CERN/LHCC/2004-009
LHCC I-013
22 March 2004

Heavy Ion Physics with the ATLAS Detector

ATLAS Collaboration

Letter of Intent

ATLAS Collaboration

Armenia
Yerevan Physics Institute, Yerevan

Australia
Research Centre for High Energy Physics, Melbourne University, Melbourne
University of Sydney, Sydney

Austria
Institut für Experimentalphysik der Leopold-Franzens-Universität Innsbruck, Innsbruck

Azerbaijan Republic
Institute of Physics, Azerbaijan Academy of Science, Baku

Republic of Belarus
Institute of Physics, National Academy of Science, Minsk
National Centre for Particle and High Energy Physics, Minsk

Brazil
Universidade Federal do Rio de Janeiro, COPPE/EE/IF, Rio de Janeiro

Canada
University of Alberta, Edmonton
University of Carleton/C.R.P.P., Carleton
Group of Particle Physics, University of Montreal, Montreal
Department of Physics, University of Toronto, Toronto
Simon Fraser University, Burnaby, BC
TRIUMF, Vancouver
Department of Physics, University of British Columbia, Vancouver
University of Victoria, Victoria

CERN
European Laboratory for Particle Physics (CERN), Geneva

China
Joint Cluster formed by IHEP Beijing, USTC Hefei, University of Nanjing and University of Shandong

Czech Republic
Academy of Sciences of the Czech Republic, Institute of Physics and Institute for Computer Science, Prague
Charles University in Prague, Faculty of Mathematics and Physics, Prague
Czech Technical University in Prague, Faculty of Nuclear Sciences and Physical Engineering, Faculty of Mechanical Engineering, Prague

Denmark
Niels Bohr Institute, University of Copenhagen, Copenhagen

France
Laboratoire d'Annecy-le-Vieux de Physique des Particules (LAPP), IN2P3-CNRS, Annecy-le-Vieux
Laboratoire de Physique Corpusculaire, Université Blaise Pascal, IN2P3-CNRS, Clermont-Ferrand
Laboratoire de Physique Subatomique et de Cosmologie de Grenoble, IN2P3-CNRS Université Joseph Fourier, Grenoble
Centre de Physique des Particules de Marseille, IN2P3-CNRS, Marseille
Laboratoire de l'Accélérateur Linéaire, IN2P3-CNRS, Orsay
LPNHE, Universités de Paris VI et VII, IN2P3-CNRS, Paris
Commissariat à l'Energie Atomique (CEA), DSM/DAPNIA, Centre d'Etudes de Saclay, Gif-sur-Yvette

Georgia
Institute of Physics of the Georgian Academy of Sciences and Tbilisi State University, Tbilisi

Germany
Physikalisches Institut, Universität Bonn, Bonn
Institut für Physik, Universität Dortmund, Dortmund
Fakultät für Physik, Albert-Ludwigs-Universität, Freiburg
Institut für Hochenergiephysik der Universität Heidelberg, Heidelberg
Institut für Physik, Universität Mainz, Mainz
Lehrstuhl für Informatik V, Universität Mannheim, Mannheim
Sektion Physik, Ludwig-Maximilian-Universität München, Munich
Max-Planck-Institut für Physik, Munich
Fachbereich Physik, Universität Siegen, Siegen
Fachbereich Physik, Bergische Universität, Wuppertal

Greece
Athens National Technical University, Athens
Athens University, Athens
Aristotle University of Thessaloniki, High Energy Physics Department and Department of Mechanical Engineering, Thessaloniki

Israel
Department of Physics, Technion, Haifa
Raymond and Beverly Sackler Faculty of Exact Sciences, School of Physics and Astronomy, Tel-Aviv University, Tel-Aviv
Department of Particle Physics, The Weizmann Institute of Science, Rehovot

Italy
Dipartimento di Fisica dell'Università della Calabria e I.N.F.N., Cosenza
Laboratori Nazionali di Frascati dell'I.N.F.N., Frascati
Dipartimento di Fisica dell'Università di Genova e I.N.F.N., Genova
Dipartimento di Fisica dell'Università di Lecce e I.N.F.N., Lecce
Dipartimento di Fisica dell'Università di Milano e I.N.F.N., Milan
Dipartimento di Scienze Fisiche, Università di Napoli 'Federico II' e I.N.F.N., Naples
Dipartimento di Fisica Nucleare e Teorica dell'Università di Pavia e I.N.F.N., Pavia
Dipartimento di Fisica dell'Università di Pisa e I.N.F.N., Pisa
Dipartimento di Fisica dell'Università di Roma I 'La Sapienza' e I.N.F.N., Roma

Dipartimento di Fisica dell'Università di Roma II 'Tor Vergata' e I.N.F.N., Roma
Dipartimento di Fisica dell'Università di Roma III 'Roma Tre' e I.N.F.N., Roma
Dipartimento di Fisica dell'Università di Udine, Gruppo collegato di Udine I.N.F.N. Trieste, Udine

Japan
Hiroshima Institute of Technology, Hiroshima
Department of Physics, Hiroshima University, Higashi-Hiroshima
KEK, High Energy Accelerator Research Organisation, Tsukuba
Department of Physics, Faculty of Science, Kobe University, Kobe
Department of Physics, Kyoto University, Kyoto
Kyoto University of Education, Kyoto
Nagasaki Institute of Applied Science, Nagasaki
Naruto University of Education, Naruto
Department of Physics, Faculty of Science, Okayama University, Okayama
Department of Computer Science, Ritsumeikan University, Kusatsu
Department of Physics, Faculty of Science, Shinshu University, Matsumoto
International Center for Elementary Particle Physics, University of Tokyo, Tokyo
Physics Department, Tokyo Metropolitan University, Tokyo
Department of Applied Physics System, Tokyo University of Agriculture and Technology, Tokyo
Institute of Physics, University of Tsukuba, Tsukuba

Morocco
Faculté des Sciences Ain Chock, Université Hassan II, Casablanca, and Université Mohamed V, Rabat

Netherlands
FOM - Institute SAF NIKHEF and University of Amsterdam/NIKHEF
University of Nijmegen/NIKHEF, Nijmegen

Norway
University of Bergen, Bergen
University of Oslo, Oslo

Poland
Henryk Niewodniczanski Institute of Nuclear Physics, Cracow
Faculty of Physics and Nuclear Techniques of the University of Mining and Metallurgy, Cracow

Portugal
Laboratório de Instrumentação e Física Experimental de Partículas (LIP), Lisbon, in collaboration with: University of Lisboa, University of Coimbra, University Católica-Figueira da Foz and University Nova de Lisboa

Romania
National Institute for Physics and Nuclear Engineering, Institute of Atomic Physics, Bucharest

Russia
Institute for Theoretical and Experimental Physics (ITEP), Moscow
P.N. Lebedev Institute of Physics, Moscow

Moscow Engineering and Physics Institute (MEPhI), Moscow
Moscow State University, Moscow
Budker Institute of Nuclear Physics (BINP), Novosibirsk
State Research Center of the Russian Federation - Institute for High Energy Physics (IHEP), Protvino
Petersburg Nuclear Physics Institute (PNPI), Gatchina, St. Petersburg

JINR
Joint Institute for Nuclear Research, Dubna

Republic of Serbia
Institute of Physics, University of Belgrade, Belgrade

Slovak Republic
Bratislava University, Bratislava, and Institute of Experimental Physics of the Slovak Academy of Sciences, Kosice

Slovenia
Jozef Stefan Institute and Department of Physics, University of Ljubljana, Ljubljana

Spain
Institut de Fisica d'Altes Energies (IFAE), Universidad Autónoma de Barcelona, Bellaterra (Barcelona)
Physics Department, Universidad Autónoma de Madrid, Madrid
Instituto de Fisica Corpuscular (IFIC), Centro Mixto Universidad de Valencia - CSIC, Valencia and Instituto de Microelectrónica de Barcelona, Bellaterra (Barcelona)

Sweden
Fysika institutionen, Lunds universitet, Lund
Royal Institute of Technology (KTH), Stockholm
University of Stockholm, Stockholm
Uppsala University, Department of Radiation Sciences, Uppsala

Switzerland
Laboratory for High Energy Physics, University of Bern, Bern
Section de Physique, Université de Genève, Geneva

Taiwan
Institute of Physics, Academia Sinica, Taipei

Turkey
Department of Physics, Ankara University, Ankara
Department of Physics, Bogazii University, Istanbul

United Kingdom
School of Physics and Astronomy, The University of Birmingham, Birmingham
Cavendish Laboratory, Cambridge University, Cambridge
Department of Physics and Astronomy, University of Glasgow, Glasgow
Department of Physics, Lancaster University, Lancaster

Department of Physics, Oliver Lodge Laboratory, University of Liverpool, Liverpool
Department of Physics, Queen Mary and Westfield College, University of London, London
Department of Physics, Royal Holloway and Bedford New College, Egham
Department of Physics and Astronomy, University College London, London
Department of Physics and Astronomy, University of Manchester, Manchester
Department of Physics, Oxford University, Oxford
Rutherford Appleton Laboratory, Chilton, Didcot
Department of Physics, University of Sheffield, Sheffield

United States of America
State University of New York at Albany, New York
Argonne National Laboratory, Argonne, Illinois
University of Arizona, Tucson, Arizona
Department of Physics, The University of Texas at Arlington, Arlington, Texas
Lawrence Berkeley Laboratory and University of California, Berkeley, California
Physics Department of the University of Boston, Boston, Massachusetts
Brandeis University, Department of Physics, Waltham, Massachusetts
Brookhaven National Laboratory (BNL), Upton, New York
University of Chicago, Enrico Fermi Institute, Chicago, Illinois
Nevis Laboratory, Columbia University, Irvington, New York
Department of Physics, Duke University, Durham, North Carolina
Department of Physics, Hampton University, Virginia
Department of Physics, Harvard University, Cambridge, Massachusetts
Indiana University, Bloomington, Indiana
Iowa State University, Ames, Iowa
University of California, Irvine, California
Massachusetts Institute of Technology, Department of Physics, Cambridge, Massachusetts
Michigan State University, Department of Physics and Astronomy, East Lansing, Michigan
University of Michigan, Department of Physics, Ann Arbor, Michigan
Department of Physics, New Mexico University, Albuquerque
Northern Illinois University, DeKalb, Illinois
Ohio State University, Columbus, Ohio
Department of Physics and Astronomy, University of Oklahoma
Department of Physics, University of Pennsylvania, Philadelphia, Pennsylvania
University of Pittsburgh, Pittsburgh, Pennsylvania
Department of Physics and Astronomy, University of Rochester, Rochester, New York
Institute for Particle Physics, University of California, Santa Cruz, California
Department of Physics, Southern Methodist University, Dallas, Texas
State University of New York at Stony Brook, New York
Tufts University, Medford, Massachusetts
High Energy Physics, University of Illinois, Urbana, Illinois
Department of Physics, Department of Mechanical Engineering, University of Washington, Seattle, Washington
Department of Physics, University of Wisconsin, Madison, Wisconsin
Physics Department, University of Yale, New Haven, New York

Chapter 1

Introduction

The ATLAS detector has been designed to study high-p_T physics in pp collisions at the LHC centre-of-mass energy of 14 TeV and design luminosity of 10^{34} cm^{-2} s^{-1}. The experiment layout, performance and physics reach has been described in detail in many documents, in particular in several Technical Design Reports (TDR, [1, 2]). This Letter of Intent describes, for the first time, the expected potential of ATLAS for the study of ion-ion collisions.

The LHC will be able to run a variety of ion beams, thus providing nucleus-nucleus and proton-nucleus collisions. It is foreseen that the heavy-ion programme will extend for one month of running per year of operation. Since most of this time will likely be devoted to Pb-Pb collisions (at $\sqrt{s} = 5.5$ TeV per colliding nucleon pair), and since these collisions are experimentally more challenging than lighter ion-ion and proton-ion collisions, the emphasis in this document is on Pb-Pb interactions, although comments on other scenarios are made whenever appropriate.

The studies reported here represent first and preliminary attempts to establish the performance of the baseline ATLAS experiment (as described in the various TDRs) in the heavy-ion environment, and its capability to provide measurements potentially useful to constrain the underlying physics. The accent is put on high-p_T signatures, which are better matched to the ATLAS design concepts than soft final states. No changes to the detector presently under construction, nor to the trigger and DAQ system, have been assumed in most cases [1]. The results reported here represent therefore a "zero-cost" addition to the (already broad) physics potential of the baseline detector and its exploitation for a different field of physics.

The main motivation for undertaking these studies is that several features of the ATLAS detector are well suited for that part of the heavy-ion physics programme which is based on the detection of high-p_T probes. This includes a variety of phenomena, ranging from jet quenching to quarkonia suppression. When compared to the other LHC experiments, ATLAS has put particular emphasis to achieve a most hermetic and segmented calorimetric system, as well as an excellent jet energy resolution, which should allow detailed jet energy and profile measurements and therefore provide insight into the jet quenching mechanism. The air-core Muon Spectrometer, with its capability of detecting and identifying muons down to $p_T \sim 3$ GeV, is potentially useful to study the suppression of Υ and J/ψ states via their di-muon decays. Finally, the granular and precise Pixel and Silicon layers of the Inner Detector should be able to cope with the higher occupancy expected in the Pb-Pb environment compared to pp events, and should therefore be able to perform good-quality tracking

---

[1] The only exception (described in an Appendix to this document) is the possibility of adding a Zero Degree Calorimeter in the very forward regions, to improve the studies of ultra-peripheral collisions.

also in this environment.

In the absence of a complete theory able to describe heavy-ion interactions, against which one could quantify the physics potential of the experiment, the primary aim of this document is to demonstrate that ATLAS is able to detect and measure a set of basic signatures, which are generally considered crucial probes of the phenomena underlying heavy-ion collisions. Translating these capabilities into a well-defined impact on the understanding of heavy-ion theory is difficult today, but hopefully the guidance of RHIC data will help, in a near future, to narrow the broad spectrum of existing models and therefore to better define the rôle of ATLAS in heavy-ion nuclear physics.

One main difference between pp and Pb-Pb collisions at the LHC is that in the latter case the luminosity will be several orders of magnitude smaller and so will be the interaction rate. Therefore the trigger and the detectors will run in much more relaxed conditions. However, Pb-Pb collisions will produce a much larger multiplicity (typically one order of magnitude larger) of (soft) particles in the final state than pp collisions at the LHC design luminosity. The detector occupancy will therefore be much higher than in pp events, especially in the Inner Detector and in the first longitudinal compartments of the calorimeters. A first consequence for ATLAS is that the TRT detector is considered conservatively to be unusable in Pb-Pb collisions. However, the conditions will be more favourable for lighter ion-ion and proton-ion collisions, with, in some cases, a similar or more quiet environment compared to pp operation at design luminosity. In these cases, the full potential of the ATLAS detector can be exploited.

The results presented in this Letter of Intent have been obtained from detailed full-simulation studies of the detector response and performance. For this first round of studies, standard ATLAS software tools (e.g. reconstruction algorithms), not specially tuned to the peculiar heavy-ion environment, have been used in most cases. In this respect, these results can be considered as conservative.

This document is organised as follows. Chapter 1 presents some general features of heavy-ion operation at the LHC and a short overview of the main physics goals. Chapter 2 describes the simulation tools used in these studies, and Chapter 3 the detector environment. The measurement of global event features is addressed in Chapter 4, the tracking performance in Chapter 5 and jet reconstruction in Chapter 6. Studies of variables sensitive to jet quenching are presented in Chapter 7, and the detection of quarkonia resonances is discussed in Chapter 8. Chapter 9 addresses trigger issues, while Chapter 10 is devoted to the conclusions. Finally, Appendix A describes additional instrumentation useful to study ultra-peripheral collisions.

It should be noted that by no means do the preliminary results reported here represent the final word about the ATLAS performance in heavy-ion collisions. Indeed, several areas where more detailed and extensive studies are needed have been identified, and are underlined at several places in the text. Nevertheless, this Letter of Intent demonstrates a very good potential of the ATLAS experiment for an additional and exciting physics programme, in which the Collaboration wishes to participate.

1.1 Main parameters for heavy-ion operation

Tables 1.1 and 1.2 list ions that are being considered for both nucleus-nucleus and proton-nucleus operation [3]. The luminosity for Pb-Pb runs is limited by the quenching of the magnets. At the LHC the nuclear fragmentation cross-sections are large and fragments deposit high enough energy to induce quenching at luminosities higher than 10^{27} cm^{-2} s^{-1}. The lower cross-sections for lighter ions allow higher beam luminosity. In heavy-ion operation the bunch-crossing will happen in 100 ns intervals (scenarios for 125 ns bunch-crossing intervals are also under consideration).

Colliding ions	Limit	N^{max}	$\mathcal{L}[\mathrm{cm}^{-2}\mathrm{s}^{-1}]$
^{208}Pb	Quench	7.0×10^7	1.0×10^{27}
^{115}In	SC	2.2×10^8	1.0×10^{28}
^{84}Kr	SC	3.3×10^8	2.3×10^{28}
^{40}Ar	SC	5.5×10^8	6.4×10^{28}
^{16}O	SC	1.0×10^9	2.1×10^{29}
^{4}He	SC	5.2×10^9	5.7×10^{30}

Table 1.1: List of ion species and peak luminosities that will be available at the LHC for ion-ion collisions. The limitation for the beam intensity is either magnet quench or space charge (SC) constraints in the proton synchrotron (PS) accelerator. N^{max} indicates the maximum bunch intensity.

Colliding system	$\mathcal{L}^{max}[\mathrm{cm}^{-2}\mathrm{s}^{-1}]$
p+Pb	7.4×10^{29}
p+Ar	5.5×10^{30}
p+O	1.0×10^{31}

Table 1.2: For various proton-ion collisions, the expected maximum peak luminosities achievable at the LHC.

In Pb-Pb collisions, the average luminosity expected with three experiments (ALICE, ATLAS and CMS) running concurrently is 4×10^{26} cm^{-2} s^{-1}, if the injected current is for 10^{27} cm^{-2} s^{-1}. There is also a minimum value for the luminosity, namely $\sim 5 \times 10^{25}$ cm^{-2} s^{-1}, set by the sensitivity of the beam monitors.

It is assumed here that each year the LHC will be running in heavy-ion mode for one month. This corresponds approximately to 10^6 s of useful data taking time, assuming a 40% machine and experiment efficiency. The current schedule foresees a very short (few days) run during the first year of LHC operation, used to commission the ion injection and acceleration system. The first complete run (in 2008) will likely be based on Pb-Pb collisions at nominal luminosity, followed, a year later, by proton-Pb collisions, which are needed to normalize the Pb-Pb data. The subsequent years will be devoted either to Pb-Pb or to lighter ion collisions, depending on the physics scenarios emerging from the first runs.

The environment to which the detectors will be exposed can be deduced from Table 1.3, which shows the charged particle multiplicities per pseudo-rapidity unit expected from various nucleus-nucleus collisions. Although there are large uncertainties on these estimates (see Chapter 2), it can still be concluded that Pb-Pb final states will be one order of magnitude more crowded than pp final states. On the other hand the experimental conditions in proton-ion collisions will be similar to pp running at high luminosity.

It should be noted that at the LHC relatively light ions, such as Krypton, may already produce the conditions for the formation of a hot dense partonic medium. Because of this argument, because of the lower particle multiplicity produced in these collisions than in Pb-Pb, and because of the higher luminosity, these lighter ions are potentially very interesting for ATLAS, since the full capabilities of the whole detector could be exploited.

Colliding system	$< dN_{ch}/d\eta >$
Pb+Pb	$\approx$ 3200
Kr+Kr	$\approx$ 900
p+Pb	$\approx$ 200
p+p at 10^{34} cm^{-2} s^{-1}	$\approx$ 200

Table 1.3: Average charged particle multiplicities per pseudo-rapidity unit expected to be produced in central collisions of various ion beams, compared to one pp bunch-crossing at design luminosity.

Proton-nucleus interactions will be asymmetric. Since the proton beam will be accelerated to the nominal 7 TeV energy, the centre of the rapidity (y) distribution of the system will be shifted. For instance, for proton-Pb collisions the shift will be

$$\Delta y = \frac{1}{2} ln \frac{Z_1 A_2}{Z_2 A_1} \sim 0.5$$

where Z and A are the atomic and mass numbers of the two nuclei, respectively, and the centre-of-mass energy per nucleon will be

$$\sqrt{s} = 14 \sqrt{\frac{Z_1 Z_2}{A_1 A_2}}\ \mathrm{TeV} = 9\ \mathrm{TeV}$$

The large ATLAS coverage can accommodate this rapidity shift.

1.2 Nucleus-nucleus collisions

Nucleus-nucleus collisions at the LHC represent an unprecedented opportunity to create and study the Quark-Gluon Plasma (QGP) in the laboratory at the energy frontier. In central Pb-Pb collisions (impact parameter $b \sim 0$ fm), an enormous number of virtual partons, dominated by gluons, are freed from the nuclear wave function. These partons should form a QGP characterized by quark deconfinement and restoration of approximate chiral symmetry. One major advantage of the higher LHC energy compared to RHIC is that the initial parton densities are so high that a description of the gluons as colour field solutions to the Yang-Mills equation may be relevant. This picture, referred to as the colour glass condensate, has had some initial success in describing RHIC data, but would be in a more relevant regime of Q^2 at the LHC [4, 5].

The first step in characterizing the newly-created system is to determine its global properties. The ATLAS detector capabilities of measuring a relevant set of global observables, such as charged particle multiplicities and energy flow, are discussed in Chapter 4. These measurements will also allow the determination of the collision impact parameter and hence of the collision centrality.

In addition to the global system properties, one wants to use various QCD probes sensitive to the properties of the medium. The simplest of these probes is a hard-scattered parton (quark or gluon) that travels through the dense medium. The rate of high-p_T partons, and hence jets, is calculable in the factorization scheme with a pQCD parton-parton cross-section. These partons are expected to multiple-scatter from the many colour charges in the created medium and thus radiate bremsstrahlung gluons [6, 7, 8]. It should be noted that recent RHIC results [9, 10] show evidence for partonic energy losses in a dense medium created in most violent heavy-ion collisions.

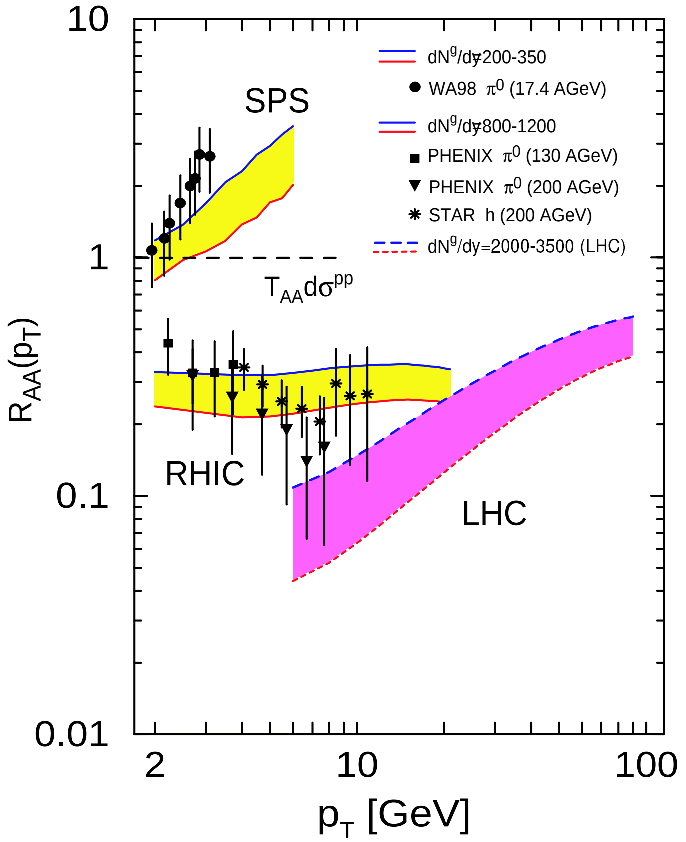

Figure 1.1: Suppression/enhancement factor R_{AA} in the production cross-section for single hadrons in heavy-ion collisions (normalized to pp interactions), as a function of transverse momentum. Data from the SPS and RHIC are shown, together with extrapolations to the LHC. The shaded bands indicate the theoretical predictions [11] for various gluon densities in the coloured medium.

There are two important measurable modifications to the jet properties from the medium (jet quenching). First, since the parton radiates additional gluons, thus losing energy, there will be a strong suppression of high-z ($z = p_{hadron}/p_{jet}$) hadrons from the jet fragmentation. Conservation of energy dictates that this must also result in a correlated increase in the total particle multiplicity of the jet. Experimentally, this can be observed for instance by looking at single-hadron spectra, as done at RHIC [9, 10]. The predicted behaviour for higher energy hadrons at the LHC, where (in contrast to previous machines) quenching is expected to dominate over other phenomena like the Cronin effect and shadowing [11], is shown in Fig. 1.1.

Second, the radiated gluons have a broader angular distribution than the unmodified jet profile, and thus one may observe an effective decrease (compared to pp interactions) in the jet cross-section as measured for a specific cone size. Alternatively, one may measure the jet energy profile as a function of cone radius $R = \sqrt{\Delta\eta^2 + \Delta\phi^2}$.

Calculations of the angular distribution of the medium-induced radiated energy are shown in Fig. 1.2. It can be seen that the thicker and denser the medium, the larger is the radiated energy.

Studies of jet-jet correlations in multijet events can also provide insight into the quenching

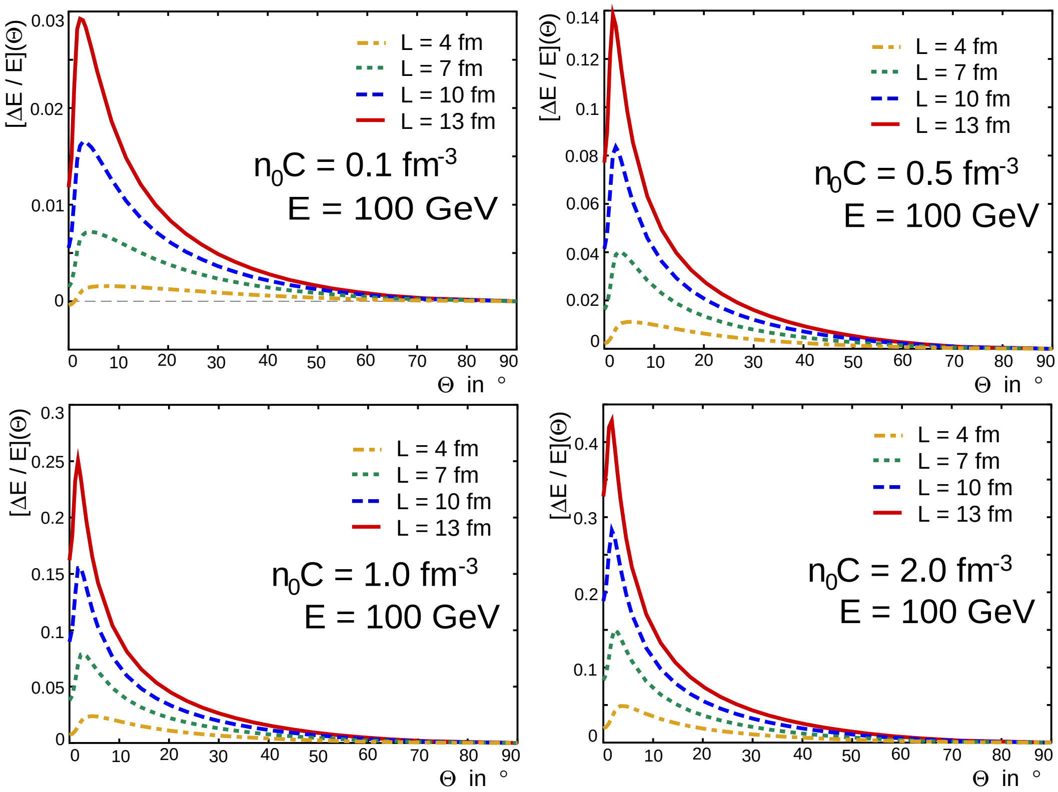

Figure 1.2: Angular distribution of the gluon energy radiated by 100 GeV partons, as calculated for different colour charge densities (n_0C) and medium thicknesses (L).

mechanism. Recent measurements from STAR [10] at RHIC reveal a suppression of the back-to-back correlation between high-p_T hadrons in most central Au-Au collisions. These observations are compatible with models indicating that one jet is frequently emitted from the surface, while the partner passes through the bulk medium thus suffering large energy loss. These results underline the importance of di-jet measurements at the LHC. Furthermore, gluons, because of their additional colour charge compared to quarks, should lose even more energy while traversing the medium. Observation of the suppression of the 3-jet topology, if experimentally feasible, would probe this phenomenon.

The ATLAS potential for measuring jet properties potentially sensitive to quenching is discussed in Chapter 7. The expected event rates are large, in contrast to RHIC, as shown in Table 1.4.

Finally, the study of γ-jet and Z-jet events offers a very clean way of probing any anomaly in the jet behaviour. This is because the photon and the Z traverse the coloured medium unaffected, and therefore allow for a controlled comparison with the associated jet. The excellent γ/π^0 separation capability of the ATLAS calorimeters (optimised for $H \to \gamma\gamma$ searches) should be extremely useful to select samples of γ+jet events with good purity. Unfortunately, the cleaner of these two channels, Z+jet production, suffers from a low rate. In one month of Pb-Pb data taking, about 500 $Z \to \mu^+\mu^-$ with $p_T > 40$ GeV are expected in ATLAS. Very detailed studies of these processes in pp interactions have been made [1], but they have not yet been extended to heavy-ion collisions.

Recent theoretical investigations [12] indicate that charm and bottom quarks propagating through

Transverse momentum (GeV)	Number of events
50	30×10^6
100	1.5×10^6
150	1.9×10^5
200	4.4×10^4

Table 1.4: Expected numbers of high-p_T jet events in ATLAS with $|\eta| < 4.9$ for one month (10^6 s) of Pb-Pb running at a luminosity of $\mathcal{L} = 4 \times 10^{26}$ cm^{-2} s^{-1}.

a dense partonic medium radiate less energy compared to light quarks, due to the "dead cone" effect (i.e. less collinear gluons are emitted by heavy quarks). Therefore, the possibility of tagging b-jets produced in heavy-ion collisions in ATLAS would give an additional tool to understand quenching and may allow crucial comparisons to be made with light-quark jets. This is discussed in Chapter 5.

It should be noted that these various jet observables will also have important implications on the understanding of gluon shadowing and saturation physics.

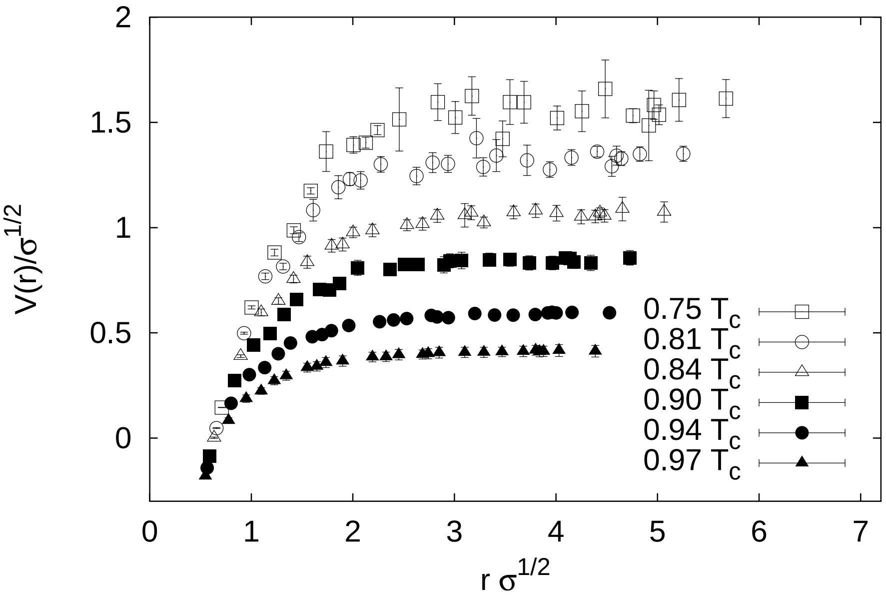

Figure 1.3: The QCD potential for heavy-quark pairs, as a function of distance, for various temperatures. T_c indicates the critical temperature (at which the transition from nuclear matter to QGP takes place), and σ is the colour string tension at zero temperature.

Another interesting phenomenon is the transition to deconfinement of heavy quarkonia. It is expected that in the dense colour medium the individual partons are deconfined and move about relatively freely within the plasma boundaries. The heavy-quark potential calculated from lattice QCD [13] is shown in Fig. 1.3. One can see a clear onset of deconfinement as the long-range potential is screened. This phenomenon can be studied by systematic measurements of heavy quarkonia states produced in proton-proton, proton-ion and ion-ion reactions. The upsilon states have quite different binding energies, and thus can act as a QCD thermometer of the plasma. As seen in Fig. 1.4, the effective size (i.e. binding energy) of the upsilon resonance is much smaller (larger) than that of the J/ψ. Therefore it is expected, in the context of this calculation, that the beauty quarkonia disappear at higher temperatures than the charm quarkonia.

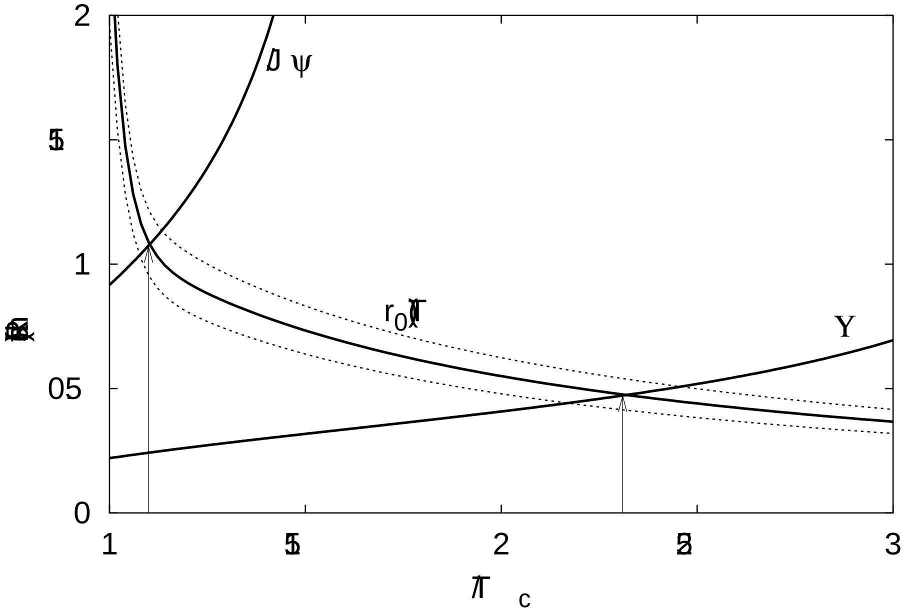

Figure 1.4: Effective radius of the J/ψ and Υ resonances as a function of temperature. The screening radius r_0 as a function of temperature is also indicated (with dashed lines showing a range of parameters). The intersections between the screening and the resonance curves (indicated by vertical arrows) give the temperatures of dissociation.

The ATLAS potential for the detection and separation of quarkonia states is discussed in Chapter 8.

Finally, it should also be noted that precise measurements of the main expected QGP signatures (jet profiles, quarkonia production, etc.) in pp (and pA, see below) interactions will be used as a normalization for the heavy-ion data, and therefore will be indispensable to obtain a convincing evidence of any anomalous behaviour in these data.

1.3 Proton-nucleus collisions

Measurements of proton-nucleus collisions at the LHC will not only provide essential control of the hard processes that are expected to determine the initial conditions of heavy-ion collisions, as mentioned above, but these measurements can also address physics that is, in its own right, of fundamental interest.

The full ATLAS detector will be functional for proton-nucleus operation because, as shown in Table 1.3, these collisions yield similar occupancy to that expected from the $\sim$ 25 simultaneous proton-proton collisions per bunch-crossing at the LHC design luminosity.

Much of the interest in proton-nucleus collisions at the LHC is focused on the perturbative production of gluons and the modifications of the gluon distribution $g(x, Q^2)$ in the nucleus at low Bjorken x. Already at RHIC, the perturbative production of gluons is expected to play an important rôle in determining the initial conditions of a heavy-ion collision [14, 15]. At the LHC energies, hard gluon production becomes even more important due to the growth of the gluon distribution at low x. For example, the production of gluon jets with p_T=20 GeV through ordinary QCD processes will involve initial-state gluons at $x \sim 2 \times 10^{-3}$. The more copiously produced lower p_T gluon jets will probe even lower x values.

At such low x, strong modifications of the nuclear gluon distribution are expected, and understanding these modifications will be essential to deduce the initial conditions of heavy-ion collisions at the LHC. At large Q^2, the modifications to $g(x, Q^2)$ are best understood in the context of shadowing, and extensive pQCD calculations of the nuclear size and the x-dependence of the shadowing modifications of the gluon distribution in heavy nuclei have been performed [16]. Studies of γ-jet and jet-jet production in proton-nucleus collisions will allow these modifications to be measured, thus providing both an essential test of the theoretical calculations and an important constraint on the initial conditions of heavy-ion collisions. The large pseudo-rapidity coverage of ATLAS should allow the nuclear shadowing to be mapped out over a range $\sim 10^{-4} < x < 10^{-2}$.

At lower Q^2, saturation effects can be studied. The physics of saturation is controlled by a scale, Q_s, such that the growth in the gluon density in the nucleus with decreasing k_T (the gluon transverse momentum) is cut off for $k_T \leq Q_s$. In the very small x range accessible at the LHC, Q_s may be larger than 4 GeV [17], and since the $g(x, Q^2)$ distribution is sensitive to gluons with $k_T^2 \leq Q^2$ [18], it should be possible to directly probe the saturated gluons by measuring hadron production over the range $2 \leq p_T \leq 4$ GeV. The ATLAS Inner Detector has been designed to have good tracking efficiency in this momentum range over the full pseudo-rapidity coverage $|\eta| < 2.5$. One aspect of saturation that is not yet well understood is its effect on hard-scattering processes for $Q^2 \sim Q_s^2$. It has been suggested that the gluon k_T distribution could be significantly modified well above Q_s. If so, then it should be possible to study the Q^2 evolution of saturation effects in ATLAS by performing γ-jet and jet-jet measurements over a large phase space.

Another important physics topic that can be addressed by proton-nucleus measurements is the applicability of factorization in hard-processes involving nuclei. No experiment that has studied either nuclear deep-inelastic scattering or proton-nucleus collisions has been able to simultaneously investigate many different hard-processes to explicitly demonstrate that factorization applies. ATLAS will be able to study single-jet and jet-jet events, γ-jet events, heavy-quark, Z and W production, Drell-Yan processes, etc., and to probe the physics of jet fragmentation. With this wide variety of experimentally accessible hard-processes, which should all be determined by the same parton distributions, it should be possible to demonstrate clearly the success of factorization for $Q^2 >> Q_s^2$. Detailed studies of the behaviour of jet fragmentation as a function of pseudo-rapidity could be used to determine if the fragmentation is modified by the presence of the nucleus or its large number of low-x gluons. The observation, or lack thereof, of modifications to the jet fragmentation could provide sensitive tests of the formation time and coherence in the re-dressing of the hard-scattered parton and the longitudinal spatial spread of low-x gluons in a highly Lorentz-contracted nucleus.

Yet another interesting problem that can be well studied in proton-nucleus collisions at the LHC is that of double hard-scattering events. These are events in which, for example, two separate partons in the proton undergo a hard scattering in the nucleus. Such events have been observed in $p\overline{p}$ collisions at the Tevatron [19]. In addition to providing a sensitive test of QCD, they directly probe parton correlations in the proton [20]. It has been argued that when these events take place in a nuclear target, the correlations from the partons in the nucleus are relaxed, so by comparing pp and pA data on double hard scattering, the understanding of parton correlations in the nucleon may be dramatically improved [21].

1.4 Ultra-peripheral nuclear collisions

Heavy-ion collisions where the impact parameter b is larger than the sum of the nuclei radii are referred to as ultra-peripheral collisions (UPC). The physics of ultra-peripheral collisions changes character with increasing centre-of-mass energy. At the Bevalac, AGS and SPS fixed-target experiments the equivalent photon spectrum extends far enough to induce photo-nuclear fragmentation of one or both nuclei. At RHIC, the equivalent photon spectrum extends to ~ 100 GeV in the nucleus rest frame, and measurements have been reported on total inelastic cross-sections and vector meson photoproduction [22, 23]. At the LHC, the highly Lorentz-contracted electric field of the ions can be viewed as a source of high-energy photon-photon and photon-nucleon collisions, that are competitive with electron-positron colliders and deep-inelastic scattering at HERA. Therefore the LHC can extend the measurements of hadron structure made at HERA to higher energies (even higher than available at electron-ion colliders currently under discussion) and to nuclear targets. It will be possible to study hard processes such as heavy-quark and di-jet production, which is analogous to hard-diffraction studies at the Tevatron [24].

The partonic structure of the heavy ions at small Bjorken x can be studied via heavy quark production in high-energy photon-hadron interactions, where virtual photons emitted coherently from one nucleus interact with the other ion. The coherence condition implies that the photon Q^2 range is limited to $\sim 1/R^2_{nucleus}$. On the other hand the cross-sections for photo-nuclear excitations are very large (enhanced by $\sim Z^2$), exceeding the nuclear geometrical cross-section.

A common feature of photon-exchange and diffractive (Pomeron-exchange) interactions is the presence of rapidity gaps in the final state. Rapidity gaps can occur because the photon and Pomeron carry no colour charge. This experimental signature has been exploited in studies of $p\overline{p}$ interactions at the Tevatron and ep at HERA. Particles are observed in the central detector, in conjunction with a leading particle in at least one beam direction. Charged particle multiplicity and calorimeter energy distributions are used to search for gaps in the event structure. When momentum measurement of the leading particles became available [24], it was demonstrated that the key kinematical quantities (momentum of exchanged particles) could be measured either from the leading particles or with the central detector. In the case of heavy-ion collisions the momentum transfers are small compared to the natural beam spread, so only the latter method is available. The large rapidity coverage of ATLAS is well suited to the study of these topologies.

Tagging of heavy-ion UPC is relatively straightforward using Zero Degree Calorimeters, as done at RHIC. In roughly 15% of ρ photo-production events, additional photon exchange occurs which results in nuclear excitation and a neutron tag. The multi-photon exchange is a feature of heavy-ion collisions, since the strength of the interaction, characterized by $Z^2\alpha$, is large. The neutron tag results in a significantly harder equivalent photon spectrum because it selects small impact parameters [25]. Instead of falling roughly as $1/E$, the neutron-tagged spectrum is essentially flat out to the cutoff (10^5 GeV in ATLAS with Pb beams). Since both photon-exchange and Pomeron-exchange interactions can be studied in ATLAS with heavy-ion and proton beams, it will be interesting to compare the features in both cases.

Consider the analogous processes of two-photon exchange and double-Pomeron exchange. In both cases there is a leading particle in each beam direction and an isolated cluster in the central region. The physics is similar to $\gamma\gamma$ interactions at LEP. However, with hadron beams there is strong competition from the double-Pomeron process. With proton beams double-Pomeron dominates over two-gamma for the highest masses [26]. It may be possible to distinguish the two processes and isolate a two-gamma signal using the t-distribution of the leading protons [27]. The situation is reversed in the case of Pb beams. The coherent photon exchange grows rapidly with atomic number (as Z^4), whereas Pomeron exchange is expected to grow only as $A^{2/3}$. The net result is that Pomeron exchange dominates in pp collisions and two-photon exchange dominates in Pb-Pb collisions.

The ATLAS detector fulfills the prerequisites for a programme of physics in this field, in that it has hermetic coverage with tracking and high quality calorimetry over full azimuth and over pseudo-rapidity $|\eta| < 4.9$. The tools developed for the analysis of electromagnetic interactions at RHIC, such as neutron tags and rapidity gap detection, will also be available in ATLAS. Additional instrumentation which would be useful for these studies (e.g. to trigger on the most peripheral interactions) is discussed in Appendix A.

Chapter 2

Simulation Tools

The ATLAS potential for heavy-ion physics has been evaluated as follows:

- The HIJING event generator [28], version 1.38, was used to generate nucleus-nucleus collisions at the LHC energy. These samples constitute the basis for the study of global event properties and provide the high-density background of soft particles.
- High-p_T probes, like QCD di-jet events, have been generated with PYTHIA. In some cases, and for specialized studies such as $\Upsilon \rightarrow \mu\mu$ decays, a single particle generator has also been used. These high-p_T samples have then been embedded in central (i.e. with impact parameter $b < 1$ fm) Pb-Pb collisions produced with HIJING.
- All generated events have been processed through a full and detailed GEANT3-based simulation of the ATLAS detector.

Whenever possible, data samples produced during the ATLAS Data Challenge 1 have also been used.

2.1 The HIJING event generator

The HIJING Monte Carlo was developed to study particle production in high-energy pp, pA and AA collisions. It is based on a perturbative QCD description of multiple mini-jet production in hard parton scattering. For soft processes, with small transverse momentum transfers (below 2 GeV), a string description of soft-gluon exchanges between valence quarks or di-quarks is adopted. The Lund (JETSET) fragmentation scheme is used for jet and string hadronization. A nucleus-nucleus collision is decomposed into a sequence of binary collisions involving participant and excited nucleons. The Glauber model [29] is used to describe the collision geometry and compute the number of binary collisions. Additional nuclear effects are also incorporated. These include the nuclear shadowing of the parton structure functions and the final-state energy loss by a high-p_T parton in a dense medium (jet quenching). Nuclear shadowing, namely the modification of the effective number of partons at low x values (leading to a decrease in the multiplicity of produced particles), is modeled by suitable parametrizations of the quark and gluon structure functions in the small and medium x region. Jet quenching is described via gluon radiation with an assumed average energy loss of partons traversing the dense medium. The process of energy loss is stopped when the p_T of a parton falls below 2 GeV. HIJING does not incorporate any final state re-interactions among produced particles.

The HIJING model has been tested against data from pp, $p\overline{p}$ and AA collisions over a wide energy range. Figure 2.1(a) shows the predictions of HIJING (both with jet quenching switched on and off) for the charged particle density over the region $|\eta| < 1$ in central heavy-ion collisions. They are compared with experimental data from the AGS centre-of-mass energy (about 4 GeV) up to the highest RHIC energy of 200 GeV [30]. RHIC results show that HIJING with jet quenching overestimates significantly the particle multiplicity. On the other hand the saturation model of Ref. [31] reproduces reasonably well the data.

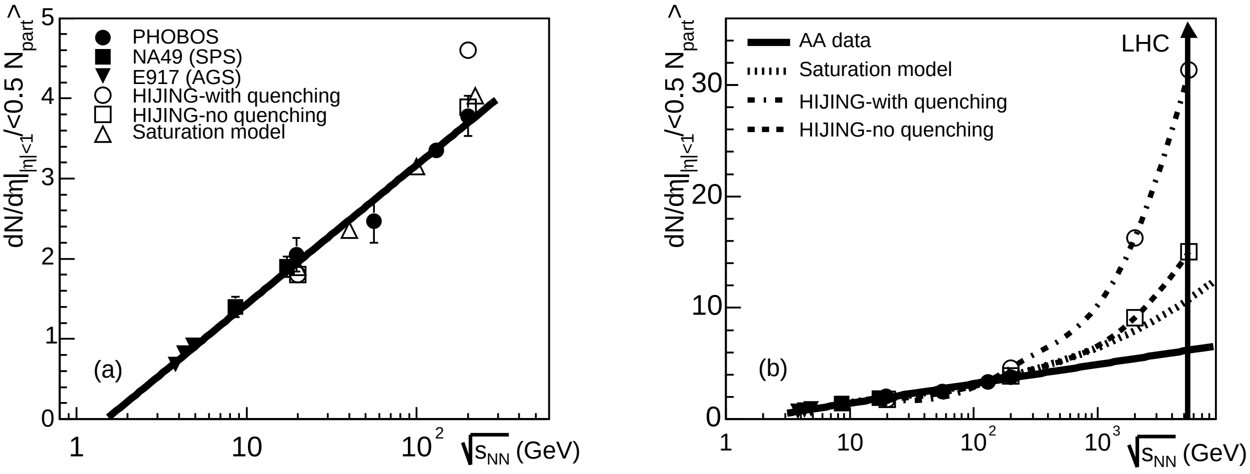

Figure 2.1: Average number of charged particles per pseudo-rapidity unit and per participant pair, over the region $|\eta| < 1$, as a function of the centre-of-mass energy of the pair of nucleons. (a) Comparison of various models with experimental data. (b) Extrapolation of data and models to the LHC energy.

The extrapolation of both the data and the model predictions to the LHC energies is shown in Fig. 2.1(b). Assuming an average number of participants $< N_{part} > \simeq 380$ for central Pb-Pb collisions at the LHC energies, the expected number of charged particles per pseudo-rapidity unit from the extrapolation of the experimental data is $dN_{ch}/d\eta \sim 1200$. On the other hand, the model predictions vary from about 2000 in the case of the saturation model, to about 3000 for the HIJING generator without jet quenching, up to about 6000 for HIJING with jet quenching turned on. It is therefore likely that HIJING overestimates the particle densities at the LHC, especially if parton energy losses are incorporated. It should also be noted that the HIJING model with jet quenching on is not able to reproduce the particle p_T spectra measured at the RHIC energies [32]. Therefore, for the studies presented in this document the jet quenching was switched off, which still gives a much higher level of soft background than other models. The results reported here are therefore conservative. For some specific tasks, small samples of HIJING events have been generated with jet quenching turned on.

2.2 Simulation strategy

The simulation of the detector response used for these studies is based on the GEANT 3.21 package, and includes a detailed description of the detector geometry, of the dead material and of the signal response from the various sensitive elements. This simulation is the same as that used to produce large event samples from pp collisions in the framework of the Data Challenge 1, except for two modifications introduced to save processing time in Pb-Pb collisions. First, the energy threshold for tracking was raised from 100 keV (standard value used for ATLAS physics simulations) to 1 MeV. Second, for most of the (preliminary) studies reported here the pseudo-rapidity acceptance of the generated particles was limited to $-3.2 < \eta < 3.2$.

A sample of 20000 events was simulated in these conditions and with an impact parameter b spanning the range 0–15 fm. In addition, two samples from central Pb-Pb collisions ($b < 1$ fm) were produced, one with an energy threshold for tracking of 100 keV, and one with the initial (staged) layout of the pixel detector (i.e. two pixel layers instead of three).

The simulation chain and environment are illustrated in Fig. 2.2. HIJING events were generated with different centralities and stored. They were then processed through the GEANT3 simulation and finally digitized (this last step includes the details of the detector readout response). The complete simulation of one central ($b = 0 - 1$ fm) Pb-Pb event takes approximately 6-8 hours of CPU on the US-ATLAS computer farm (~ 100 1 GHz Pentium III Coppermine processors).

A procedure for overlapping two event samples is also available (see Fig. 2.2), which turned out to be very useful to study rare processes with adequate and affordable statistics. Two different events (e.g. a high-p_T "signal" event and a background soft event) are simulated separately (with identical detector geometries) and are then merged at the GEANT hit level, before digitization.

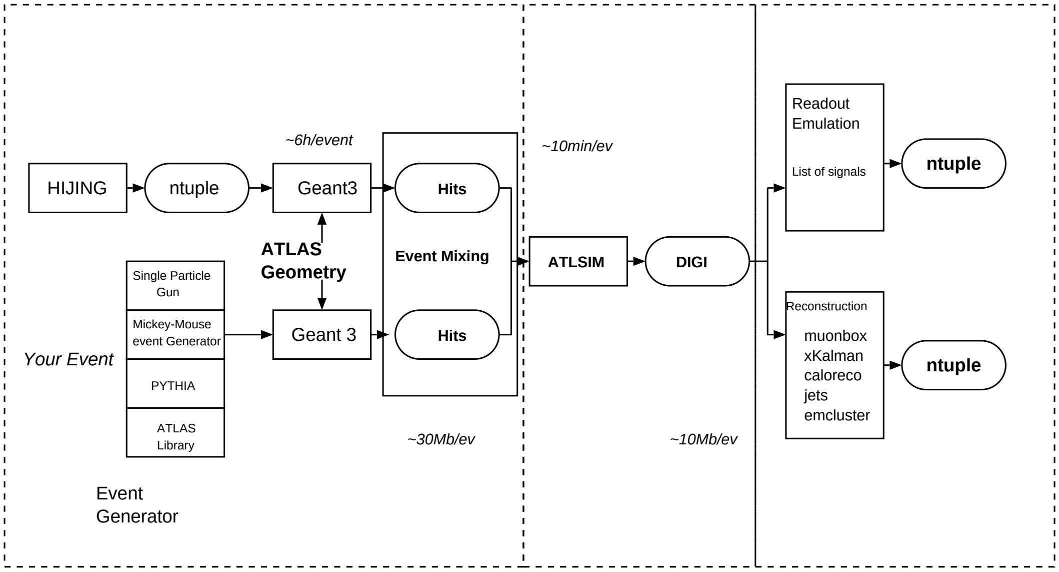

Figure 2.2: Sketch of the simulation chain and environment used for the studies described in this document.

For most of the preliminary studies reported here, the simulated events were reconstructed using the standard ATLAS reconstruction software and algorithms, and only in a few cases (e.g. jet reconstruction) heavy-ion specific modifications were implemented. Several areas where dedicated algorithms could improve the performance have been identified in the course of the study (e.g. pattern recognition in the inner detector), and will be the subject of future work. As a consequence, the results presented in this document can be considered as conservative also from the reconstruction performance point of view.

Chapter 3

Detector Occupancies

Detector occupancies in the heavy-ion environment have been evaluated for central ($b = 0 - 1$ fm) Pb-Pb collisions. HIJING events without jet quenching have been used, which are characterised by an average charged particle multiplicity per pseudo-rapidity unit $< dN_{ch}/d\eta > \ \simeq 3200$ (see Fig. 2.1b). Most of these particles have $p_T < 1$ GeV.

3.1 Inner Detector

Thanks to their excellent granularity, the precision layers (Pixels and SCT) are expected to experience acceptable occupancies even in central heavy nucleus-nucleus collisions. Figure 3.1 shows that the occupancy does not exceed 2% in the Pixel detector, and stays below 20% in the SCT. These values, which are one order of magnitude larger than in pp events at design luminosity, were obtained using very low thresholds for particle tracking in GEANT (100 keV). More studies are needed to evaluate the impact on the occupancy from particles produced beyond $|\eta| = 3.2$ (expected to be less than $\sim$ 20%).

In contrast, the TRT detector, because of its long straws, will suffer from much higher occupancies and may not be able to contribute to tracking in the busy heavy-ion environment. However, this problem can be reduced with the use of a faster gas. In addition, the TRT can probably be used for proton-nucleus collisions and maybe also for very light ($A < 20$) ion-ion collisions. These possibilities will be investigated in the future.

The track reconstruction capabilities of the ATLAS precision layers in central Pb-Pb collisions are discussed in Chapter 5.

3.2 Calorimeters

Figure 3.2 shows the transverse energy deposited in towers of size $\Delta\eta \times \Delta\phi = 0.1 \times 0.1$ in the electromagnetic and hadronic calorimeters (a tower extends over the full detector depth). Most of the energy (few GeV) is released in the first longitudinal compartment (strip section) of the electromagnetic calorimeter. The average transverse energy flow as a function of η is also shown in Fig. 3.2. A very simple calibration procedure has been used in this study, therefore the variations in the calorimeter response (e.g. the drops at the transition between the barrel and the end-cap electromagnetic calorimeters) are not completely corrected for.

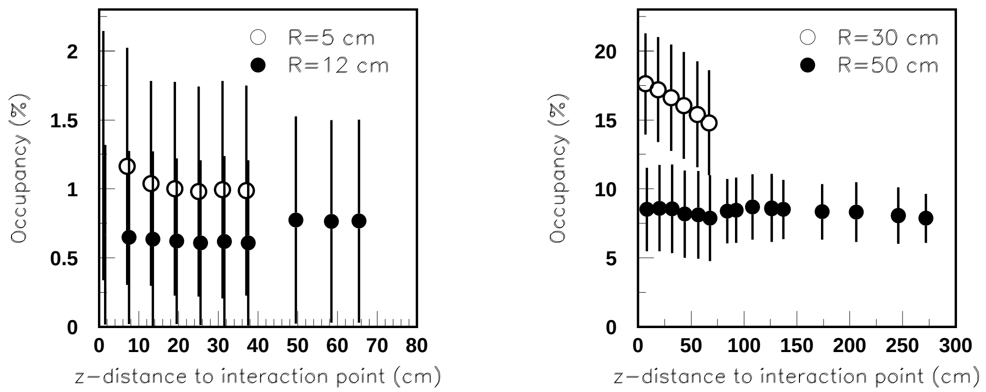

Figure 3.1: For central Pb-Pb collisions ($b = 0 - 1$ fm) at the LHC, the average occupancies in the Pixel (left panel) and SCT (right panel) detectors, as a function of the distance along the beam line from the interaction point, at two fixed radii. The error bars give the spread of values around the average. These results were obtained with the (unquenched) HIJING Monte Carlo.

3.3 Muon Spectrometer

In pp runs at high luminosity the occupancy in the Muon chambers is expected to originate mainly from a neutron gas diffused in the cavern, produced by the interactions of particles from the primary collision with the detector and machine elements along the beam line.

In heavy-ion collisions such a background will be negligible. In addition, most of the (soft) particles from the Pb-Pb interaction will be absorbed by the calorimeters. As a consequence, the Muon chambers will show very little activity and the number of hits (mainly due to decays in flight of π and K produced in the primary collision) will be much lower than that expected during pp operation, as shown in Table 3.1.

Muon chambers	pp at 10^{34} cm^{-2} s^{-1}	Pb-Pb with $b < 1$ fm
BIL $\eta = 0.2$	1.9	0.3
BML $\eta = 0.2$	5.1	0.5
BOL $\eta = 0.2$	6.7	0.5
EIL $\eta = 2.0$	14.8	0.9

Table 3.1: Average number of hits per chamber in the Muon Spectrometer for pp operation at high luminosity and for Pb-Pb central collisions. Results are given for the barrel large muon chambers in the inner/middle/outer stations (BIL/BML/BOL) at $\eta = 0.2$, and for the end-cap large muon chambers in the inner station (EIL) at $\eta = 2.0$.

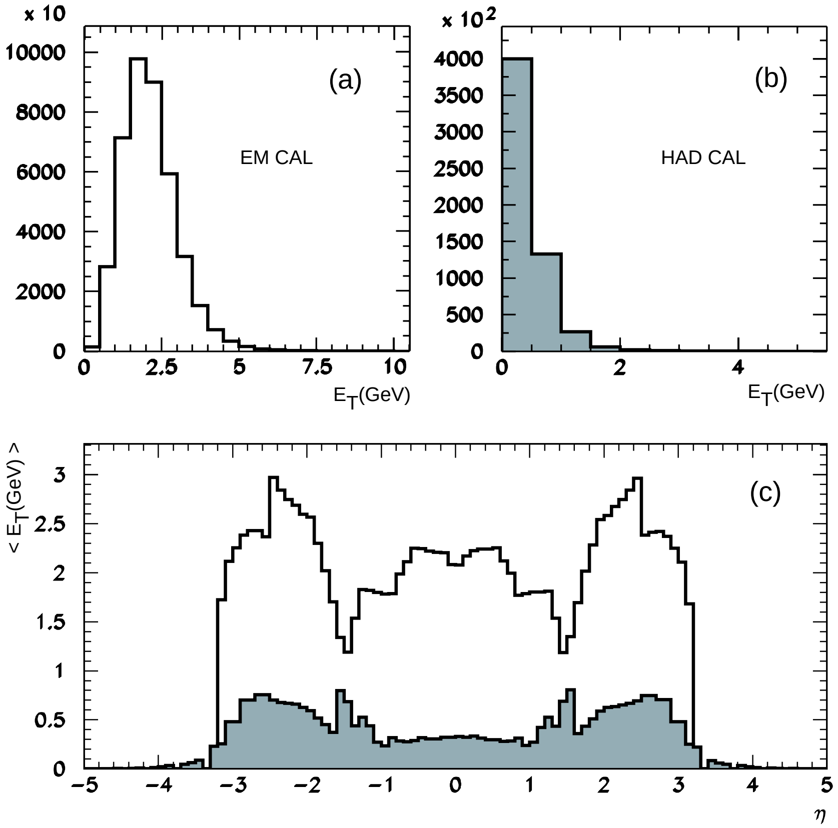

Figure 3.2: Distribution of the transverse energy deposited in towers of size $\Delta\eta \times \Delta\phi = 0.1 \times 0.1$ of the electromagnetic (a) and hadronic (b) calorimeter (all towers with $|\eta| < 3.2$ are included in these plots). The average transverse energy per tower in the electromagnetic (light histogram) and hadronic (dark histogram) calorimeter is shown in (c) as a function of pseudo-rapidity (see text for explanation of the structures).

Chapter 4

Global Variables

Charged particle multiplicities (N_{ch}) and charged particle densities ($dN_{ch}/d\eta$) are the most fundamental observables which will be measured at the beginning of the heavy-ion operation at the LHC. Indeed, they provide the global properties of the system created in the collisions and reflect the time integral over a variety of physics processes contributing to the multi-particle production. From these basic measurements one can infer information about the initial conditions, like the energy density and the parton density saturation. These observables are also sensitive to the details of the nuclear structure functions, to the interplay of hard and soft processes, and to the effects of nuclear shadowing and jet quenching. Finally, the rescattering processes taking place during later stages of the system evolution, and the entropy production throughout the whole system evolution, also influence the particle production. Two other "day-one" measurements, namely the total transverse energy (E_T) and the transverse energy per pseudo-rapidity unit ($dE_T/d\eta$), can in addition determine how much of the initially available energy is converted into the transverse degrees of freedom. These measurements provide also a way to study the experimental environment to which the detector is exposed, and to estimate the accuracy of the measurements of other observables.

The initial conditions of heavy-ion interactions are predominantly determined by the energy and the geometry of the nuclear collision. The impact parameter b between the colliding nuclei defines their overlap area. Using the Glauber model [29] one can calculate the number of nucleons participating in inelastic processes (N_{part}) and the number of binary nucleon-nucleon collisions (N_{coll}) as a function of b. These parameters, which characterize the centrality of the event, are however not directly measurable, and other variables must be used, which are experimentally accessible and which are highly correlated with the above parameters. Charged particle multiplicities and transverse energies depend monotonically on the impact parameter (and on N_{part}, N_{coll}). This dependence can be exploited to correlate a fraction of the cross-section, selected by making cuts on the measured signals, to a range in b, N_{part}, and N_{coll}. Therefore these measurable global event properties can be used to estimate the centrality of the collision, an indispensable information for more detailed analysis of particle production and to compare the theory to data.

Despite the basic nature of the global event measurements, there is no precise theoretical prediction calculable from first principles. This is mainly due to the fact that such predictions require the description of the entire collision process, and the underlying dynamics at the different stages of the system evolution is not precisely known. Thus, only model predictions are available, which however suffer from large uncertainties. Before the first measurements became available at RHIC energies, both extrapolations to these energies from the SPS data and the various model expectations varied widely. RHIC measurements [30] have provided valuable constraints and shown that most models overestimate the charged particle multiplicity. However, although RHIC data are now available, extrapolations over more than one order of magnitude in $\sqrt{s}$ to the LHC energies are still affected by large uncertainties and the predictions for the charged particle multiplicity in Pb-Pb collisions vary significantly from model to model (see Fig. 2.1). Therefore only direct measurements can provide stringent constraints on these models.

Charged particle multiplicities and densities can be measured over $|\eta| < 2.5$ using the precision layers of the Inner Detector, where the occupancy levels are relatively small (see Chapter 3). In addition, the hermetic coverage of the calorimeters allows a detailed study of the transverse energy deposited in different phase-space regions.

4.1 Charged particle multiplicity

The event multiplicity, N_{ch}, was inferred from the total number of signals, N_{sig}, recorded in the readout channels of the Pixel and SCT layers. As already mentioned in Chapter 2, HIJING events were processed through a full GEANT simulation of the detector, including the response of the readout electronics. Saturation effects in the Pixel readout system (the module controller chip holds no more than ~1800 hits) were taken into account (they are however negligible). The resulting signals are therefore very similar to those that will be recorded during actual data taking.

In addition, the correlation between the total event energy (E_{tot}) and total transverse energy (E_T) deposited in the calorimeters and the charged particle multiplicity was also studied.

It was found that the relation between N_{sig} and N_{ch} is approximately linear, and is similar in the various layers of the Inner Detector with the exception of the innermost barrel Pixel [1]. Therefore the signals from all precision layers (except the first one) were combined, in order to reduce statistical fluctuations. The result is shown in the left panel of Fig. 4.1. Here, N_{ch} is defined as the number of primary charged particles produced within the range $|\eta| < 2.5$, as obtained from the HIJING generator. Similarly, an approximately linear relation is observed between N_{ch} and the total energy and transverse energy deposited in the electromagnetic and hadronic calorimeters (see middle and right panels in Fig. 4.1).

The distributions in Fig. 4.1 were fitted with second-order polynomials. These parameterizations provided a way to reconstruct the charged particle multiplicity (N_{ch}^{rec}) on an event-by-event basis, using either the total number of Inner Detector signals or energy depositions in the calorimeters. The reconstructed multiplicity distribution obtained from the Inner Detector information is compared in Fig. 4.2 to the HIJING input distribution. The agreement is very good. The relative statistical reconstruction errors, defined as $|(N_{ch}^{rec} - N_{ch}^{true})|/N_{ch}^{true}$, are shown in Fig. 4.3 for the three experimental variables used in this study. The conclusion is that these relatively simple global measurements reproduce the charged particle multiplicity with an accuracy of about 1-2% for central Pb-Pb collisions. For most peripheral interactions, the precision deteriorates to about 10%. The best measurements are obtained using the Inner Detector Information.

It should be noted that this analysis depends heavily on the exact parameterization of N_{sig}, E_{tot}, E_T versus N_{ch}, which is derived from the simulation of HIJING events. This dependence can be studied, and the related uncertainty derived, by using different event generators (and hence different particle compositions and momentum distributions). Additional uncertainties come from the accuracy of the GEANT physics models at low energy (production of secondary particles, multiple

---

[1] In the innermost Pixel layer the correlation between N_{sig} and N_{ch} is weaker than in the other layers. This is maybe due to physics and/or readout saturation effects, and is presently under investigation.

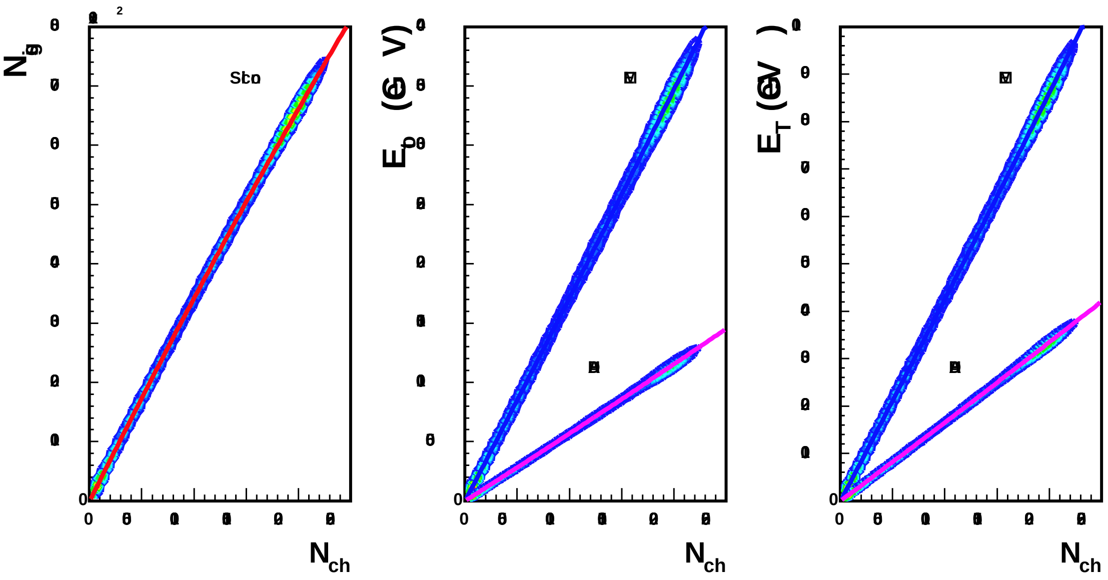

Figure 4.1: The correlations between the event charged particle multiplicity and: the total number of signals from the Pixel and SCT channels (left panel), the total energy deposited in the electromagnetic and hadronic calorimeters (middle panel), the total transverse energy deposited in the calorimeters (right panel). The solid lines indicate the best fits.

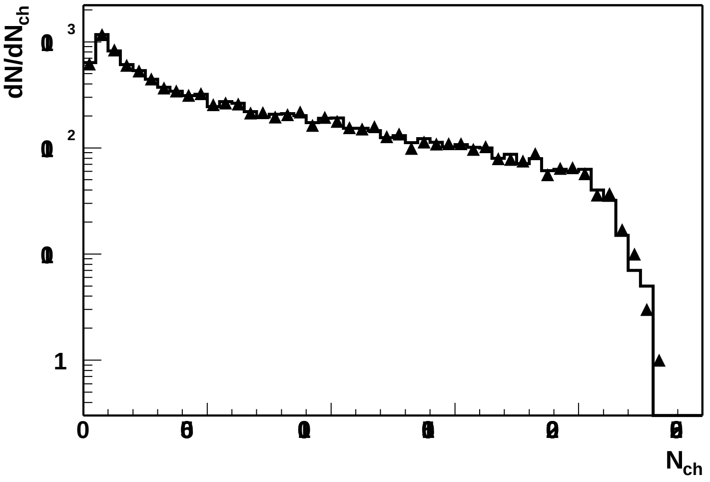

Figure 4.2: Comparisons between the event charged particle multiplicity in Pb-Pb collisions reconstructed using the information from the Inner Detector signals (triangles) and the multiplicity generated with the HIJING Monte Carlo (histogram).

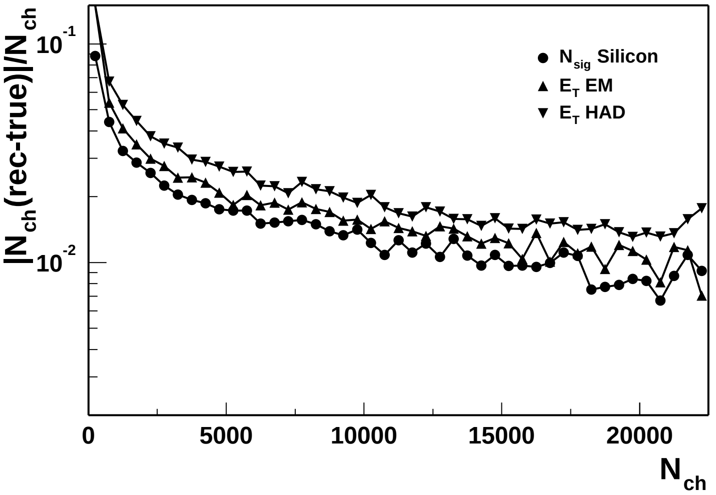

Figure 4.3: The relative statistical error on the reconstructed charged particle multiplicities ($|(N_{ch}^{rec} - N_{ch}^{true})|/N_{ch}^{true}$) versus the generated multiplicity, as obtained from measurements in the Inner Detector (dots) and in the calorimeters (triangles).

interactions, etc.). Finally, some simplifications in the simulation of the detector response have been used for this preliminary work, namely the electronic noise of the calorimeters ($E \simeq$ 300 MeV in a tower of size $\Delta\eta \times \Delta\phi = 0.1 \times 0.1$ extending over the full depth of the electromagnetic section at η ~0) has not been included. These issues, as well as other possible sources of systematic uncertainties, will be addressed in future studies.

4.2 Charged particle density

Not only the total particle multiplicity, but also the particle density versus pseudo-rapidity, $dN_{ch}/d\eta$, should provide crucial information about the underlying physics in heavy-ion collisions. Indeed, this observable is sensitive to dynamical effects like jet quenching and nuclear shadowing (see Section 2.1).

Figure 4.4 compares the pseudo-rapidity distributions of charged particles as predicted by the HIJING model with jet quenching switched off (the default of these studies) and on. Very large differences are visible, in particular the particle density at central pseudo-rapidity increases by more than a factor of two when quenching is included. Neglecting nuclear shadowing effects can result in a further increase of the particle multiplicity in this pseudo-rapidity region.

To reconstruct pseudo-rapidity distributions of charged particles, individual signals recorded in the barrel layers of the Pixel detectors were analysed. Here only results obtained with the innermost pixel layer, which has the largest acceptance in η, are reported.

Signals from neighboring pixels were added to form clusters, to take into account the fact that a charged particle traversing the detector usually leaves energy in more than one pixel. The cluster size was defined according to the following criteria. In the non-bending z-direction (along the beam axis), the number of pixels to be merged depends on the track polar angle (which is related to the z-coordinate of the signal), the vertex position, and the distance between the pixel and the beam axis. In the azimuthal direction, the number of pixels traversed depends on the particle transverse

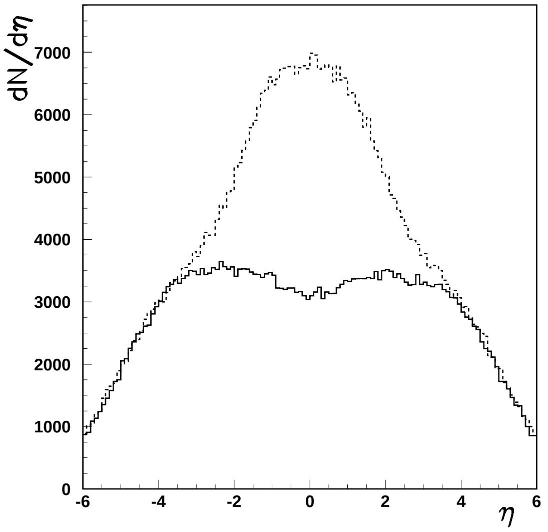

Figure 4.4: Charged particle pseudo-rapidity distributions for Pb-Pb collisions with $b < 1$ fm, as obtained from the HIJING generator with (dashed histogram) and without (solid histogram) jet quenching. Nuclear shadowing effects are included in both cases.

momentum.

Pixels with signals exceeding 10000 electrons were chosen as cluster seeds. The clustering procedure starts from the seed with the largest signal, to which hit pixels are attached as long as they have an adjacent pixel already belonging to the cluster and the distance to the seed is smaller than the expected maximal size of the cluster in both z and φ.

The pseudo-rapidity distribution of the clusters reconstructed in this way shows a significant excess at large $|\eta|$, as compared to the distribution of the primary charged particles. This excess can be attributed to several effects. Because of the magnetic field, charged particles move along a helix with radius proportional to their p_T. As a consequence, they hit barrel sensors at a larger distance from the vertex in z than if they traveled along a straight line. Thus the cluster is found at larger pseudo-rapidity values than the initial particle. In addition, particles which have low-enough p_T to be bent back to the barrel region can produce multiple clusters. Finally, particles from secondary interactions (more abundant at large $|\eta|$) also contribute to the observed effect.

Therefore, in order to extract the correct charged particle pseudo-rapidity distribution, Monte Carlo based correction factors had to be applied. These correction factors are defined as a function of η in the following way:

$$C(\eta) = \frac{(dN_{ch}/d\eta)_{rec}}{(dN_{ch}/d\eta)_{true}}. \tag{4.1}$$

The correction factors calculated with a sample of 50 central ($b = 0 - 1$ fm) Pb-Pb collisions are shown in Fig. 4.5 for the innermost pixel layer. A smooth functional dependence was fitted to the calculated $C(\eta)$, as shown in the figure.

This parameterization was then used to correct the reconstructed $dN_{ch}/d\eta$. An example is shown

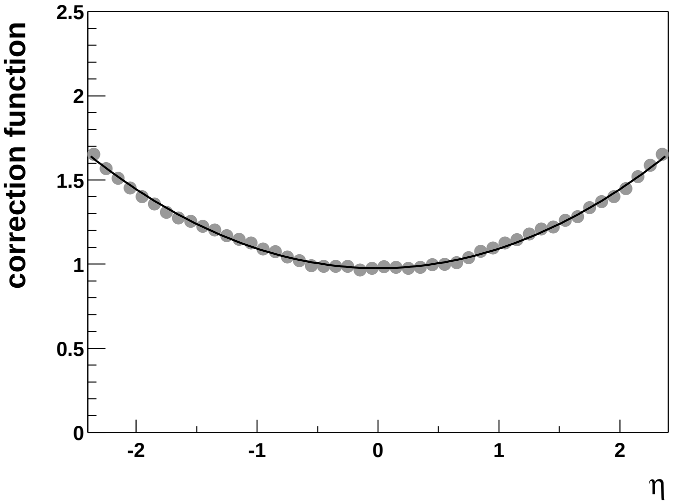

Figure 4.5: Correction factors to the charged particle density distribution (see text), obtained for the innermost pixel layer from a sample of 50 central Pb-Pb collisions. The curve shows the fitted parameterization.

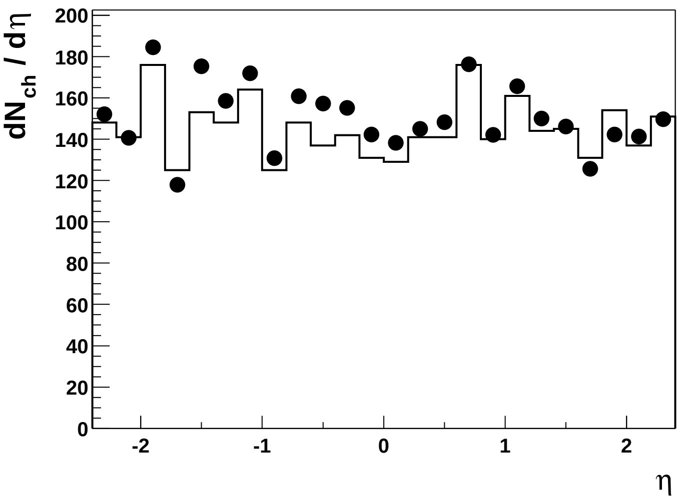

Figure 4.6: Comparison of the reconstructed charged particle density distribution (dots) with the true distribution (histogram) for a sample of five peripheral collisions.

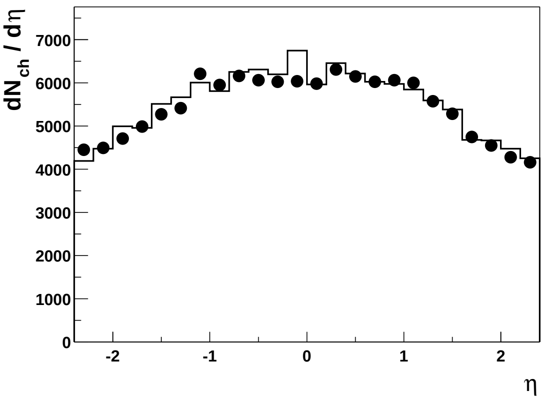

Figure 4.7: Comparison of the reconstructed charged particle density distribution (dots) with the true distribution (histogram) for one central HIJING event with jet quenching turned on.

in Fig. 4.6 for a sample of five peripheral ($b = 10-15$ fm) collisions, where the reconstructed and the generated distributions are compared. The good agreement between the two distributions indicates that the correction factors, which were determined for central collisions, are actually independent of the event centrality. The expected statistical errors on the reconstructed charged particle density for one Pb-Pb event vary from about 5% for the most central collisions, to about 9% for collisions with $b = 6 - 10$ fm, up to about 13% for the most peripheral interactions.

As a further test, the $dN_{ch}/d\eta$ distribution was also reconstructed for a central HIJING event with jet quenching turned on. In this case both, the particle density and the shape of the distribution, are expected to be significantly different from the unquenched case (see Fig. 4.4). The result obtained using the same reconstruction procedure as explained above, and exactly the same correction factors, is shown in Fig. 4.7. The excellent agreement between the measured and the generated distributions demonstrates that the reconstruction method is also insensitive to the details of the underlying dynamics from which the final-state particles are produced.

In summary, the preliminary studies reported here show that the detector performance and the reconstruction method allow a precise determination of the charged particle density distribution over the pseudo-rapidity region $|\eta| < 2.5$. This is the region most sensitive to the dynamical processes involved in particle production from heavy-ion collisions (see Fig. 4.4). An efficient tool to discriminate between different dynamical scenarios has therefore been identified. Systematic effects from the model itself and from the simulation procedure will be addressed by future studies.

In a similar way, the measurement of the energy flow as a function of pseudo-rapidity, which is based on the information of the hermetic and granular calorimeter system, should provide (possibly even more sensitive) insight into the dynamic of nucleus-nucleus collisions. Studies in this area are still in progress.

4.3 Measurement of the collision impact parameter

Since the impact parameter of the collision is not directly accessible in the experiment, measurable observables which exhibit a good correlation with it need to be used.

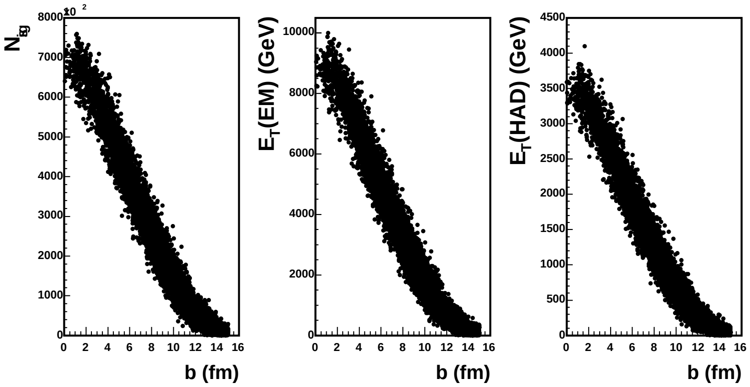

Figure 4.8: The correlations between the total number of signals in the precision layers of the Inner Detector (left panel), the total transverse energy in the electromagnetic calorimeter (middle panel), the total transverse energy in the hadronic calorimeter (right panel) and the impact parameter of the collision.

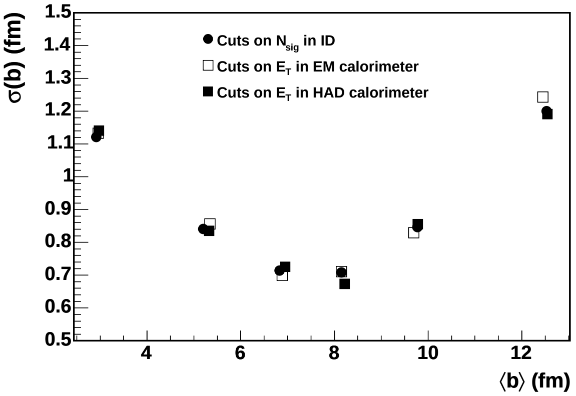

Figure 4.9: Estimated average values and σ of the impact parameter distributions for sub-samples of events selected by decreasing values of the measured global variables.

Figure 4.8 shows the relation between the impact parameter and the global variables described in Section 4.1. All of these variables decrease monotonically with increasing values of b. This quite strong correlation can thus be exploited to select events with different and well-defined centralities by making cuts on the N_{sig} and/or the E_T values, and to deduce the impact parameter with a minimal dependence on the Monte Carlo information.

The width of the estimated impact parameter distribution, $\sigma(b)$, and its average value are shown in Fig. 4.9 for sub-samples of events selected by applying different cuts on the three global variables. The fractions of events in the six bins of the figure correspond to 0-10, 10-20, 20-30, 30-40, 40-60 and 60-100% of the total sample. It can be seen that the accuracy of the estimated impact parameter is of the order of 1 fm.

It should be noted that the simulation studies reported here are restricted to the central pseudorapidity region where, as already mentioned, different dynamical processes affect the features of particle production. To determine the event centrality, on the other hand, it would be desirable to use an observable which is as much as possible insensitive to dynamical effects. A natural choice would be to measure the energy depositions in the region covered by the forward calorimeter FCAL $(3.1 < |\eta| < 4.9)$, which in ATLAS is fully integrated with the rest of the calorimeter system with minimal cracks. This study requires event simulations over the full phase space and is planned for the near future.

Chapter 5

Track Reconstruction in the Inner Detector

Particle tracking in heavy-ion events at the LHC will be a challenging task. As already mentioned in Chapter 3, the occupancy in the precision layers will be a factor of about ten larger than in pp events at high luminosity (see Fig. 3.1). In addition, it has been conservatively assumed that the TRT detector cannot be used in Pb-Pb collisions, which limits the number of measurements per track to a maximum of about ten (more precisely, eleven measurements will be available in the barrel region, of which three come from the Pixels and eight from the SCT).

On the other hand, thanks to the lower luminosity in heavy-ion operation compared to pp operation at 10^{34} cm^{-2} s^{-1}, most events will contain only a single interaction vertex, which provides a useful constraint for the Pattern Recognition.

The ability to perform tracking in Pb-Pb events, as discussed below, is potentially an important tool for the ATLAS heavy-ion physics programme, allowing e.g. the reconstruction of a clean $\Upsilon \rightarrow \mu\mu$ peak on top of the background and the study of the jet fragmentation function, as reported in Chapters 8 and 7 respectively.

5.1 Tracking performance

To determine the tracking capabilities of the ATLAS detector in the heavy-ion environment, the worst-case scenario, namely central Pb-Pb collisions with impact parameter $b < 1$ fm and with the HIJING charged particle density of $dN_{ch}/d\eta \simeq 3200$, was studied.

Events were simulated with the standard ATLAS parameters used for high-luminosity pp interactions [1]. Saturation effects in the Pixel readout, mentioned in Section 4.1, were taken into account, since they potentially affect the track reconstruction efficiency.

Tracks in the Inner Detector were reconstructed with the standard xKalman++ code [1], using only hits in the Pixel and SCT detectors. The Pattern Recognition was (partially) tuned for heavy-ion collisions by introducing an initial search for the interaction vertex using a histogramming method. Given the large number of tracks, the position of the interaction vertex can be reconstructed very fast with a resolution of about 10 μm.

The track finding then started from this common vertex (with its possible removal, at a later stage, from the reconstructed track parameters) and the Pixel detector. This reduced significantly the number of search combinations, while keeping the reconstruction efficiency high, at least for particles originating from the primary vertex.

A track candidate was accepted if at least 10 out of 11 (13) measurements in the barrel (in the intermediate and end-cap regions) were available. In addition, all three Pixel points were required to be present, and at most one cluster to be shared by more than one track. Finally, the χ^2/dof of the fit was required to be smaller than four. These stringent requirements reduce the overall track reconstruction efficiency, but keep the rate of fake tracks, produced by random combinations of hits, at a reasonably low level. This algorithm can certainly be improved in the future, for instance by requiring more measurements in the intermediate and end-cap regions and, more generally, by optimising the tuning for the heavy-ion environment.

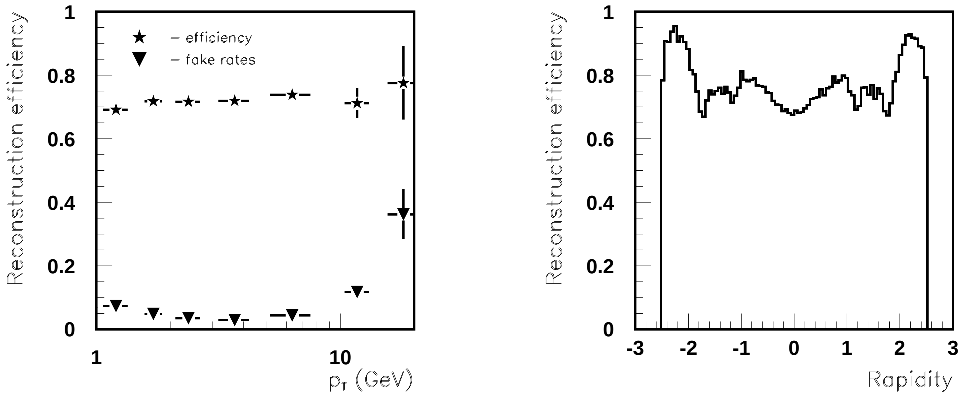

Figure 5.1: Left: Track reconstruction efficiency and percentage of fake tracks, as a function of the reconstructed p_T, for tracks with $|\eta| < 2.5$ in central Pb-Pb collisions. Right: Track reconstruction efficiency as a function of rapidity.

Preliminary results are summarized in the left panel of Fig. 5.1, which shows the track reconstruction efficiency and the fraction of fake tracks as a function of p_T, averaged over the full acceptance of the Inner Detector. The overall efficiency is $\sim 70\%$ and the fraction of fakes $\sim 5\%$ for $1 < p_T < 10$ GeV. The percentage of fakes increases at higher p_T because the number of high-p_T tracks decreases, whereas the number of fakes is approximately constant with p_T. On the other hand, the rise at p_T ~1 GeV is in large part due to the fact that, in order to save CPU time, only tracks with $p_T \geq 1$ GeV were reconstructed in this analysis. Therefore, close to the p_T threshold, many Pixel/Silicon clusters remain unassociated to good tracks and thus contribute to the combinatorial background. Efficiency and rate of fakes have been estimated using the information from the Monte Carlo truth. The right panel in Fig. 5.1 shows the tracking efficiency as a function of rapidity. The visible structures reflect the fact that the reconstruction algorithms have not been optimised for the heavy-ion environment and for a reduced number of available hits (no TRT).

The momentum resolution of the reconstructed tracks is shown in Fig. 5.2. The overall resolution obtained over $|\eta| < 2.5$, which is limited by multiple scattering in the Inner Detector material for these low-p_T tracks, is about 3%. The barrel region contributes $\sim 2\%$ and the end-cap region $\sim 4-5\%$ (due to the larger amount of material).

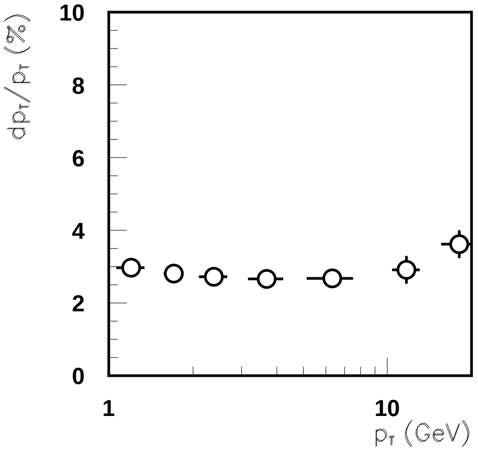

Figure 5.2: Reconstructed transverse momentum resolution as a function of p_T for tracks with $|\eta| < 2.5$ in central Pb-Pb collisions.

5.2 b-tagging

Differences in the quenching mechanisms for light and for heavy quarks have been recently predicted [12], which can be accessed experimentally if b-quark jets can be tagged in the heavy-ion environment.

Preliminary investigations of the ATLAS b-tagging performance in central Pb-Pb collisions have been made. A sample of $pp \to WH \to \ell\nu b\bar{b}$ events and a sample of $pp \to WH \to \ell\nu u\bar{u}$ events, both with $m_H = 400$ GeV, have been embedded in central Pb-Pb HIJING events. The energy of the b-jets and u-jets in these physics samples is in the range 50-400 GeV. The standard ATLAS b-tagging algorithm, based on vertexing information [1], has been used to discriminate between the two classes of jets. The results are reported in the left panel of Fig. 5.3, which shows the rejection factor against u-jets as a function of the b-jet tagging efficiency. They indicate that a rejection of ~100 against u-jets can be achieved for a b-tagging efficiency of 25% (to be compared to an efficiency of 50% in pp collisions for the same rejection). The p_T-dependence of the performance is illustrated in the right panel of Fig. 5.3. These results are conservative because algorithms developed for pp events have been used, with no special effort to optimize them for the heavy-ion environment. Furthermore, tagging of soft muons from b-decays in the low-occupancy Muon Spectrometer may improve the performance. This will be studied in the future.

5.3 Conclusions and future plans

The preliminary results reported in this Chapter indicate very encouraging tracking performances of the precision layers of the ATLAS Inner Detector in the heavy-ion environment. In addition, improvements are to be expected with more work, since in most cases algorithms optimised for the

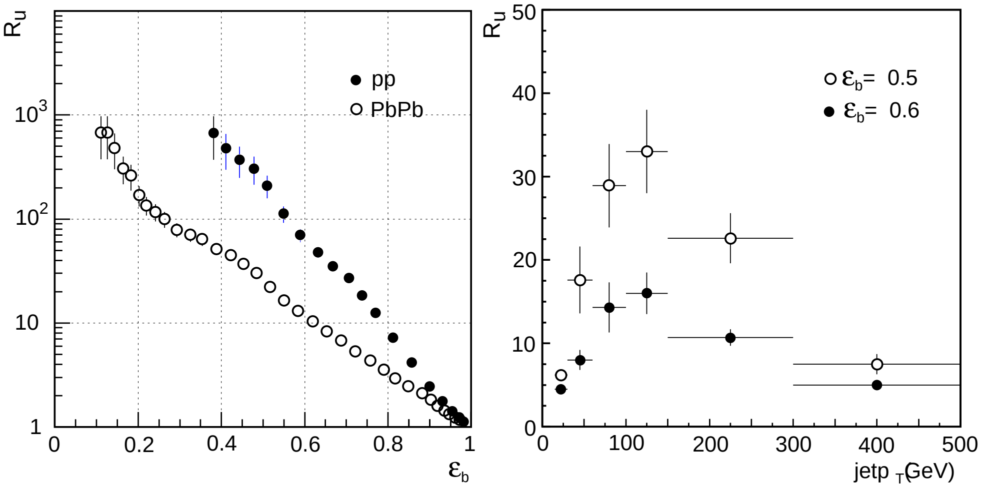

Figure 5.3: Left: rejection factor against u-jets ($\mathrm{R_u}$), as a function of the tagging efficiency for b-jets (ϵ_b), for pp collisions at low luminosity (dots) and for central Pb-Pb collisions (open symbols). Right: for central Pb-Pb collisions, rejection factor against u-jets, as a function of the jet p_T, for two values of the b-jet tagging efficiency. The jets come from samples of WH events (see text).

cleaner pp environment have been used.

Several issues require further investigation. For instance, track reconstruction efficiency and purity need to be studied in more detail and over a larger p_T range. Matching high-p_T tracks with calorimeter clusters may help to reject fakes. Studies of b-tagging need to be extended to lower jet p_T. Vertexing algorithms require tuning for the heavy-ion environment and should be combined with soft-muon tag techniques.

Chapter 6

Jet Reconstruction

Jet reconstruction in the heavy ion environment is more challenging than in pp collisions because of the larger background of low-p_T particles. This raises a number of issues:

- Jet finding: typical jet reconstruction thresholds used in ATLAS for pp collisions at low (high) luminosity are $E_T \simeq 10(20)$ GeV for a jet cone of size $\Delta R = \sqrt{\Delta\phi^2 + \Delta\eta^2} = 0.4$. The higher threshold at high luminosity is necessary because of pile-up fluctuations, which inside a $\Delta R = 0.4$ cone have an r.m.s.$(E_T) \sim$ 7 GeV. In a central lead-lead collision with impact parameter in the range 0-1 fm, the average transverse energy deposited in a $\Delta R = 0.4$ cone is approximately 50 GeV, with large fluctuations (r.m.s.$(E_T) \sim 12$ GeV). Therefore efficient and correct jet identification is challenging in the heavy-ion environment at low E_T.
- Energy resolution: the above-mentioned background fluctuations translate into an additional "noise" term contribution (i.e. of the form $1/E$) to the energy resolution, and therefore in a deterioration of the resolution itself. For jets reconstructed at $\eta \sim 0$ inside a $\Delta R = 0.4$ cone, this contribution is expected to be $\sim 12/E(\mathrm{GeV})$.
- Jet energy calibration: to optimise the jet energy resolution, suitable weights have to be applied to the energies released by the jet in the calorimeter compartments and/or cells, in order to compensate for the different detector response to the electromagnetic and hadronic components of the shower. Optimal weights may depend on the background, hence the jet energy calibration may be different for pp and for heavy-ion events. In addition, energy threshold cuts which may be applied to get rid of cells containing only noise ("zero suppression") will have an impact on the jet absolute energy scale.

To evaluate the possibility of reconstructing jets in the heavy-ion environment, QCD di-jet events generated with PYTHIA and HIJING central events (impact parameter $b = 0 - 1$ fm) were passed through a full simulation of the ATLAS detector and then merged (see Fig. 2.2). The merged events were then reconstructed using the algorithm described below. QCD jets were generated in the pseudo-rapidity range $-3.2 < \eta < 3.2$, so the results reported here represent the average response of the calorimeter system over this range.

6.1 Jet reconstruction algorithm

Before reconstructing the jets, the average transverse energy from the background must be subtracted from each calorimeter tower. This has been done with an iterative procedure. First, the average background was estimated in rings of size $\Delta\eta \times \Delta\phi = 0.1 \times 2\pi$, and was subtracted from each calorimeter tower (tower granularity $\Delta\eta \times \Delta\phi = 0.1 \times 0.1$). Then, a sliding window algorithm was used to find jet candidates, which were reconstructed inside cones of size $\Delta R = 0.4$. At this point, the initial energies of the jet towers, i.e. before the background subtraction described above, were considered again. For each jet found, a cone of size $\Delta R = 0.2$ was built around the jet axis and the background was estimated from towers in the annular region $0.2 < \Delta R < 0.4$. This background was then subtracted from the jet towers. Finally, jet candidates were accepted if their transverse energy was above 40 GeV. The results of this procedure, which is not optimal and will be refined in the future, are illustrated in Figs. 6.1 and 6.2 for jets with $E_T \simeq 55$ GeV and $E_T \simeq 280$ GeV respectively. A third jet from the HIJING event is visible in Fig. 6.2, which survives the background subtraction procedure.

The background subtraction ensures that on average the jet transverse energy is correct, but fluctuations in the background level can produce fake jets. This problems affects mainly low-E_T jets, as discussed in the next Section.

6.2 Reconstruction efficiency and rate of fake jets

The efficiency of the reconstruction procedure described above was evaluated by counting reconstructed jets matching the generated PYTHIA jets within a cone of size $\Delta R = 0.2$. To define a PYTHIA (truth) jet, all particles within the jet cone (except neutrinos) were considered.

To estimate the number of fake jets, the original HIJING (background) sample without PYTHIA jets was inspected. For each successful match between a reconstructed and a true jet in the PYTHIA+HIJING sample, the presence of a jet in the HIJING background sample matching the direction of the above-mentioned jet was looked for. A wider cone was used in this case ($\Delta R = 0.4$). If such a jet was found in the background sample, this jet was counted as a fake.

The jet reconstruction efficiency and the fraction of fakes are shown in Fig. 6.3a. The efficiency reaches 95% for jets with $E_T > 75$ GeV and drops to approximately 80% for $E_T \sim 40$ GeV. The fraction of fake jets is negligible for $E_T > 75$ GeV and rises to 20% for $E_T \sim 40$ GeV. However this estimate of fake jets is conservative, since some of them are indeed real jets from the HIJING event and not just mistakes of the reconstruction algorithm due to background fluctuations. For technical reasons (only part of the Monte Carlo truth information was available), it was not possible to distinguish between these two classes of HIJING "jets" in these preliminary studies.

6.3 Jet energy resolution

The H1 algorithm was used to calibrate the jet energy and optimise the energy resolution, along the lines discussed in [1]. The jet energy resolution was obtained from Gaussian fits to the transverse energy distributions for each E_T bin. The result obtained over the pseudo-rapidity range $-3.2 < \eta < 3.2$ is shown in Fig. 6.3b, and compared to the resolution for pp events in the same pseudo-rapidity range. At large E_T the performance is similar because the heavy-ion background has a negligible impact. Background fluctuations give a sizable contribution, as expected, below 100 GeV.

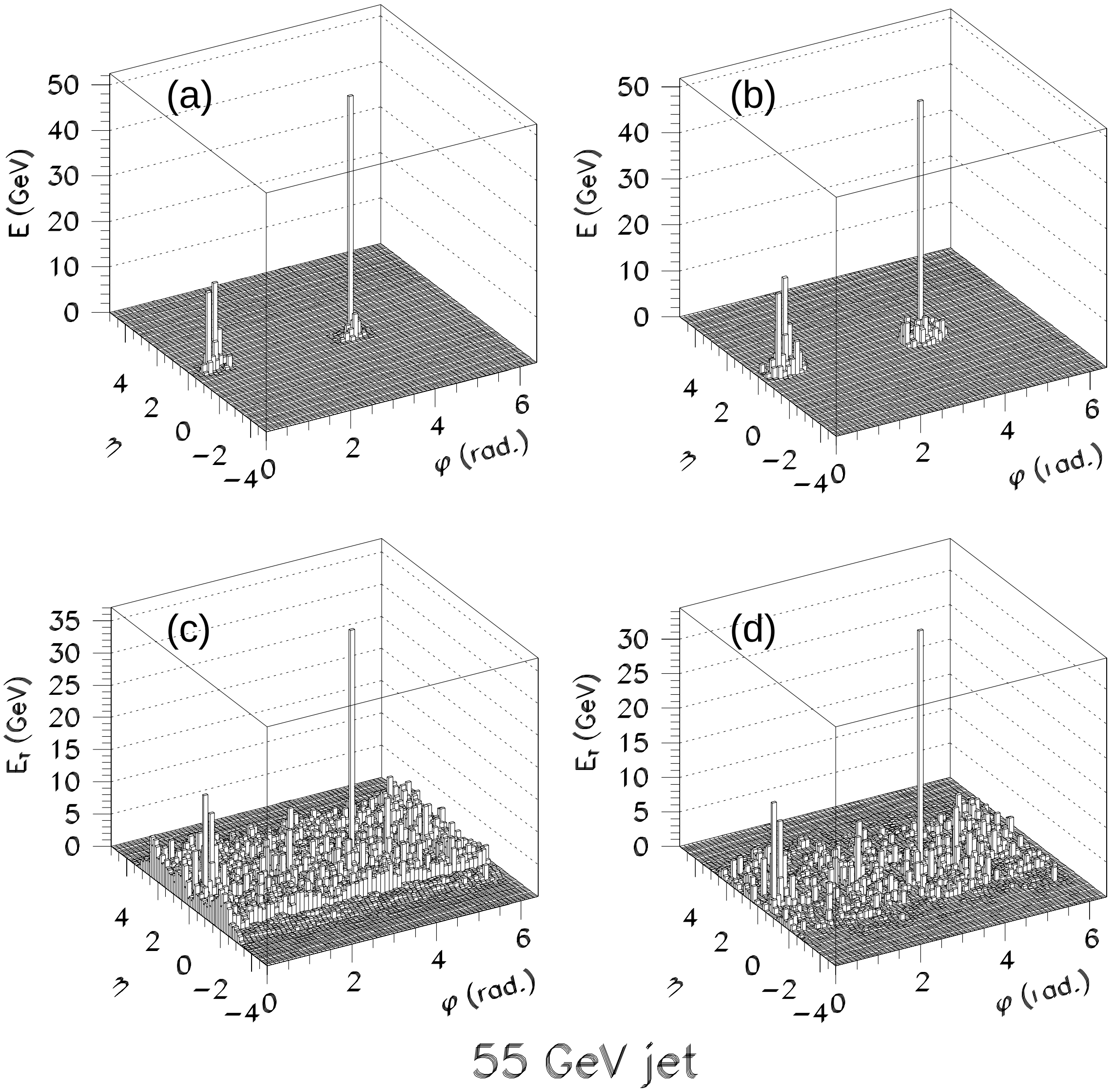

Figure 6.1: Illustration of the jet reconstruction algorithm. (a): reconstructed QCD di-jet event from PYTHIA in the pp environment; (b): the same QCD di-jet event reconstructed in the heavy-ion environment; (c) and (d): the same QCD di-jet event embedded in the HIJING background before and after background subtraction, respectively. Note that the vertical scale indicates energy (transverse energy) per tower in the top (bottom) plots. The di-jet event has been generated with a momentum transfer $\hat{p}_T^{hard} = 55$ GeV.

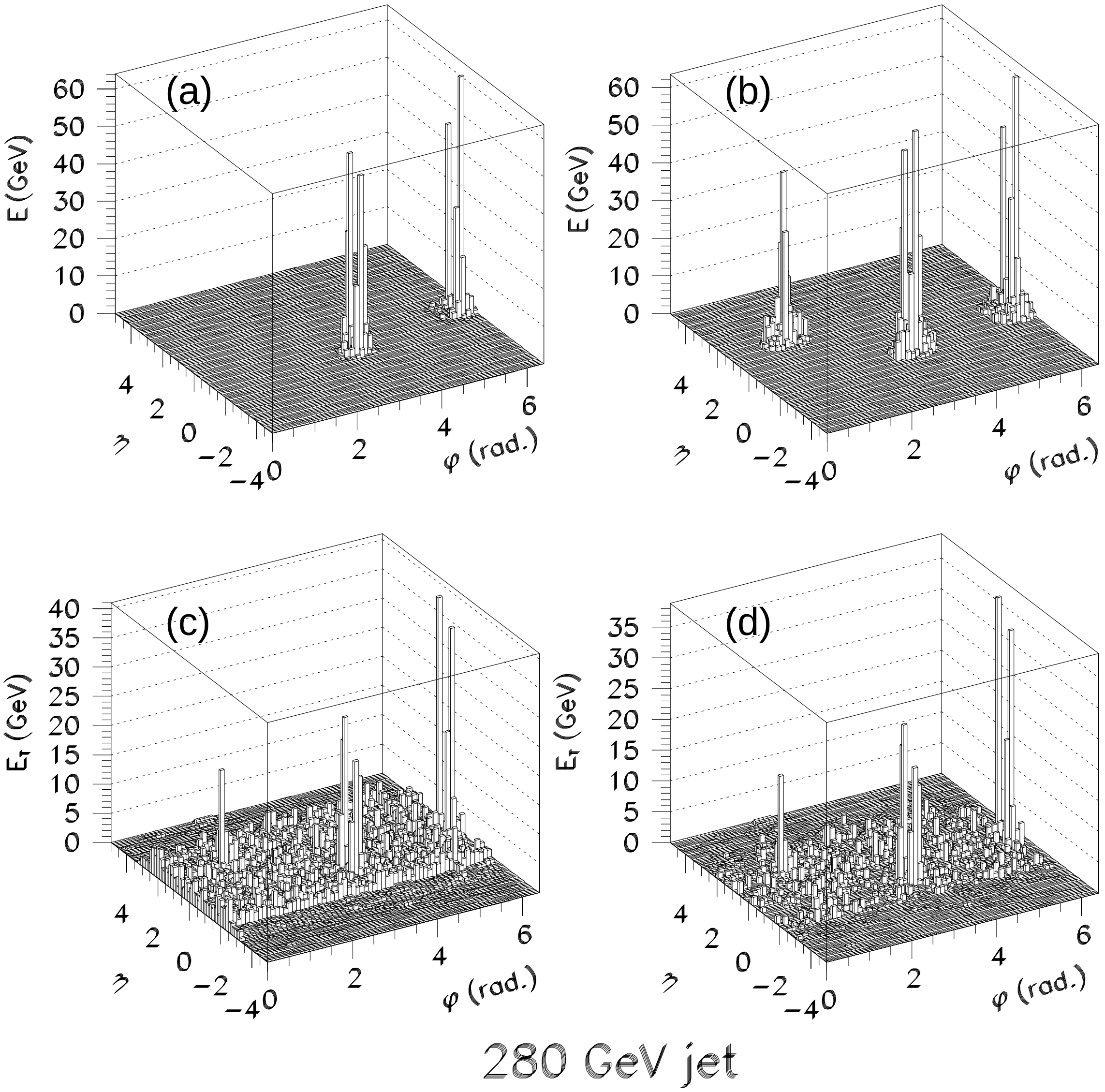

Figure 6.2: Illustration of the jet reconstruction algorithm. (a): reconstructed QCD di-jet event from PYTHIA in the pp environment; (b): the same QCD di-jet event reconstructed in the heavy-ion environment; (c) and (d): the same QCD di-jet event embedded in the HIJING background before and after background subtraction, respectively. Note that the vertical scale indicates energy (transverse energy) per tower in the top (bottom) plots. The di-jet event has been generated with a momentum transfer $\hat{p}_T^{hard} = 280$ GeV.

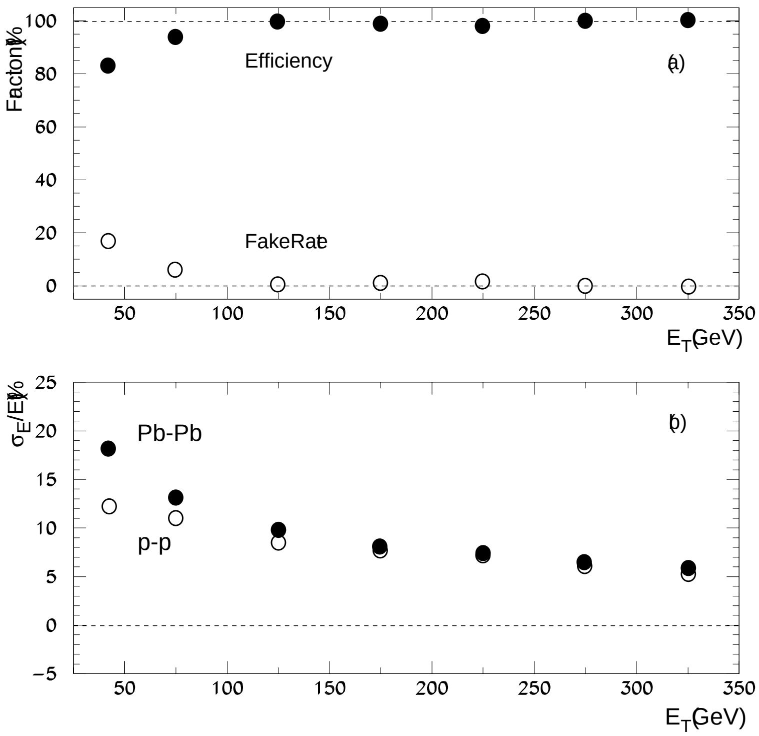

Figure 6.3: (a) The jet reconstruction efficiency (closed circles) and (an upper limit to) the rate of fake jets (open circles) as a function of the jet transverse energy, in central Pb-Pb collisions (see text for the definition of fake jets). (b) The jet energy resolution as a function of transverse energy for pp (open circles) and Pb-Pb (closed circles) events. Results are for unquenched jets reconstructed in cones of size $\Delta R = 0.4$.

6.4 Jet angular resolution

The fine calorimeter granularity in the transverse and longitudinal views allows a precise reconstruction of the jet direction using calorimetric information only. The result is shown in Fig. 6.4 for $E_T = 70$ GeV jets in the heavy-ion environment. The angular resolutions for this energy (averaged over $-3.2 < \eta < 3.2$) are $\sigma_\phi = 0.036$ rad and $\sigma_\eta = 0.045$.

6.5 Jet reconstruction using tracks

The possibility of reconstructing jets by using the information from the Inner Detector, alone or together with the calorimeter, can provide an additional handle to reject fake jets and improve the jet reconstruction efficiency, especially at low p_T.

A preliminary result of the jet reconstruction in the heavy-ion environment using tracks is shown in Fig. 6.5. Individual tracks can be reconstructed inside a jet with an efficiency of about 70% for a fake rate of typically 5%. The jet p_T shown in the Figure is defined as the sum of the transverse momenta of all tracks inside a cone of size $\Delta R =$ 0.4. An average shift of approximately 30 GeV is observed in heavy-ion events compared to pp events, which can probably be reduced by raising the

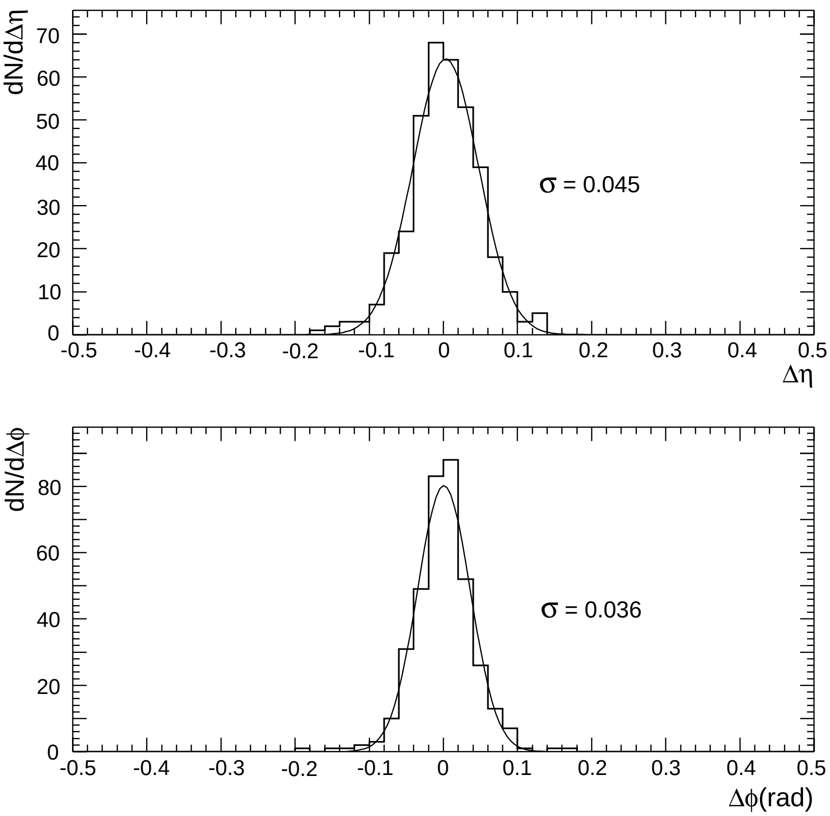

Figure 6.4: Angular resolutions in the η (top) and ϕ (bottom) directions for jets with $E_T = 70$ GeV and $|\eta| <$ 3.2 embedded in HIJING events.

track p_T threshold ($p_T \geq 1$ GeV has been used in this study).

First attempts to use individual charged tracks inside a jet to determine the jet fragmentation function, as well as to measure the neutral (π^0's) jet component, are discussed in Chapter 7. Both are expected to be very sensitive probes of quenching effects.

6.6 Conclusions and future plans

The study of jet reconstruction in the heavy-ion environment is currently in progress. The preliminary results reported here show good energy resolution and efficiency for E_T above 40 GeV. The resolution is worse than the intrinsic jet energy resolution of the ATLAS calorimeters, but close to the expected performance for pp collisions at high luminosity.

It should be noted that no special effort has been made at this stage to optimise the jet reconstruction in the heavy-ion environment, since similar algorithms to those developed for the cleaner pp events have been used. Improved and more suitable methods are under investigation. They should also allow the jet studies to be extended below $E_T \simeq$40 GeV, which is important because quenching effects may be larger at low energy.

As an example, ignoring at the jet-finding level the first compartment of the electromagnetic calorimeter may lead to a higher sensitivity to low-energy jets, since most of the background is

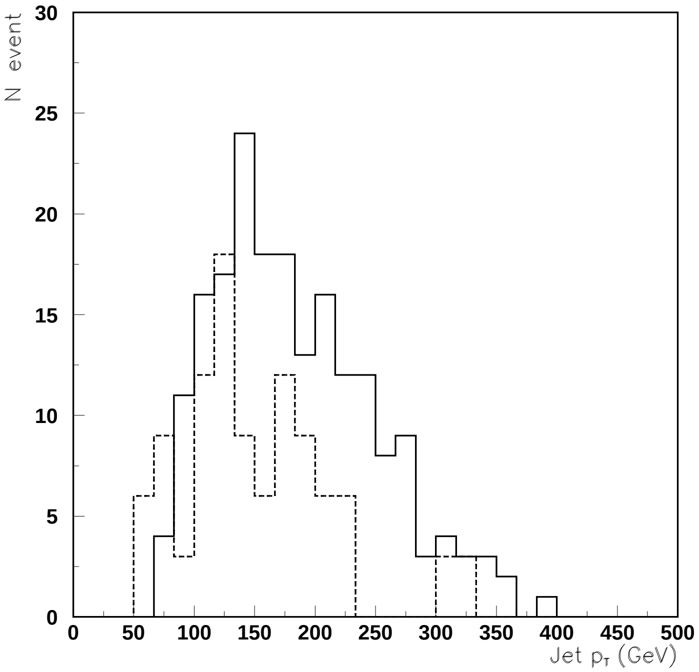

Figure 6.5: The jet p_T spectrum, as obtained using tracks reconstructed in the Pixels and SCT detectors for $WH \to \ell\nu u\overline{u}$ events. The dashed line shows the result for a PYTHIA WH sample, the full line for a PYTHIA WH sample embedded in an HIJING background sample.

absorbed by the front section of the detector. Obviously the removed energy will have to be added back for a correct reconstruction of the jet energy.

Furthermore, the combined information of the calorimeter and of the Inner Detector is potentially powerful, as already mentioned, especially at low energies, and should allow a detailed analysis of the jet properties.

An issue which needs to be addressed is the impact of possible azimuthal anisotropies in the background distribution. RHIC results [33] indicate that the asymmetry in the event energy flow, a memory of the original shape of the overlap volume between the two colliding nuclei, could be as large as 20%. Events including these effects are being studied.

Chapter 7

Jet Quenching

One of the key goals of the ATLAS heavy-ion programme is the detection and measurement of jet quenching, i.e. of the phenomenon by which hard-scattered partons radiate energy while traversing the dense coloured medium produced in nucleus-nucleus collisions. A quantitative determination of these radiative energy losses should probe directly the gluon density of the medium in the initial state, and may also provide sensitivity to the evolution of the hadronic matter into a quark-gluon plasma.

Experimental observables that are directly sensitive to the final, "quenched", parton are needed for a measurement of the radiative energy loss. By combining the information from these observables with a measurement of the total jet energy one can in principle determine both, the initial energy of the hard-scattered parton and the energy lost by the parton while propagating through the medium.

The reconstructed jet energy spectra and jet shapes could already provide useful constraints on the energy loss of the primary parton. However, theoretical predictions of the angular distribution of the radiated energy [34] indicate that much of this energy may lie within the angular range of the jet produced by the final quenched parton, and would thus get included in the region (e.g. a cone) used to reconstruct this jet. In the most extreme case where *all* of the radiated energy is contained inside the angular range of the jet produced by the final parton, the jet energy spectrum would show no modification relative to, e.g., pp collisions, even if the initial parton suffered substantial energy loss. To illustrate this problem, Fig. 7.1 shows a recent calculation of the energy angular distribution for jets with $E_T = 50$ GeV and $E_T =$ 100 GeV. In terms of jet shapes and jet energy spectra, the differences between the vacuum case and the QGP case are only of order 5-10%, and thus essentially unmeasurable.

On the other hand, more sizable effects are expected from the analysis of the individual fragmentation products. Indeed, the distribution of j_T, the transverse component (relative to the jet axis) of the momenta of the hadrons produced in the fragmentation, is predicted to be significantly broader in the presence of quenching effects [35].

Traditionally, the fragmentation of a parton is most often characterized via its single-particle fragmentation function, $D(z, Q^2)$. For a jet that results from a quenched parton plus some or all of the radiated energy, the apparent single-particle fragmentation function will be effectively softened at relatively large z,

$$D^{\mathrm{eff}}(z) \approx D\left(z \times \frac{E_{\mathrm{jet}}}{E_{\mathrm{jet}} - \Delta E^{\mathrm{jet}}_{\mathrm{q/g}}}\right), \tag{7.1}$$

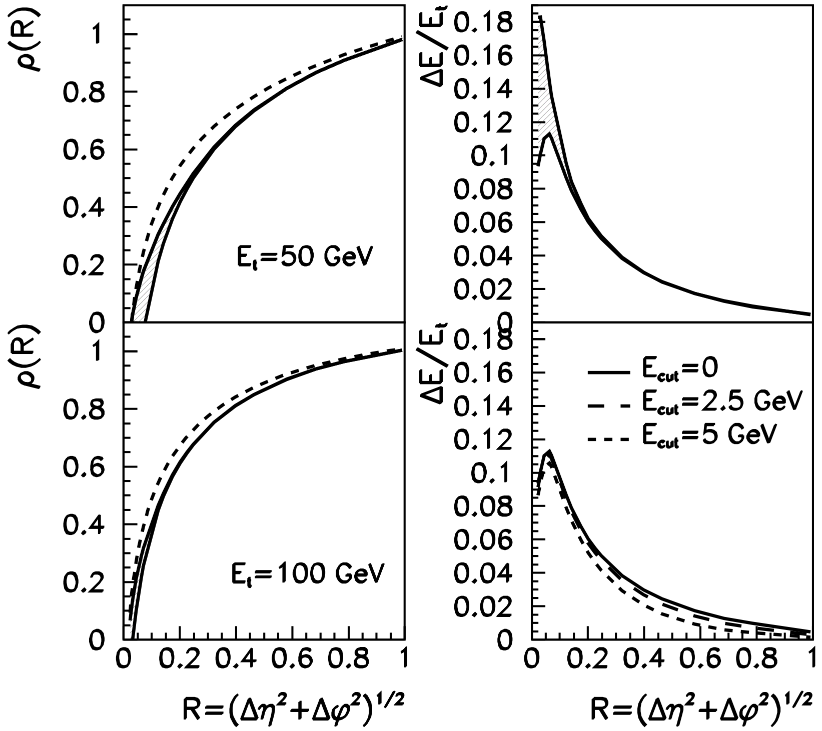

Figure 7.1: Left: the jet shape, defined as the jet energy fraction $\rho(R)$ contained inside a cone of size R, as a function of R, for $E_T = 50$ GeV and $E_T = 100$ GeV partons fragmenting in vacuum (dashed lines) or in a dense QCD medium (full lines). Right: for E_T=100 GeV partons, the average fraction of (medium-induced) energy loss outside a jet cone of size R, radiated away by gluons of energy larger than E_{cut} for three values of E_{cut}. The shaded areas indicate theoretical uncertainties. From Ref. [35].

where $\Delta E^{\mathrm{jet}}_{\mathrm{q/g}}$ is the radiative energy loss of the parton within the angular range of the jet and E_{jet} is the total energy observed in the jet.

One advantage of single-particle fragmentation measurements is that they are largely insensitive to the presence of the radiated gluons, because the probability for a gluon to be radiated in the z range of interest, $z > 0.3$, is non-zero but small. However, the fluctuations inherent to the fragmentation process (e.g. due to the large probability for collinear splitting of the leading partons) reduce the sensitivity of single-particle fragmentation measurements to the energy of the fragmenting parton. The yield of hadrons near the knee of the fragmentation function is most sensitive to the modification suggested by Eq. 7.1 [36], but hadrons at such large z values are produced in only a small fraction ($\sim$1%) of all jets.

It should be noted that the theoretical understanding of quenching at the LHC energies is still in the early stages of development. From the experimental point of view, this means that it is of utmost importance to demonstrate the ability to measure as many jet properties as possible in the heavy-ion environment.

Preliminary results are presented here of the ATLAS potential for the measurement of several observables potentially relevant for jet-quenching studies. These observables, which are discussed one by one in Sections 7.2-7.5, are:

- The jet fragmentation function, dN/dz, obtained from charged-particle tracks associated to the jet.
- The distribution of the component of the track momentum perpendicular to the jet axis (j_T), for tracks associated to the jet.
- The "jet core" transverse energy (E_T^{core}), defined as the total energy reconstructed in the calorimeters in a narrow ($R < 0.1$) angular cone at the centre of the jet.
- The energy spectrum of (partially) isolated neutral hadrons within the jet, reconstructed in the fine-segmented electromagnetic (EM) calorimeter.

In most cases, the above fragmentation variables will be affected by the large density of final-state particles in a heavy-ion collision. The impact of this background has been evaluated and the results are presented below. The sensitivity of the fragmentation measurements will also depend on the energy and angular resolution of the jet reconstruction algorithm itself. Some initial studies of this issue have been performed and are also reported below.

It should also be noted that a basic difference between Pb-Pb and pp collisions is that in non-central Pb-Pb collisions ($b >> 0$) the interaction is characterized by a "privileged" reaction plane, which is due to the non-symmetric (in ϕ) nuclear volume coming from the overlap of the initial nuclei. Recent results from RHIC [37] indicate that the suppression of high-p_T hadrons is stronger if the hadron is out of the reaction plane rather than in it. Therefore, since in-plane and out-of-plane jets may exhibit different amounts of quenching, future studies will also address the possibility to determine the reaction plane by using the calorimeter (and possibly also the Inner Detector) information.

Before discussing the fragmentation observables listed above, some estimates for the expected magnitude of the energy loss by energetic partons are given in the next Section, so as to set a benchmark against which the experimental sensitivity can be tested.

7.1 Magnitude of energy loss

Recent calculations [38] of parton energy losses, using both the GLV [39] and the BDMPS [40] formalisms, have shown that these two approaches give consistent results for jet energies above 50 GeV. Assuming initial gluon densities $dN^g/dy = 1000$, which are typical at RHIC energies and a factor 2-3 smaller than those estimated for the LHC (see Fig. 1.1), they obtain a fractional energy loss of approximately 25% for 50 GeV jets. The fractional energy loss is predicted to decrease as $\sim \log E/E$ so, for the same initial conditions, a 100 GeV gluon jet will lose $\sim$ 15% of its energy. The energy loss for quark jets will be a factor $4/9$ smaller.

Using the dependence of the parton energy loss on the initial gluon density from [38], one expects both quark and gluon energy losses to be a factor of 2-3 larger at the LHC than at RHIC. However, a conservative value of 10% for the average fractional energy loss of 100 GeV jets in central Pb-Pb collisions at the LHC has been assumed here, as a benchmark for the required experimental sensitivity of the fragmentation observables to changes in parton energy. With increasing jet energy above 100 GeV, the fractional energy loss decreases. A quantitative measurement of this decrease is essential to test the theory.

To quantify the sensitivity of the chosen fragmentation observables to changes in the parton energy, the following strategy could be adopted. First, the variation of each variable with the jet energy should be evaluated in pp collisions. Then, using this relationship, one can in principle infer, from a given fragmentation measurement in Pb-Pb collisions, the energy of the quenched fragmenting parton. This information, combined with the total energy of the jet, would allow a direct determination of the amount of energy radiated by the initial parton. However, because the fragmentation measurements are necessarily statistical, the ideal procedure described above cannot be practically implemented on a jet-by-jet basis. Instead, one can select (in Pb-Pb events) a set of reconstructed jets within a narrow energy range, plot the distribution of the fragmentation observable, and compare the result to the same measurement in pp collisions.

This and other approaches will be addressed in future studies.

7.2 Fragmentation function

The tracking capabilities of the ATLAS detector in the heavy-ion environment have been discussed in Chapter 5. The reconstruction efficiency for tracks with $p_T < 20$ GeV is ~ 70%, and the track momentum resolution is approximately 3%.

To extract fragmentation functions, jets with $E_T = 70$ GeV and $E_T = 100$ GeV were studied. PYTHIA di-jet events were embedded in HIJING central events, and jets were reconstructed using the method described in Chapter 6.

For each reconstructed jet, all the tracks within a cone of size $\Delta R = 0.4$ centered around the jet axis were considered. The jet axis was determined exclusively on the basis of calorimetric measurements (see Fig. 6.4). This method will be refined in the future by including also tracking information. For tracks within the jet cone, the fragmentation function dN/dz was reconstructed as a function of

$$z = p_T^{track}/E_T^{jet}.$$

In the heavy-ion environment, the jet cone contains many (background) tracks from the soft part of the event. Assuming an average charged particle multiplicity $< dN/d\eta_{ch} > \ \sim 3200$, there are on average about 250 such background tracks inside a $\Delta R = 0.4$ cone. However, the vast majority of them have $p_T << 1$ GeV, and are therefore rejected by the tracking algorithm used for these studies. The residual contamination of background tracks with $p_T \geq$1 GeV amounts to about 25 tracks per cone. This background can be subtracted statistically by reconstructing the fragmentation function far away from jet candidates. However, because these residual tracks have $p_T < 3-4$ GeV, for these preliminary studies it was decided to consider only tracks with $p_T > 3$ GeV.

The top panel in Fig. 7.2 shows the measured fragmentation function for jets of E_T=70 GeV in Pb-Pb collisions. The impact of various cuts on the track p_T is illustrated. As expected, these cuts remove mostly particles at the lower end of the distribution.

The results obtained with Pb-Pb and pp events are compared in the bottom panel of Fig. 7.2 for jets of $E_T = 70$ GeV, and in the top panel of Fig. 7.3 for $E_T = 100$ GeV jets. The track reconstruction inefficiencies in the heavy-ion environment ($\sim$30%) have been taken into account. The information from the Monte Carlo generator truth is also shown. Within the available statistics, the agreement between the performance obtained in Pb-Pb events and pp events (which will be

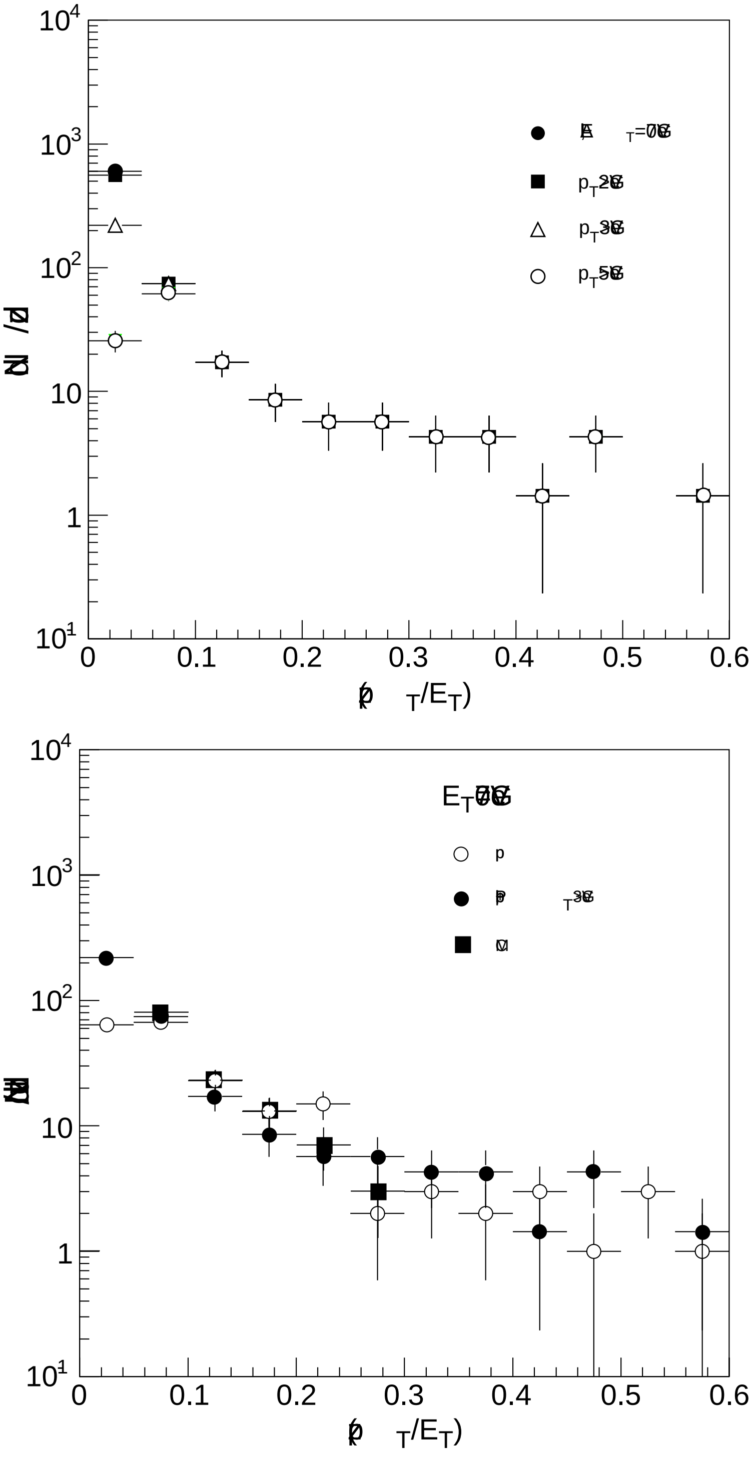

Figure 7.2: Measured fragmentation function of charged hadrons inside jets with $E_T = 70$ GeV in central Pb-Pb collisions. The top panel shows the impact of different cuts on the track p_T, and the bottom panel a comparison between Pb-Pb events (closed circles), pp events (open circles) and the Monte Carlo generator truth for Pb-Pb events (closed squares).

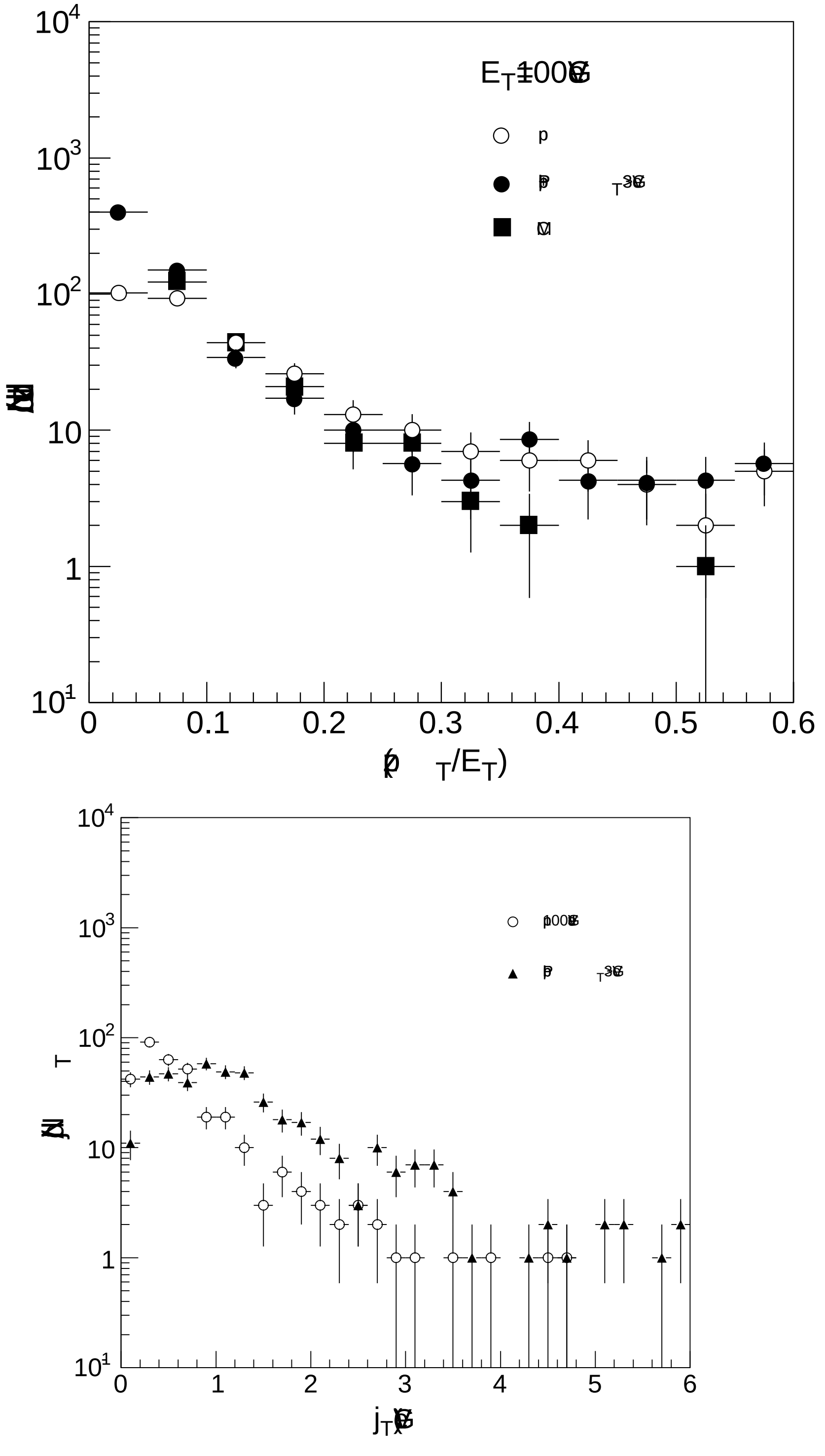

Figure 7.3: For jets with $E_T = 100$ GeV in central Pb-Pb collisions (closed symbols) and in pp collisions (open symbols), the measured fragmentation function (top panel) and j_T distribution (bottom panel) for charged hadrons inside the jet.

used as a reference sample) is reasonably good. This indicates that a measurement of the parton fragmentation function can be made in the busy heavy-ion environment, and that unquenched partons look similar in pp and Pb-Pb data reconstructed in the ATLAS detector. However, it remains to be demonstrated that this measurement can be performed to an overall accuracy of better than 10%.

One conclusion of this study is that the limitations of the measurement come, at the low end of the distribution, from the track p_T cut needed to reject the soft background, and at the high end from the increase in the percentage of fake tracks (see Section 5.1). The accessible z range is presently under study with jets of various transverse momenta, in order to assess more precisely the potential of this method [1]. However, as both RHIC results and the calculations in Ref. [35] suggest, the present range of sensitivity should already be adequate to observe quenching effects.

7.3 j_T distributions

The variable j_T is here defined as the transverse momentum of the track with respect toHERE the jet axis. The bottom panel in Fig. 7.3 shows the reconstructed j_T distributions obtained for jets of $E_T = 100$ GeV in pp and Pb-Pb events. Tracks were reconstructed and selected in exactly the same way as described in the previous Section.

The j_T spectrum for jets in the heavy-ion environment is significantly broader than for jets in pp events. This effect is most likely caused by a poorer jet-axis definition in the presence of the event background, but needs further investigations to be fully understood. In this example, a shift in the jet axis by 0.05 rad translates into a shift of $\Delta j_T = 0.5$ GeV for a 10 GeV track (z=0.1). To define the jet axis more accurately, one may need to include tracking information, and perhaps also ignore the energy deposited in the first layer(s) of the EM calorimeter.

More studies are required to assess the potential of this method.

7.4 $E_T^{\rm core}$ measurement

An alternative fragmentation measurement has been investigated, based on the energy deposited in the calorimeters in a narrow angular range ($R < 0.1$) at the "core" of a jet. Due to the limited but non-zero transverse momentum of fragmentation hadrons relative to the jet axis, only high-momentum (i.e. large-z) fragmentation fragments fall within such a narrow cone. Therefore, this variable is less susceptible to fluctuations in the fragmentation process than the single-particle fragmentation function, and is potentially more sensitive to the energy loss of hard-scattered partons.

The starting point in this study were EM clusters, reconstructed over a $\Delta\eta \times \Delta\phi = 0.125 \times 0.125$ region and with $E_T > 10$ GeV, to which the energy deposited in the hadronic calorimeter over a $\Delta\eta \times \Delta\phi = 0.2 \times 0.2$ region was added. In this preliminary analysis, the energies released in the longitudinal compartments of the calorimeters were simply summed, without applying optimized weights to improve the energy resolution. The angular range covered by the clusters in the EM calorimeter corresponds in area to an angular radius of ≈ 0.07 radians. The region included from the hadronic calorimeter corresponds to an angular region of radius $R = 0.11$. Since low-momentum hadrons deposit most of their energy in the EM calorimeter, the angular range of EM clusters is more relevant for evaluating the contributions from the radiated gluons and from the heavy-ion background to the $E_T^{\rm core}$ measurements.

---

[1] It is also planned to explore track matching to calorimeter clusters as an additional tool to reject fake tracks.

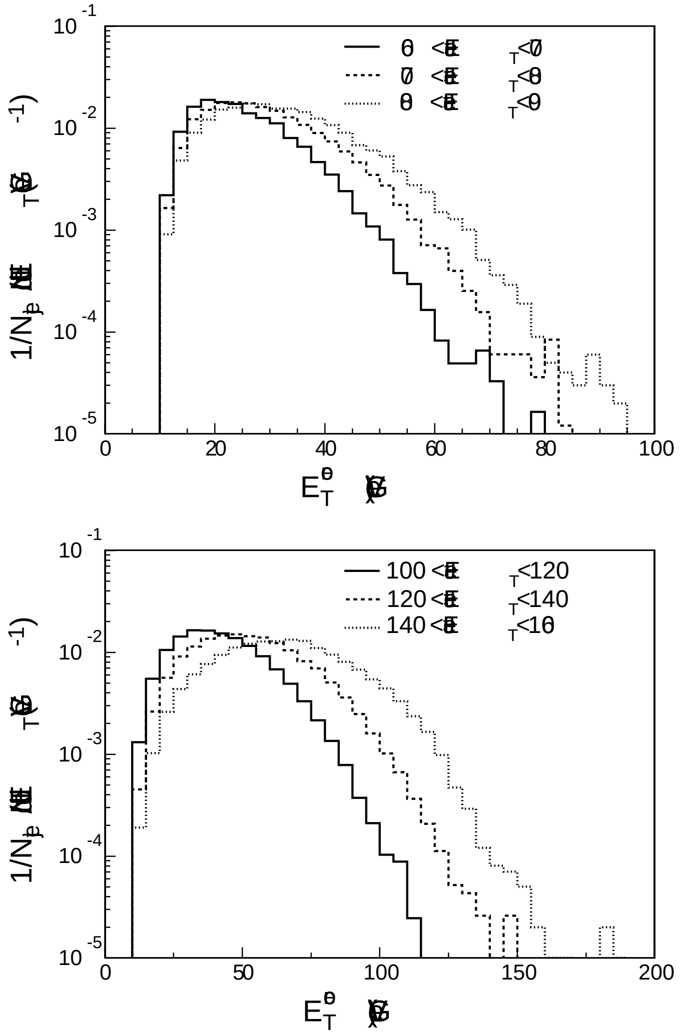

Figure 7.4: $E_T^{\rm core}$ distributions obtained for jets of varying energy in pp events.

Figure 7.4 presents $E_T^{\rm core}$ distributions obtained from jets of varying energy in pp collisions. As expected, these spectra show a rapid variation with increasing jet energy. The peak positions or the average values of the $E_T^{\rm core}$ distributions provide a simple estimate of the energy of the fragmenting partons. This is demonstrated in Fig. 7.5, which shows the variation of $\langle E_T^{\rm core}\rangle$ with the jet energy.

The $E_T^{\rm core}$ measurement will also be affected by the "background" in heavy-ion collisions. As for other studies reported in this document, a worst-case evaluation of the effect of the heavy-ion environment has been made by embedding PYTHIA jets in central Pb-Pb events. The correlation of $\langle E_T^{\rm core}\rangle$ with jet energy has then been studied, without attempting to perform a background subtraction in either the EM or hadronic calorimeters. The results are shown in Fig. 7.5, in comparison to the results obtained from jets in pp collisions. The difference between the $E_T^{\rm core}$ measurements obtained from the pure PYTHIA events and from the mixed events decreases with increasing jet energy, as expected. This difference could be removed also at low energy by applying a background

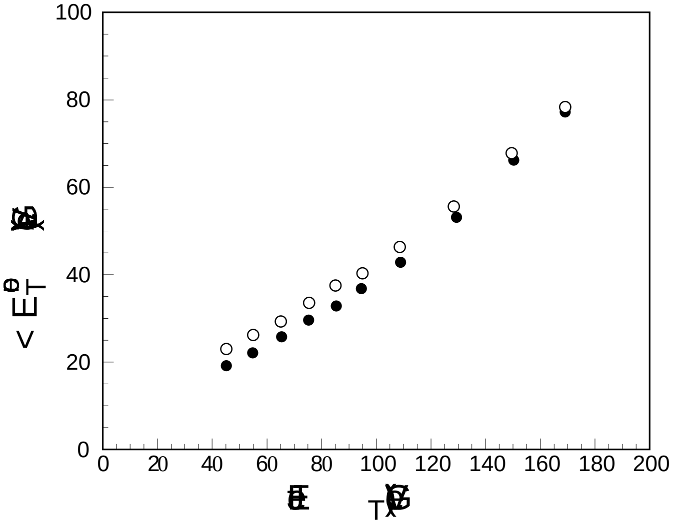

Figure 7.5: Variation of $\langle E_T^{\rm core} \rangle$ with the jet transverse energy for PYTHIA jets in pp collisions (dots) and for these same jets embedded in central Pb-Pb events (open circles).

subtraction procedure, as described in Chapter 6. However, it is first important to minimize the sensitivity of the $E_T^{\rm core}$ distributions to the background (e.g. by optimizing the threshold cuts applied to the calorimeter cell energies), in order to reduce the impact of the background fluctuations on the measurement. These issues are still under investigation.

Figure 7.5 indicates that a (conservative) 10% energy loss by quenching from partons with initial $E_T \simeq$100 GeV would produce a similar decrease of about 10% in the measured value of $\langle E_T^{\rm core} \rangle$. Such a decrease is larger than the expected systematic uncertainty on the $\langle E_T^{\rm core} \rangle$ measurement.

7.5 Jet fragmentation via isolated neutral hadrons

Detection of energetic π^0's and η's in ATLAS is possible due to the small opening angle of the photons in the $\gamma\gamma$ decay of these hadrons at moderate to high p_T. While the reconstruction of π^0's and η's in isolation may be straightforward, the reconstruction of these hadrons within a jet is much more challenging, because of the presence of overlapping charged and neutral hadrons, as shown in Fig. 7.6. This problem becomes more serious with increasing jet energy, due to the increased collimation of the jets.

Nonetheless, a way was found to select a class of isolated neutral hadrons, whose energy can be measured with good precision. The study was first performed with isolated PYTHIA jets, and only at a second stage were HIJING Pb-Pb events added. Figure 7.7(a) shows a distribution of relative error in the measurement of the energies of isolated neutral hadrons and photons from jets with $E_T > 75$ GeV. These clusters were selected by applying transverse and longitudinal shower shape cuts in the EM and hadronic calorimeters. It was also required that the clusters lie within an angular range $\Delta R < 0.1$ of the parent jet. The peak containing correctly measured neutral hadron energies has a Gaussian width of 2.5% using the restricted fit shown in the Figure. The tail to larger relative errors consists almost entirely of clusters resulting from overlapping neutral hadrons that are not

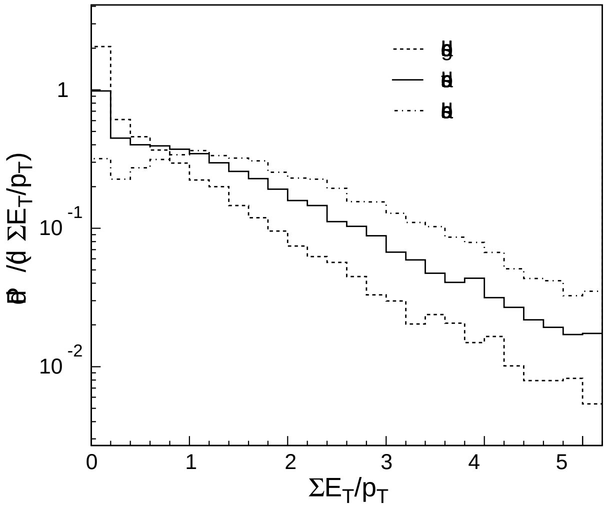

Figure 7.6: Distribution of the transverse energy of charged, neutral, and all hadrons overlapping a neutral hadron, divided by the transverse momentum of the neutral hadron, for the fragmentation of jets with $E_T > 75$ GeV and with neutral hadron $p_T > 15$ GeV in pp events. The overlap criterion is that the hadrons lie within an angular range $\Delta R < 0.075$ of the neutral hadron.

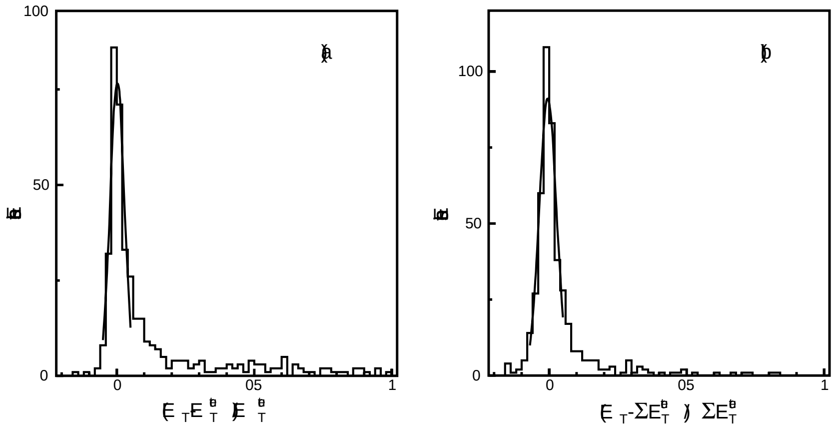

Figure 7.7: Relative error in the measurement of the transverse energy of isolated EM clusters with $E_T(\mathrm{cluster}) > 50$ GeV and $|\eta| < 2.4$ from jets with $E_T > 75$ GeV in pp events. (a) The measured E_T is compared to the true E_T of the input neutral hadron that has the smallest ΔR from the reconstructed cluster. (b) The measured E_T is compared to the sum of the true transverse energies for all overlapping neutral hadrons. The Gaussian fits shown have $\sigma = 2.5\%$ in (a) and $\sigma = 3.5\%$ in (b).

rejected by the isolation cuts. Figure 7.7(b) shows a distribution of relative error in the measurement of the total transverse energy of all neutral hadrons within an angular range $\Delta R < 0.075$. In this distribution, the large-error tail is significantly reduced; $\sim 10\%$ of the counts lie more than 3σ above the centre of the Gaussian peak, to be compared to 33% in Fig. 7.7(a). If the definition of the fragmentation observable is modified to be the total transverse energy of all isolated neutral hadrons falling within a cone of $\Delta R = 0.075$, then the measurement of this observable can be performed with a resolution of a few percent.

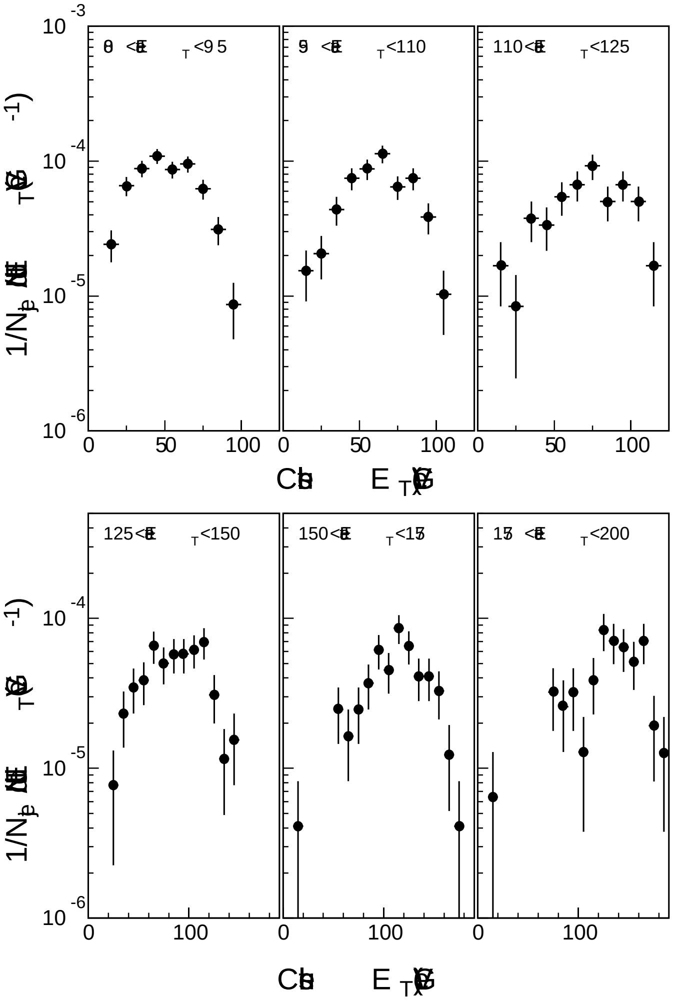

Figure 7.8: Energy spectra of isolated EM clusters with $E_T(\mathrm{cluster}) > 10$ GeV in the fragmentation of jets of different energy in pp events. The spectra give the cluster yield per jet and per GeV in 10 GeV bins.

In order to evaluate the sensitivity of this fragmentation observable to radiative energy losses, the isolated EM cluster energy spectra are plotted in Fig. 7.8 for different ranges of jet energy. The isolated cluster energy distributions look quite different from the approximately exponential single-particle fragmentation functions shown e.g. in Fig. 7.2. The broad peak at large E_T values results from a competition between the increasing probability to find an isolated cluster with increasing z and the rapidly decreasing single-particle fragmentation function. The likelihood that a neutral hadron will satisfy the isolation cuts increases with hadron z, because as the hadron takes a larger fraction of the jet energy, the remaining hadrons will necessarily carry a smaller fraction of the jet momentum, and thus will be distributed over a larger angular range. The effectiveness of this angular spreading,

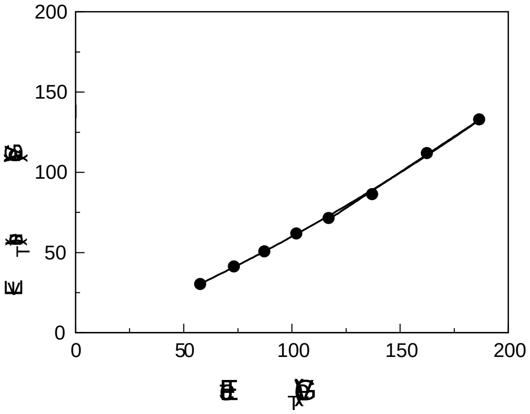

Figure 7.9: The average transverse energy of isolated EM clusters as a function of the parent jet energy (pp events). The line shows a second order polynomial fit to the points.

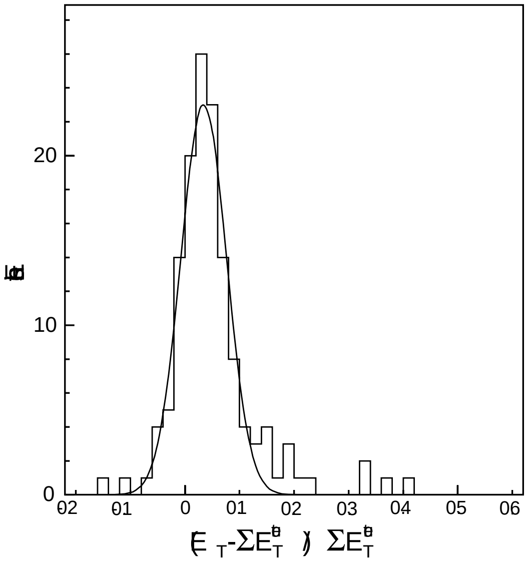

Figure 7.10: Relative error in the measurement of the energy of overlapping neutral hadrons (and photons) with total transverse energy above 50 GeV from jets with $E_T > 75$ GeV, in Pb-Pb central events. The Gaussian fit shown has σ = 4.5%.

however, decreases with increasing jet energy, which means that a larger fraction of the jet energy must be taken by the leading neutral hadron for it to remain "isolated".

The average energy of isolated EM clusters is shown in Fig. 7.9 as a function of the jet energy. The deviation from a purely linear dependence is explained by the kinematic arguments above. However, since the isolated EM clusters typically account for more than 50% of the jet energy, they are directly sensitive to the energies of their parent partons. Thus, provided sufficient statistics is available, and ignoring instrumental systematic effects, the average energy of the final fragmenting parton can in principle be measured, for a given bin in total jet energy, with arbitrarily good precision. Typically this analysis selects isolated clusters in $\leq 1\%$ of jets. The RMS values of the isolated cluster E_T distributions vary from 20 GeV for the lowest jet energies considered in Fig. 7.9 to 30 GeV for the highest jet energies. Therefore, to obtain an estimate of the mean value of the isolated EM cluster E_T distribution for jet transverse energies in the range 100-110 GeV with 10% statistical precision, only a few tens of events are need. These simple studies need to be pursued to evaluate more precisely the impact of the very low expected rates of jets with such a highly electromagnetic content and of the systematics (which need to be controlled to a few %).

To evaluate the performance of the above analysis in heavy-ion collisions, the simulated PYTHIA jets were embedded into central ($b = 0 - 1$ fm) HIJING events. The most obvious concern in these conditions is the effect of the background event on the measurement of the cluster energy. Figure 7.10 shows the energy resolution for isolated clusters in heavy-ion events, using the summed energy of all overlapping neutral hadrons as the benchmark for the energy measurement (see above). The heavy-ion background produces a small change (3.5% → 4.5%) in the resolution of the measured clusters.

Due to the difficulty of embedding large samples of jets into Pb-Pb events, the presently available statistics is not sufficient to determine the shapes of the isolated cluster E_T distributions in Pb-Pb events. In addition, the isolation criteria need to be re-optimized to account for the presence of the heavy-ion background. These are outstanding issues which need further studies.

Chapter 8

Probes of Deconfinement: Quarkonia Suppression

Dissociation of heavy-flavour bosons is another very promising signature of QGP formation [41] that can potentially be studied with the ATLAS detector. This phenomenon is linked to the saturation of the long-range attractive potential in a QCD medium. Color screening effects prevent the various ψ, Υ, χ states to be formed when the color screening length becomes smaller than the size of the resonances. Thus, observation of the suppression of these states provides crucial tests of the nuclear potential.

The evidence for J/ψ suppression reported by the NA50 CERN experiment [42] at $\sqrt{s}$=17.3 GeV per nucleon pair raised a large interest for this kind of studies, although the interpretation is still a subject of debate. At the LHC, in addition to the J/ψ family, the Υ family will also be accessible, which will allow the study of c and b quarkonia states with a large variety of binding energies, and thus provide more powerful tests of screening effects in a saturated color potential.

The possibility of observing quarkonia production in ATLAS, and their possible suppression by a QGP formation, is the subject of this Chapter. Only decays of the resonances into muon pairs are considered, since these offer clear trigger and experimental signature.

8.1 Υ mass reconstruction

The intrinsic di-muon mass resolution of the ATLAS detector was studied with single Υ decays into muon pairs over the region $\mid \eta \mid \ < 2.5$. A sample of 5000 $\Upsilon \rightarrow \mu^+\mu^-$ events were generated with an inverse p_T slope of 240 MeV. These events were then processed through the GEANT3 full simulation, and reconstructed with the ATLAS Muon Spectrometer reconstruction package Muonbox [1] and the Inner Detector reconstruction package xKalman (see Section 5.1).

As the standalone Muon Spectrometer provides an insufficient mass resolution (approximately 460 MeV) to separate the various Υ states, muon candidates reconstructed in the Muon Spectrometer were matched to tracks in the Inner Detector (reconstructed using the information of the Pixels and SCT). The matching was done by a selection on the χ^2 of a global track fit between the different detectors, keeping the best combinations. In addition, a χ^2 cut and a geometrical $\Delta\phi \times \Delta\eta$ cut were applied, where $\Delta\phi$ and $\Delta\eta$ are the differences in azimuthal angle and pseudo-rapidity between Inner Detector tracks and Muon-Spectrometer tracks after back-extrapolation to the vertex. The quality of the matching can be deduced from Figs. 8.1a, 8.1b and 8.2a, where R is defined as

$R = \sqrt{\Delta\phi^2 + \Delta\eta^2}$, while Fig. 8.2b shows the χ^2 of the best association. The p_T and pseudo-rapidity distributions of the reconstructed muons from the Υ decay are shown in Figs. 8.3a and 8.3b.

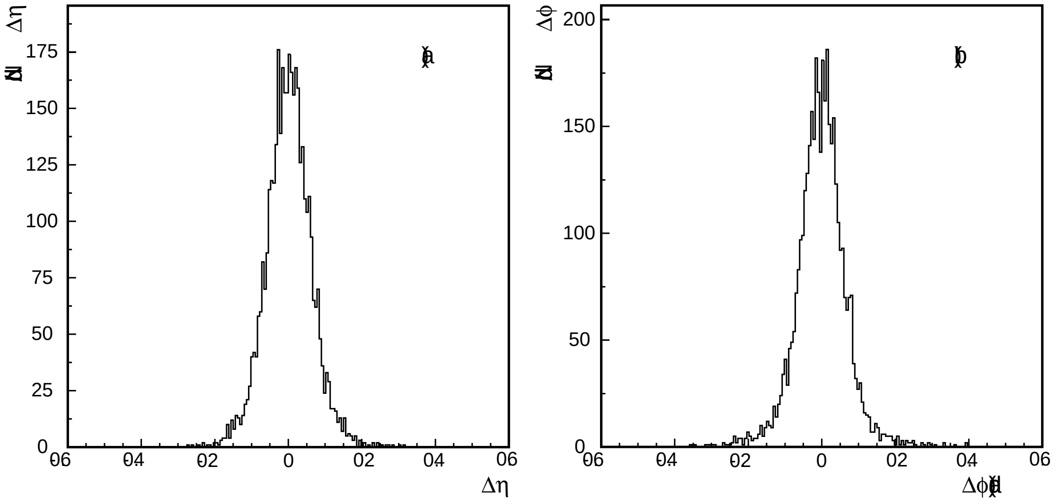

Figure 8.1: For muons from Υ decays, the pseudo-rapidity (a) and the azimuthal (b) difference between tracks reconstructed in the Inner Detector and in the Muon Spectrometer, after back-extrapolation to the vertex.

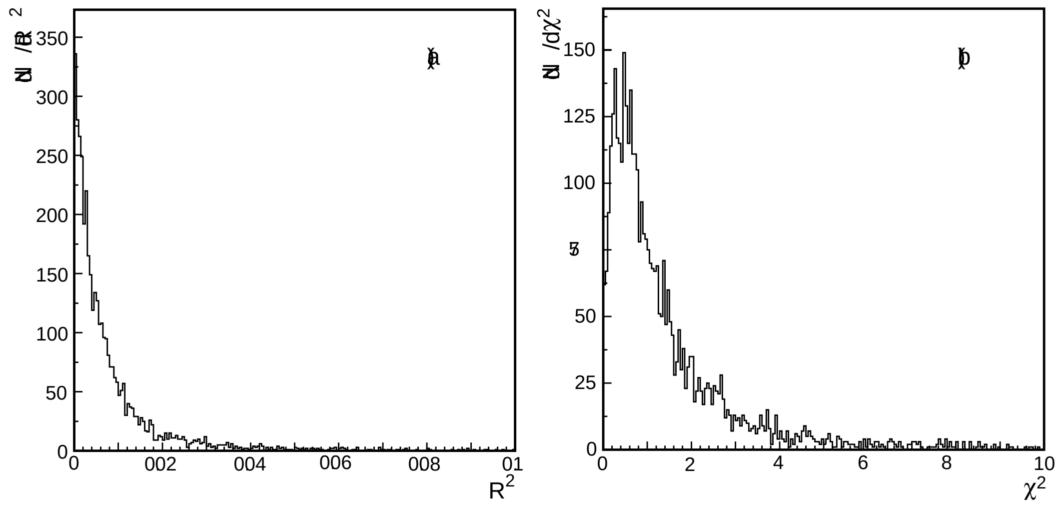

Figure 8.2: For muons from Υ decays, (a) the radial difference between tracks reconstructed in the Inner Detector and in the Muon Spectrometer, after back-extrapolation to the vertex, and (b) the χ^2 distribution of the global track fit.

For further analysis, a set of rather loose selection cuts was chosen, namely a geometrical cut $R < 0.25$, a cut $\chi^2 < 5$ and a cut on the muon transverse momentum $p_T > 3$ GeV. The total

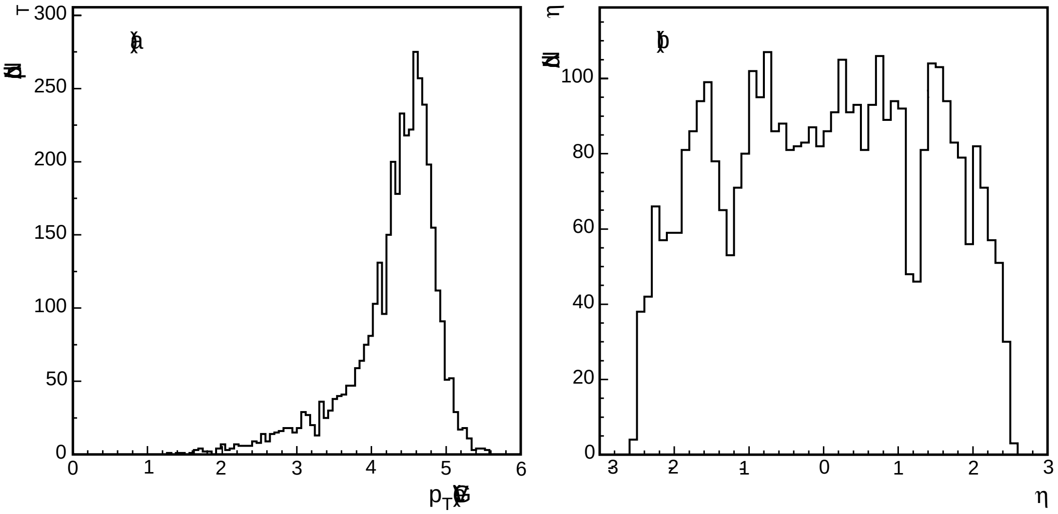

Figure 8.3: Transverse momentum (a) and pseudo-rapidity (b) distributions for muons from Υ decays.

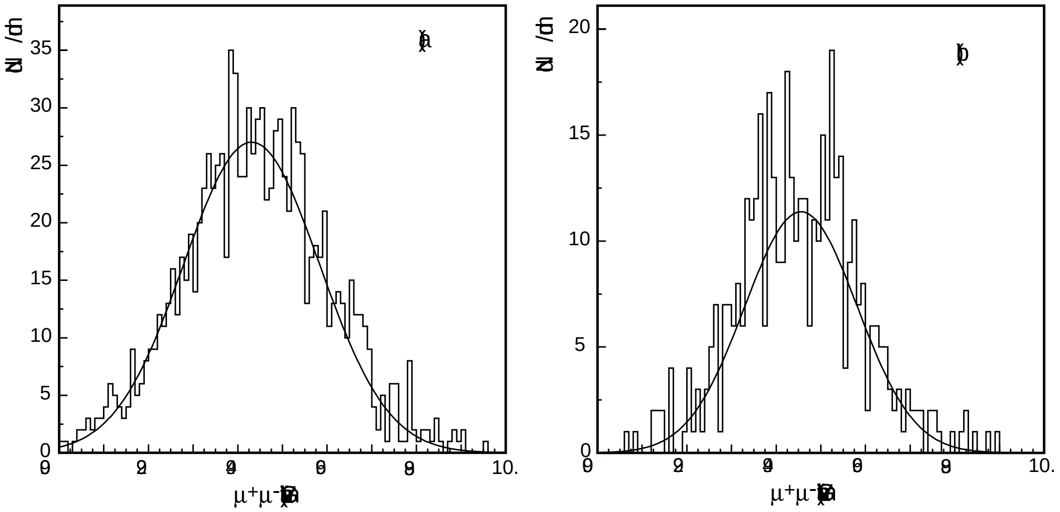

Figure 8.4: The reconstructed di-muon mass spectrum for muons from Υ decays obtained over (a) the full detector ($|\eta| < 2.5$) and (b) the central part only ($|\eta| < 1$).

acceptance of these cuts, including the muon reconstruction efficiency, is 22%, and the di-muon mass resolution is 152 MeV (Fig. 8.4a). The combined mass resolution is entirely determined by the Inner Detector at these low momenta, and is limited by multiple scattering in the tracker material. However, the Muon Spectrometer is essential for trigger and muon identification purposes. If only muons in the central pseudo-rapidity region $\mid \eta \mid$<1 are considered (where the amount of material in the Inner Detector is smaller), the mass resolution improves to 126 MeV (Fig. 8.4b) but the total acceptance decreases to 8.7%.

Figure 8.5 shows the di-muon mass resolution and the (integrated) event acceptance and recon-

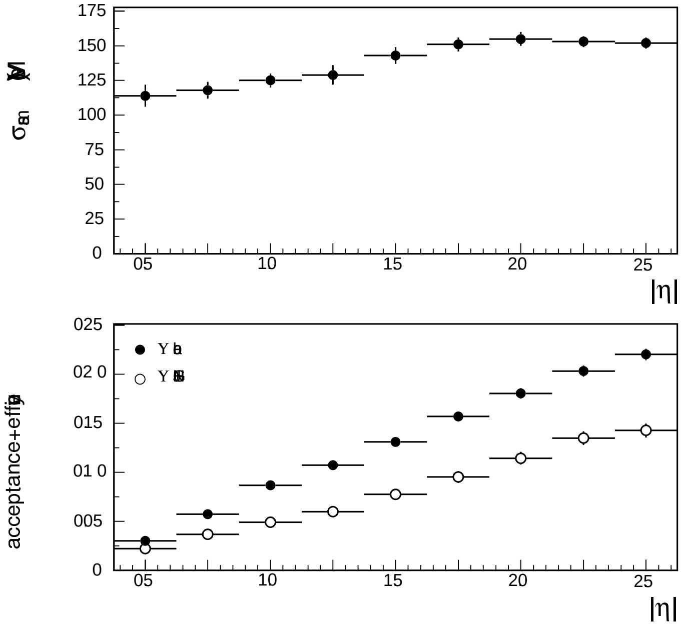

Figure 8.5: The Υ mass resolution (top) and the integrated Υ selection efficiency after cuts (bottom), as a function of the pseudo-rapidity acceptance of the decay muons. Results for isolated Υ (closed circles, see Section 8.1) and for Υ embedded in HIJING events (open circles, see Section 8.3) are shown.

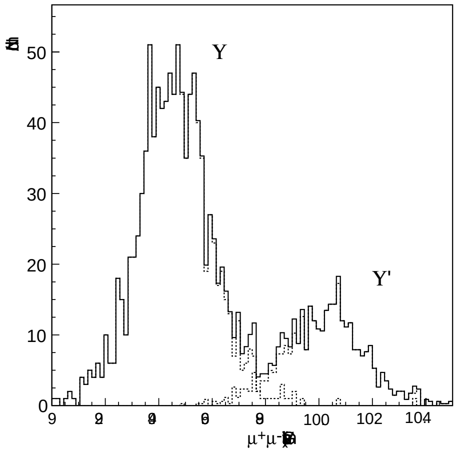

Figure 8.6: The reconstructed $\mu^+\mu^-$ invariant mass distribution for muons with $| \eta | < 1$ in the Υ-Υ' region. The two resonances are indicated by the dashed histograms.

struction efficiency after selection, as a function of the pseudo-rapidity cut on the decay muons (see Section 8.3 for comments on the impact of the HIJING background). It is clear that a compromise has to be found between the overall rate of accepted events and the mass resolution, which vary in opposite directions when the pseudo-rapidity acceptance of the decay muons increases, in order

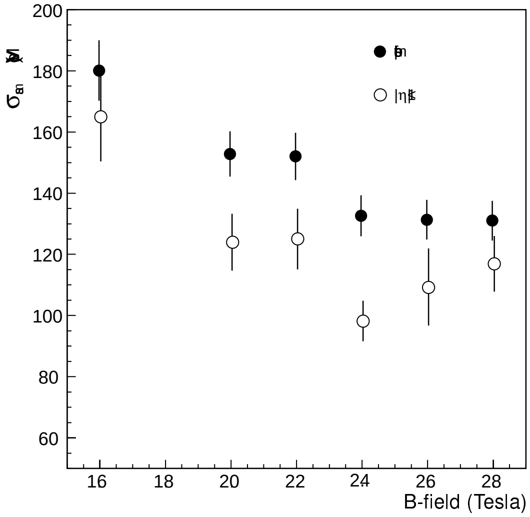

Figure 8.7: $\Upsilon \rightarrow \mu^+\mu^-$ mass resolution as a function of the magnetic field in the solenoid for muons with $|\eta| < 2.5$ (dots) and $|\eta| < 1$ (triangles).

to separate Υ from Υ' in a clean way and with maximum statistics. As an example, the separation between the Υ and Υ' resonances obtained with muons inside $\mid \eta \mid$<1 can be appreciated from the plot in Fig. 8.6. Such a clear separation is not achievable in the forward regions. Further studies are however needed to optimise the muon pseudo-rapidity acceptance.

A few additional checks were performed. With only two Pixel layers, as foreseen in the initial (staged) layout of the Inner Detector, the mass resolution improved slightly because of the smaller amount of material. Applying even looser selection cuts than those described above, i.e. $R < 0.5$, $\chi^2 < 10$ and $p_T > 1.5$ GeV, increases the acceptance only slightly, namely to 24% (9.2%) for the full detector (central part). Finally, for illustration, the Υ mass resolution is shown in Fig. 8.7 as a function of the solenoid magnetic field.

8.2 Background studies

Background events were generated with HIJING 1.38, were processed through a full GEANT3 simulation, and were reconstructed with the tools described in Section 8.1. This detailed simulation makes sure that local high multiplicities and possible detector saturation effects (see Section 4.1) are taken into account. A total of 5000 central ($b < 1$ fm) Pb-Pb collisions were produced.

Most of the muons in these background events come from in-flight decays (i.e. before absorption in the calorimeters) of π and K (indirect muons), and from c and b decays directly at the vertex (direct muons). The direct muons have on average a larger p_T than the indirect ones, therefore the ratio of direct/indirect muons depends on the p_T cut used in the analysis. Because secondary tracks from particles decaying away from the initial vertex usually produce kinks, geometrical and χ^2 cuts, in addition to p_T cuts, are quite efficient to suppress indirect muons. This is illustrated in Figs. 8.8 and 8.9. These plots were made for all muon candidates with $R < 0.5$ after the global fit, and can be compared with the distributions obtained in very similar conditions for the Υ signal (Figs. 8.1 and 8.2). The latter show cleaner matching properties than the former, thanks to the absence of π/K decays.

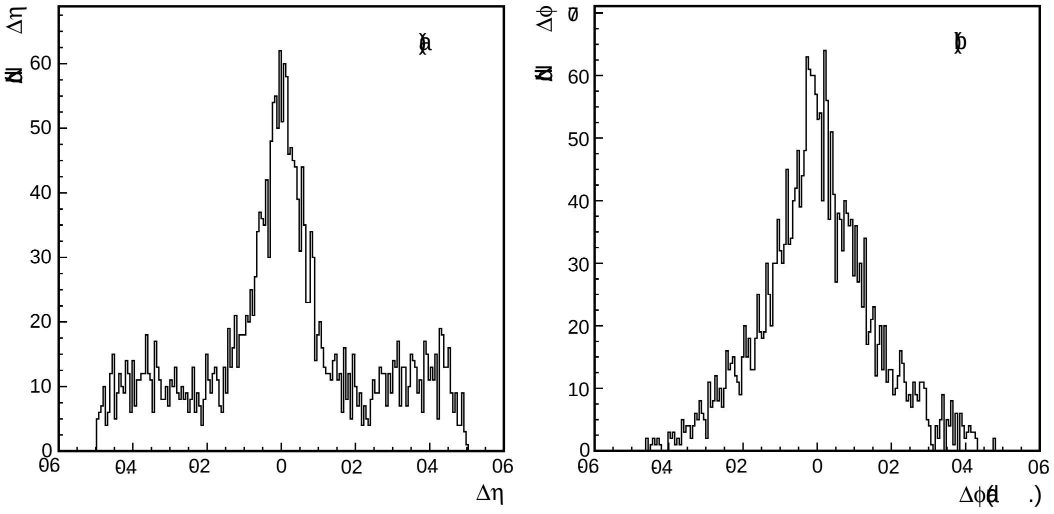

Figure 8.8: For background muons from central HIJING, the pseudo-rapidity (a) and the azimuthal (b) difference between tracks reconstructed in the Inner Detector and in the Muon Spectrometer, after back-extrapolation to the vertex.

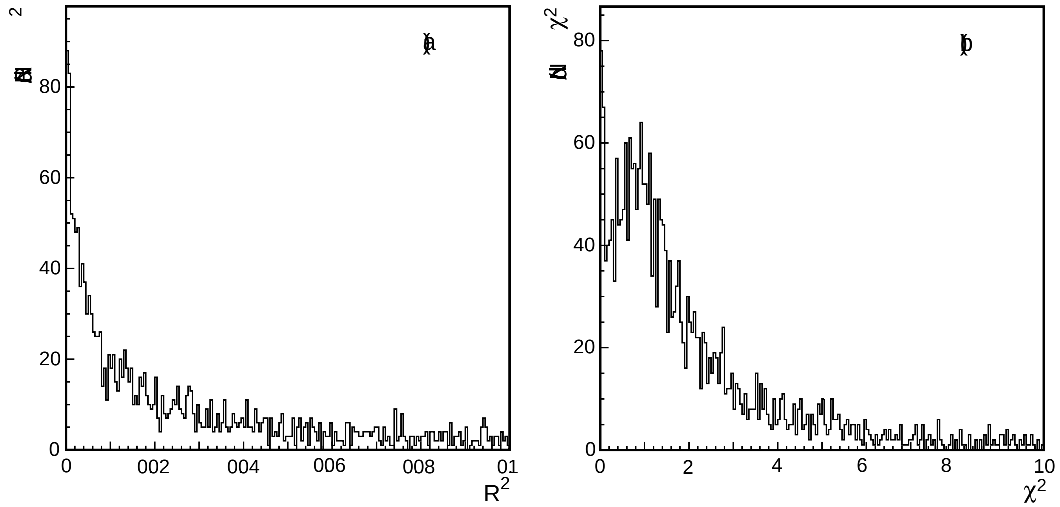

Figure 8.9: For background muons from central HIJING events, (a) the radial difference between tracks reconstructed in the Inner Detector and in the Muon Spectrometer, after back-extrapolation to the vertex, and (b) the χ^2 distribution of the global track fit.

Figure 8.10 shows the p_T and pseudo-rapidity distributions of the reconstructed muons. Again, these distributions are quite different from those obtained for muons from Υ decays (Fig. 8.3). In particular, a p_T cut in the 3-3.5 GeV range is quite effective to separate the Υ signal from the background. The two peaks at large $|\eta|$ in Fig. 8.10b are due to low-p_T muons, and are considerably reduced after a $p_T > 3$ GeV cut is applied.

After the selection cuts described in the previous Section are applied to this background sample, the number of reconstructed muons is reduced to 0.17 muons per event on average. Compared to the number of muons initially reconstructed in the Muon Spectrometer alone over $|\eta|$ <2.5, the background muons after these cuts are reduced by a factor 4.8, out of which a factor 2.1 comes from the p_T cut and a factor 2.3 from the matching to Inner Detector tracks. The average number of reconstructed $\mu^+\mu^-$ pairs per central event was found to be 0.011. This includes both correlated and uncorrelated muon pairs, the latter amounting to less than 0.01 per event. No cut on the di-muon invariant mass has yet been applied at this stage.

Due to the small statistics of surviving muons, the shape of the di-muon mass distribution for the background sample was obtained with a mixed-event technique, where the two muons were taken from two different events. As a consequence, this method provides only the mass shape of uncorrelated muon pairs. The result is shown in Fig. 8.11.

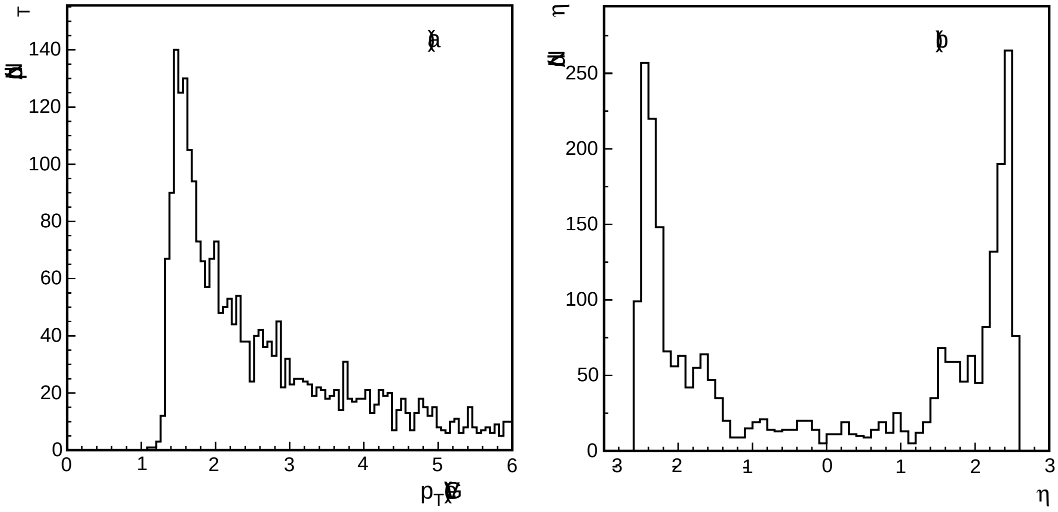

Figure 8.10: Transverse momentum (a) and pseudo-rapidity (b) distributions for reconstructed background muons from central HIJING events.

The fraction of direct muons in the sample surviving the above-mentioned set of cuts was found to be 40%, increasing to 48% if the geometrical cut is tightened from $R < 0.25$ to $R < 0.1$. The background after cuts is therefore still dominated by π and K decays.

Finally, it was also checked that the global fit associates correctly the muon track found in the Muon Spectrometer to an Inner Detector track coming from a direct or indirect muon. This is the case for 93% (80%) of the muon candidates with $|\eta| < 1$ ($|\eta| < 2.5$) passing the above selections, and for 98% (91%) of the candidates passing a tightened $R < 0.1$ geometrical cut.

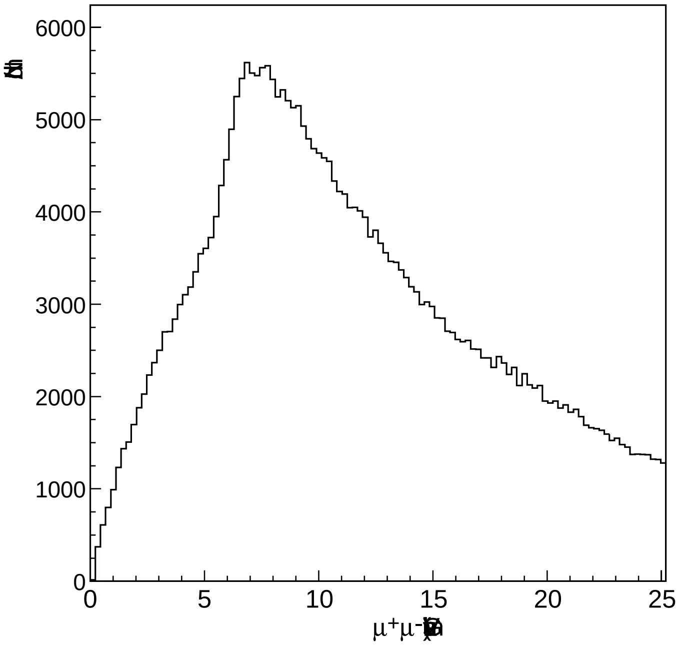

Figure 8.11: Reconstructed di-muon mass spectrum for muons from central HIJING events, as obtained with a mixed-event technique (see text).

8.3 $\Upsilon \rightarrow \mu\mu$ inside central Pb-Pb events

The capability of reconstructing Υ decays in complete heavy-ion events was studied by merging the two samples discussed in the previous Sections, namely single $\Upsilon \rightarrow \mu^+\mu^+$ events and central Pb-Pb HIJING events.

Figure 8.12 shows the reconstructed $\mu^+\mu^-$ invariant mass distribution for a sub-sample of these combined events. The Υ mass resolution was found to be 147±11 MeV for muons inside the full acceptance ($|\eta| < 2.5$), and 122±9 MeV for muons inside $|\eta| < 1$. This performance is similar to that obtained with single Υ events (see Section 8.1). The signal purity in the mass region 9.1-9.8 GeV, defined as the fraction of muon pairs with both muons coming from the Υ, ranges between 91% and 95%, depending on the analysis cuts (94% to 99% for muons with $|\eta| < 1$). These values do not take into account the Υ' contamination in the Υ mass region.

The Υ reconstruction efficiency, which is displayed in Fig. 8.5, is reduced by about 40% for these complete events, as compared to the case of single Υ events. The origin of this degradation, which comes mainly from the Muon Spectrometer, is presently not understood and is still under investigation (it may be due to a software technical problem). Nevertheless, the results obtained with the merged events (represented by triangles in Fig. 8.5) have been used to estimate production rates and signal-to-background ratios.

8.4 Production rate and signal-to-background ratio

The $\Upsilon \rightarrow \mu^+\mu^-$ cross-section at the LHC energies can be estimated by linear extrapolation of the CDF data from $\sqrt{s}$=1.8 TeV [43] to $\sqrt{s}$=5.5 TeV. The extension from $p\overline{p}$ collisions to AA collisions

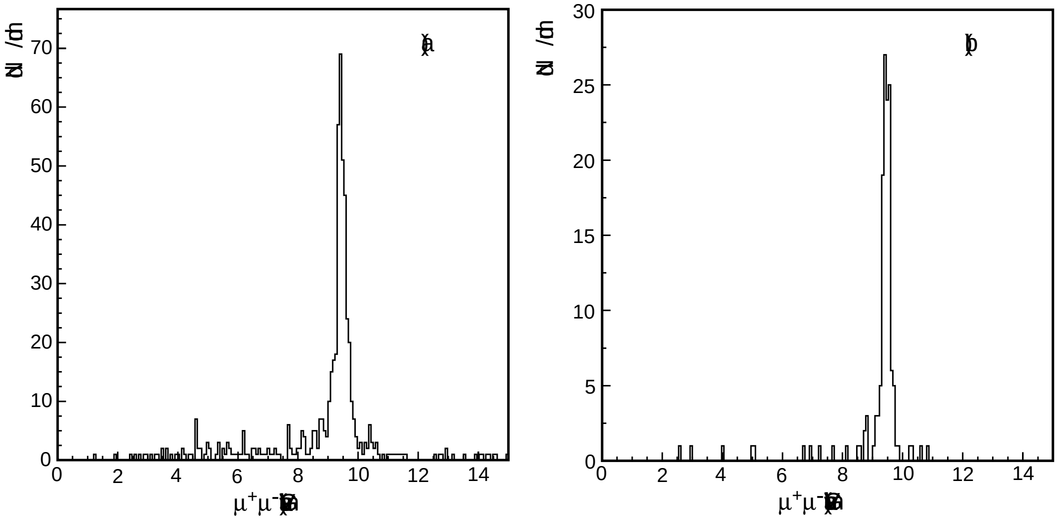

Figure 8.12: Reconstructed di-muon invariant mass distributions for Υ events embedded in central Pb-Pb events, over (a) the full detector acceptance and (b) the region $|\eta| < 1$.

is then obtained by using the A-scaling law

$$\left[\frac{d\sigma(AA)}{dy}\right]_{y=0} = A^{2\alpha}\left[\frac{d\sigma(p\overline{p})}{dy}\right]_{y=0} \tag{8.1}$$

with α=0.95 for b-states [44]. Following calculations performed by CMS [45], values of cross-section times branching ratio of $B_r d\sigma/dy(Pb-Pb \rightarrow \Upsilon \rightarrow \mu^+\mu^-) =$ 410 μb, $B_r d\sigma/dy(Pb-Pb \rightarrow \Upsilon\text{'} \rightarrow \mu^+\mu^-) =$ 120μb, and $B_r d\sigma/dy(Pb-Pb \rightarrow \Upsilon\text{"} \rightarrow \mu^+\mu^-)$= 41 μb have been used, where B_r indicates the branching ratios for Υ, Υ' and Υ" decays into muon pairs. These cross-sections are valid for minimum-bias Pb-Pb collisions.

In these preliminary studies, the signal-to-background ratio S/B has been estimated starting from the average number of reconstructed $\mu^+\mu^-$ pairs per central HIJING event, i.e. 0.011 with the standard set of cuts (see Section 8.3). Since the di-muon background is expected to be proportional to N^2, the square of the charged particle multiplicity above the applied p_T cut, a correction factor $(N_{b=0}/N_{min-bias})^2$ was used to derive the $\mu^+\mu^-$ background for minimum-bias events from that determined in Section 8.3 for central Pb-Pb collisions. With $N_{b=0}/N_{min-bias}$=4.5, the expected number of $\mu^+\mu^-$ pairs per event is $\sim 5.3 \times 10^{-4}$. Taking into account the signal and background acceptances in the Υ mass region, and assuming a total Pb-Pb cross-section of 8 b and a $\Upsilon \rightarrow \mu^+\mu^-$ production cross-section of 410 μb, signal-to-background ratios of S/B=0.5 and S/B=1.3 were obtained over the full detector acceptance and for the region $|\eta| < 1$ respectively.

These estimates have to be taken with caution, and need to be confirmed by more complete studies based on high-statistics samples of minimum-bias Pb-Pb events. The background level depends crucially on the maximum charged particle multiplicity given by the generator, especially in the forward regions. It is also very sensitive to the π and K transverse momentum distributions used in the model. As an example, with the SHAKER generator, which predicts a harder p_T spectrum for pions and kaons than HIJING, the estimated S/B ratio would decrease by about a factor of about two [45].

On the other hand, these studies have been made with algorithms not specially tuned to the heavy-ion environment, and with simple analysis cuts and techniques. There is therefore margin for improvement.

Possible schemes to trigger on $\Upsilon \to \mu^+\mu^-$ events in heavy-ion collisions are presently being investigated. One way would be to use a di-muon trigger(see Chapter 9). Table 8.1 shows the total signal acceptance and the S/B ratio as a function of the muon p_T cut. It is crucial to trigger on muons with p_T as low as 3.5-4 GeV (see Fig. 8.3), a possibility which is under study. Another option is to combine an interaction trigger based on the forward calorimeter (see Chapter 9) with a loose single or di-muon trigger in the Muon Spectrometer.

p_T (min) (GeV)	3.0	3.5	4.0	4.5
Acceptance+efficiency $\lvert\eta\rvert < 2.5$	14.3%	14.1%	12.5%	5.5%
S/B $\lvert\eta\rvert < 2.5$	0.5	0.6	0.6	0.5
Acceptance+efficiency $\lvert\eta\rvert < 1$	4.9%	4.9%	4.6%	2.7%

Table 8.1: Acceptance for $\Upsilon \to \mu^+\mu^-$ signal events and S/B ratio as a function of the p_T threshold on both muons.

The number of $\Upsilon \to \mu^+\mu^-$ events which can be accumulated in one month of Pb-Pb operation has been estimated by assuming 10^6 s of effective data taking time, which corresponds to a machine and experiment efficiency of 40%. Assuming an average luminosity of 0.4$\times 10^{27}$ cm^{-2} s^{-1}, and a signal acceptance limited to 6% by a muon pseudo-rapidity cut $|\eta| < 1.2$ (in order to get a clean separation between Υ and Υ'), the number of recorded events is expected to be 10^4 per month of Pb-Pb running. This number does not take into account the trigger efficiency, which has not been estimated yet. Nevertheless, even assuming an additional signal reduction by a factor of two, to account for inefficiencies from the trigger and/or additional analysis cuts, the remaining statistics will hopefully be sufficient to study the Υ production as a function of the collision centrality.

Suppression of quarkonia resonances has to be established with respect to a signal which is not affected by the evolution of the interacting coloured medium created in the Pb-Pb collision. At the LHC the Drell-Yan process, which was used as a reference at the SPS [42], is expected to have a very low rate. The possibility of using $Z \to \mu^+\mu^-$ decays, and maybe also $Z \to e^+e^-$, is being investigated.

8.5 Charmonium states

A basic difference in the experimental study of Υv and J/ψ production is that, because of its mass, the Υ can be measured over its full p_T spectrum starting at p_T=0. Indeed, even if the Υ is produced at rest, the decay muons have in general enough energy to traverse the calorimeters and reach the Muon Spectrometer. The situation is different for muons from J/ψ decays, which in most cases need an additional p_T from the parent particle, or a Lorentz boost, to reach the Muon Spectrometer. As a consequence, a full p_T analysis of the $J/\psi \to \mu^+\mu^-$ channel (which is important because quarkonia suppression may depend on the resonance transverse momentum) is only possible in the forward regions where, however, the background is largest.

On the other hand, $J/\psi \to \mu^+\mu^-$ production has a much larger cross-section than Υ production, which allows stricter cuts to be applied to reduce the background. The cross-section for the process

$J/\psi \rightarrow \mu^+\mu^-$ at the LHC can be derived, in a similar way as for the Υ, from Equation 8.1 with $\alpha = 0.90$, which gives $B_r d\sigma/dy(Pb + Pb \rightarrow J/\psi \rightarrow \mu^+\mu^-) = 58$ mb [45]. Another advantage is that the reconstructed di-muon mass resolution (∼53 MeV from a full-simulation study) is sufficient to separate J/ψ from ψ' even in the forward regions of the detector, which is probably not the case for the Υ resonances.

Finally, it should be noted that tagging displaced vertices (see Section 5.2) provides a tool to discriminate prompt J/ψ, which are expected to undergo suppression, from J/ψ from B-meson decays. The ratio between prompt and decay J/ψ could be studied as a function of the event centrality.

An evaluation of the ATLAS potential for the observation and detailed analysis of charmonium states is under way.

Chapter 9

Trigger and DAQ Issues

Aspects related to triggering and recording heavy-ion events are the subject of this Chapter. Although studies in this area are at a very preliminary stage, a few ideas about possible trigger menus for heavy-ion data taking, satisfying the ATLAS Trigger/DAQ and offline technical and financial boundaries, are discussed.

As in previous Chapters, the emphasis will be on Pb-Pb collisions, since in most cases they are more challenging than lighter ion-ion collisions and pA collisions.

9.1 Overview of the ATLAS Trigger and DAQ system

The ATLAS Trigger and DAQ (T/DAQ) system is designed to cope with the challenging conditions in pp collisions at the LHC design luminosity of 10^{34} cm^{-2} s^{-1}. It has to reduce the interaction rate of about 1 GHz, occurring with a bunch-crossing frequency of 40 MHz, to an output rate to mass storage of $\mathcal{O}(200$ Hz$)$. The emphasis has been put on the selection of high-p_T events containing leptons, photons, jets and missing or total transverse energy.

ATLAS will use a three-level trigger system, as shown in Fig. 9.1, where the first stage (LVL1 [46]) is implemented in hardware and has to reduce the bunch-crossing frequency to at most 100 kHz within a maximum latency of 2.5 μs. During this time, the event data are stored in pipeline memories in the front-end electronics of the sub-detectors. After a LVL1 accept, the event fragments are transferred from these pipelines to about 1600 readout buffer (ROBs), via readout drivers (RODs) and readout links.

The Higher-Level Triggers (HLT [47]) provide further rate reduction by up to three orders of magnitude before the events are transferred to mass storage. The HLT is composed of two separate selection stages, the second level trigger (LVL2) and the event filter (EF). In both cases, the selection is done with commercially available CPUs using software algorithms.

9.1.1 LVL1 signatures

The information available for LVL1 is restricted to data (in coarse granularity) from the calorimeter systems and from the dedicated muon trigger chambers (RPCs in the barrel and TGCs in the end-caps). For the calorimeter part of the trigger, the following object types are foreseen:

EM: electron or photon candidate in $|\eta| < 2.5$.

TAU: tau/single hadron candidate in $|\eta| < 2.5$.

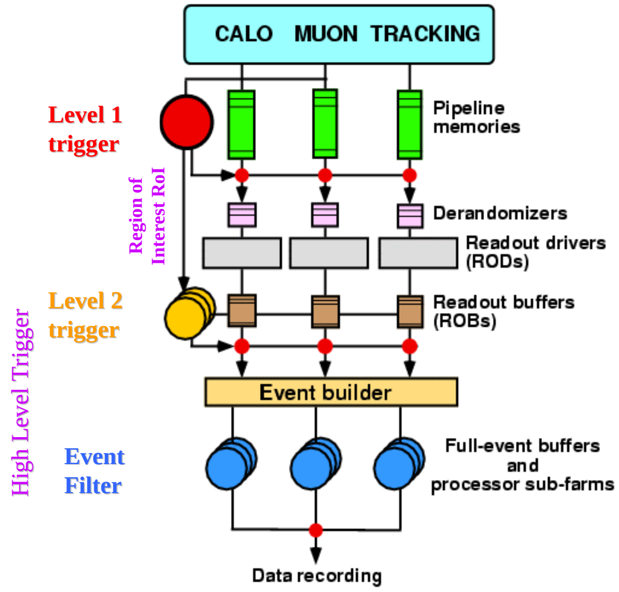

Figure 9.1: Schematic view of the ATLAS T/DAQ system.

J: jet candidates in $|\eta| < 3.2$, with the possibility of using different window sizes, as well as forward energy depositions up to $|\eta| \sim 4.9$.

xE: missing transverse momentum (computed over $|\eta| < 4.9$).

E: total transverse energy (computed over $|\eta| < 4.9$).

All of the algorithms defining the above objects are implemented in programmable logic arrays (FPGA), and thus some flexibility in their adaptation is available, beyond the simple adjustment of threshold values. For example, different algorithms can be implemented for a FCAL-based interaction trigger for heavy-ion operation, as discussed in Section 9.3.

From the information of the muon trigger chambers, one additional object type is provided at LVL1:

MU: muon candidate in $|\eta| < 2.4$.

The definition of the **MU** objects is based on coincidences between several stations, where again flexibility exists in the details of the coincidence requirements.

More details on LVL1 can be found in [46]. It should be noted that the capability of LVL1 to select high-p_T signatures will be useful not only for pp, but also for pA and AA operation. Indeed in the latter cases, in addition to peripheral low-p_T collisions, for which a dedicated LVL1 trigger is necessary (see Section 9.3), one will also need to record enriched samples of events where a hard interaction has occurred.

9.1.2 HLT signatures

LVL2 reduces the LVL1 accepted rate to a few kHz, by using only a few percent of the data of a full event, relying on the guidance of Regions-of-Interest flagged by LVL1. For these regions, LVL2 has access to the full granularity of all sub-detectors, and thus can combine the information of different detectors. LVL2 has to operate within a tight time budget and to provide the decision after a latency of about 10 ms only, which is achieved by using specialized and optimised algorithms.

After a LVL2 accept, all fragments of the event are collected (event building) and the full event is then passed to a processor in one of several EF farms for the final rate reduction. The EF processors will use offline-derived software to refine the selections of LVL2, within a more relaxed time budget of about one second.

At the HLT, the high-p_T objects found by LVL1 are refined and the following objects can be used for selection criteria: electrons (e) and photons (γ), derived from a LVL1 **EM** object, muons (μ, from LVL1 **MU**), tau hadrons (τ, from **TAU**), jets (j) and b-tagged jets (b), derived from LVL1 **J** objects, E_T^{miss} (from **xE**) and ΣE_T (from **E**). At the EF level it will also be possible to implement selection criteria which do not rely on an explicit high-p_T requirement at LVL1.

During pp operation, the total rate to mass storage after the HLT selection will be limited, mainly by offline computing resources, to ≈ 200 Hz of 1.5 MB size events. This rate×size to storage of ≈ 300 Hz×MB is assumed in the following as an upper limit also for heavy-ion collisions.

9.2 Boundary conditions in heavy-ion collisions

During Pb-Pb operation, the luminosity will be significantly lower than in pp runs, i.e. about 10^{27} cm^{-2} s^{-1}. The total interaction rate is expected to be about 8 kHz, of which only ~3 % will come from central collisions with an impact parameter $b < 3$ fm. The spacing between two bunch-crossings will be 100 ns.

9.2.1 Event size

Unlike the interaction rate, the particle multiplicity in the final state will be much larger in Pb-Pb collisions than in pp interactions, leading to a sizable increase in the detector occupancies (see Chapter 3) and in the event size.

Based on simulation studies presented in the previous Sections, a (conservative) estimate for the event size of about 5 MB has been obtained for central ($b < 1$ fm) Pb-Pb collisions. This size is dominated by the information from the Inner Detector (Pixels and SCT) with about 3.2 MB, followed by the calorimeters (about 1.4 MB) and the Muon Spectrometer (about 0.2 MB).

These numbers should be considered as upper limits because, on the basis of the achieved understanding of the detector performance and of the physics goals, several ways could be envisaged to reduce the event size. Partial event building, i.e. recording only the information of some sub-detectors (e.g. Pixels and SCT), could be implemented for some event samples. Another possibility is loss-less data compression, which however requires adequate resources to run suitable data packing algorithms at the EF level. Zero-suppression or other compression schemes can be foreseen in the calorimeters.

Obviously, the event size for more peripheral Pb-Pb collisions, for lighter ion-ion collisions and for pA collisions will be smaller.

9.2.2 Event selection requirements

Although the requirements on the selectivity and background rejection capabilities of the trigger system are less stringent in heavy-ion collisions because of the lower interaction rate, it will be of

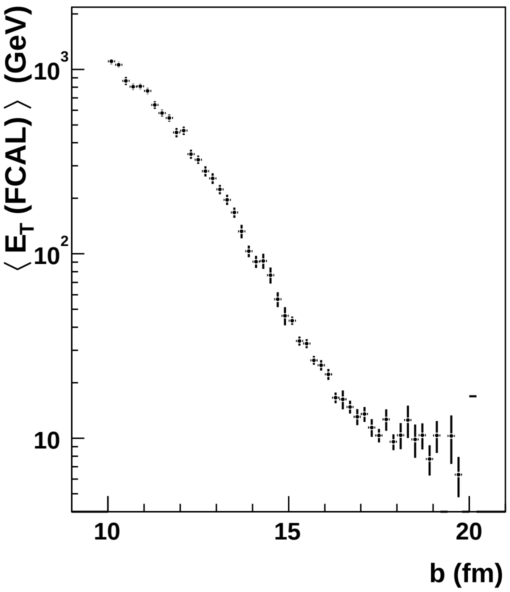

Figure 9.2: Average transverse energy deposited in the forward calorimeter as a function of the collision impact parameter (from full simulation).

utmost importance to be able to select, in as an unbiased way as possible, events where an inelastic AA interaction has occurred. Obviously, only a fraction of these events will be recorded eventually, e.g. by prescaling. Furthermore, it will also be important to trigger on collisions with various levels of centrality, and to be able to collect enriched samples containing high-p_T objects.

In order to cope with a maximum data rate to storage of ≈ 300 Hz×MB, as in pp collisions, and given a (conservative) size of 5 MB for Pb-Pb events, the target output rate after the HLT selection should be about 50 Hz for (central) events.

9.3 Interaction trigger

In order to select generic inelastic AA collisions, a LVL1 interaction trigger is needed. Such a trigger should be efficient for all impact parameters and possibly select also ultra-peripheral collisions. With the present layout of the ATLAS detector, and on the basis of very preliminary studies, the most promising solution seems to be a trigger based on the transverse energy deposited in the forward calorimeter, which covers the pseudo-rapidity range $3.1 < |\eta| < 4.9$.

As discussed in Chapter 4, the total particle multiplicity produced in the collision is correlated with the impact parameter. Simulation studies have shown that also the transverse energy deposited in the FCAL varies monotonically with the impact parameter (see below). Therefore the FCAL signal may be used not only as the basis of a generic and simple LVL1 interaction trigger, but also to select events with different levels of centrality.

Several types of FCAL-based selections can be envisaged: single arm triggers (i.e. requiring a signal in one of the two FCALs), coincidence triggers (i.e. requiring signals in both FCALs) and triggers based on the total E_T deposited in both calorimeters. These triggers are expected to be fully efficient for relatively central collisions. However, as the impact parameter increases, the detection efficiency decreases because of the lower particle multiplicity. A full simulation study was therefore performed with a sample of Pb-Pb events with $10 < b < 30$ fm (for $b < 12$ fm there is enough energy in the FCAL to ensure an efficient trigger selection). The simulation used a detailed description of the forward regions up to $|\eta| = 5.1$, including the FCAL and the surrounding active and inactive elements. One of the results obtained from this study is the anti-correlation between the total E_T deposited in the FCAL and the collision impact parameter, shown in Fig. 9.2.

To form a LVL1 trigger decision, the transverse energy deposited in the FCAL is first collected in Trigger Towers (there are 128 such towers in each of the two FCALs), where a noise threshold is applied. Then, signals from the Trigger Towers are summed in larger slices, called Trigger Wedges. There are eight Wedges per FCAL, each one covering the full η range and 1/8 of the azimuthal angle. Two trigger schemes have been studied: a coincidence trigger, and a total E_T trigger. To form a coincidence trigger, Wedges with signals above a given E_T threshold are required in both forward calorimeters. For the total E_T trigger, the total transverse energy in both calorimeters is summed, and is compared to a given threshold. The resulting trigger efficiencies are shown in Fig. 9.3 for the two trigger types and for three different noise thresholds applied at the Trigger Tower level.

The best performance has been achieved with a total E_T trigger, where e.g. for a Trigger Tower threshold of 0.5 GeV only 5% of all inelastic events are lost. On the other hand the coincidence trigger potentially offers rejection power against background events, like beam-gas interactions.

Additional studies are needed to define the details of this interaction trigger, in particular the affordable threshold values. It may be, for instance, that bunch-crossing identification requirements can be relaxed in the FCAL, due to the relatively long bunch spacing of 100 ns for heavy-ion operation, allowing smaller Trigger Tower E_T deposits to be used in the trigger.

In conclusion, although the results shown in this Section are very preliminary, they nevertheless indicate that ATLAS has a viable LVL1 interaction trigger, based on the forward calorimeter, able to select generic inelastic AA interactions over a large range of impact parameter values.

9.4 Selection signatures

The discussion concentrates here on Pb-Pb collisions at peak luminosity. It is expected that the selection requirements for pA collisions are closer to the pp case than Pb-Pb collisions are, with a larger emphasis on high-p_T objects, for which the ATLAS T/DAQ system has been designed.

LVL1 signature	HLT signature	Physics coverage
random	random	zero-bias sample
INT(FCAL)	int(FCAL)	centrality /interaction
EM	e	$Z \to ee$
EM	γ	photon production
2EM	2e	$Z \to ee$
MU	μ	$Z \to \mu\mu$, $\Upsilon \to \mu\mu$
2MU	2μ	$Z \to \mu\mu$, $\Upsilon \to \mu\mu$
nJ	nj	jet production

Table 9.1: Examples of LVL1 and HLT selection signatures for heavy-ion operation.

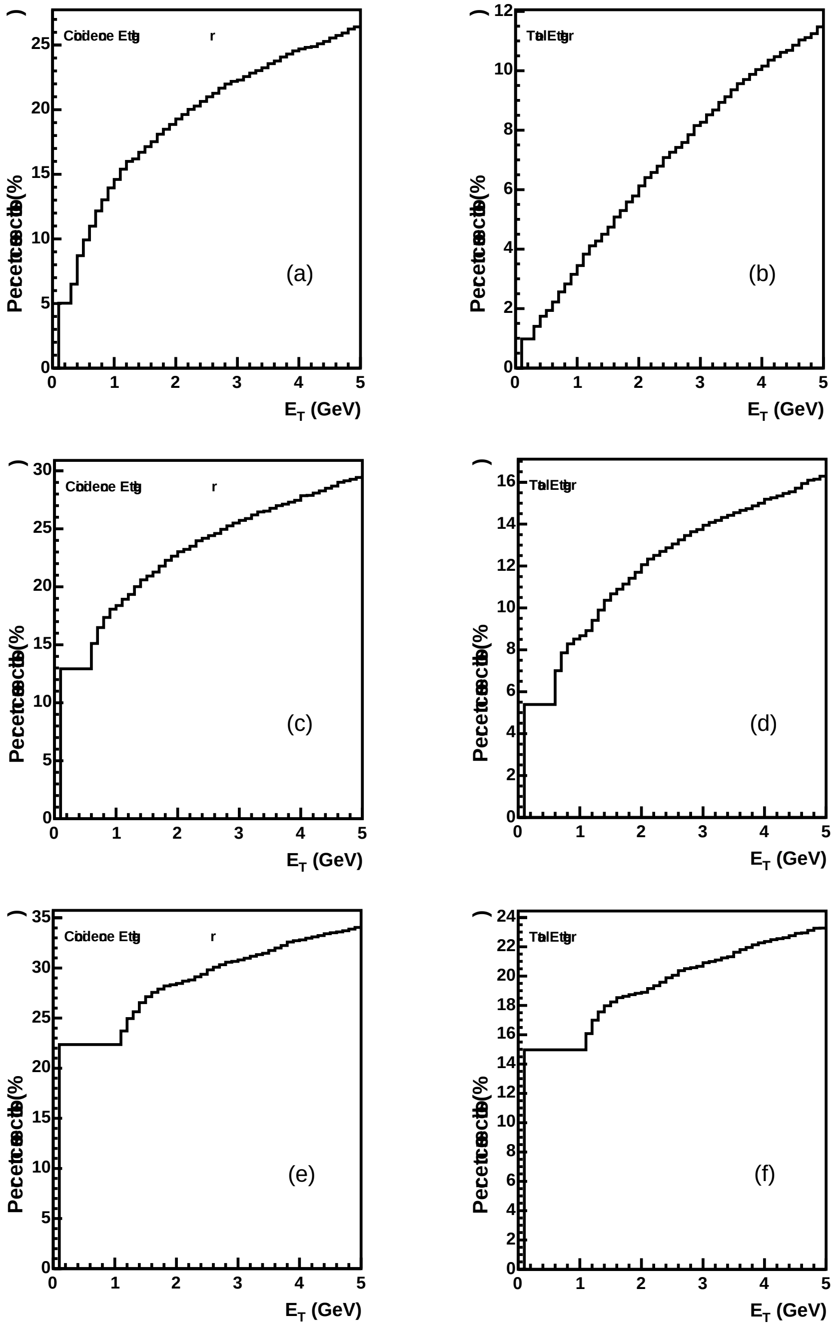

Figure 9.3: The inefficiency of two possible LVL1 interaction triggers, as a function of the E_T threshold. The left column is for a coincidence trigger, the right column for a total E_T trigger (see text). The upper, middle and bottom plots were obtained with Trigger Tower thresholds of 0.25 GeV, 0.5 GeV and 1 GeV, respectively.

As mentioned in Section 9.2.2, the maximum output rate after the HLT selections is limited to about 50 Hz (conservative bound) for Pb-Pb collisions. Since the event size is expected to be smaller for non-central collisions, a larger accept rate should be possible for these processes.

Several types of selection signatures can be foreseen. Examples are listed schematically in Table 9.1. An interaction trigger based on the transverse energy deposited in the forward calorimeter, supplemented by a random trigger for a zero-bias selection, should provide generic samples of heavy-ion collisions with different levels of centrality. In addition, menus based on high-p_T objects can be used to enhance the statistics of events with e.g. jets or a $\Upsilon \to \mu^+\mu^-$ decay. A cut on the event centrality could be combined with these high-p_T signatures, thereby allowing lower object thresholds.

The sharing of the trigger bandwidth between the various menus will be determined on the basis of the detector performance and of the physics understanding, and will most likely be changed quite often during data taking. It is also foreseen, especially at the beginning, to take dedicated runs to collect, for instance, large samples of minimum-bias events, which are useful to study the trigger efficiency for high p_T objects.

Preliminary estimates of the expected trigger rates for some representative signatures are given below. In order to keep the total rate below ~50 Hz, several trigger items will need to be prescaled. The goal is to avoid as much as possible prescaling of the high-p_T selections, in order to collect enough statistics of rare events.

An interaction trigger based on the FCAL transverse energy should provide event samples with different centrality. Table 9.2 gives an indication of the expected rates as a function of the cut on the total E_T deposited in the forward calorimeter. It should be noted that the range given for the impact parameter is only indicative, since a sharp cut in E_T does not translate into a fixed cut on b. The above selection can obviously be further refined at the HLT, as e.g. in the EF the whole event information and a more accurate calibration are available. Also, for medium and small impact parameters ($b < 10$ fm), a trigger based on the total transverse energy deposited in the electromagnetic calorimeter could complement (and be more effective than) the FCAL trigger in selecting event samples with different centralities (see Fig. 4.8). Furthermore, the selection efficiency for events with large impact parameter could be increased by using the scintillator devices that ATLAS is planning to install in front of the end-cap cryostats to trigger on beam-halo, beam-gas and minimum-bias events in the first year(s) of commissioning and operation [48]. All these issues will be studied in the future.

E_T cut	rate	centrality	fraction of σ_{tot}
> 5.6 TeV	0.3 kHz	$b < 3$ fm	3%
> 4.3 TeV	0.8 kHz	$b < 5$ fm	10%
> 1.7 TeV	2.4 kHz	$b < 9$ fm	30%
> 0.3 TeV	5.6 kHz	$b < 13$ fm	70%
> 1 GeV	6.8 kHz	unbiased	85%
> 0.25 GeV	7.9 kHz	unbiased	99%
$1 < E_T < 30$ GeV	0.9 kHz	$b > 15$ fm	11%

Table 9.2: Expected event rates, event centrality and selected fraction of the total Pb-Pb cross-section for an interaction trigger based on the total transverse energy in the FCAL, as a function of threshold (a Trigger Tower threshold of $E_T = 1$ GeV has been used, except for the second last row).

The selection of di-muon events, e.g. to study quarkonia resonances as discussed in Chapter 8, will be based on a LVL1 di-muon trigger (possibly supplemented by a cut on the event centrality), refined by the HLT algorithms. A first estimate of output rate has been obtained with optimistic assumptions on the detector performance. With a muon p_T threshold of 3 GeV, the total di-muon rate is expected to be about 9 Hz. Requiring in addition opposite muon charges decreases this rate to about 4.5 Hz. A further reduction could be achieved, if needed, by applying a mass cut on the di-muon system. For example, asking the di-muon invariant mass to be in the range 9-10 GeV suppresses the rate by almost a factor of 25.

The expected jet rate is a strong function of the jet transverse energy threshold. For $E_T > 50$ GeV, $E_T > 100$ GeV and $E_T > 200$ GeV, event rates of about 40 Hz, 0.1 Hz and 0.02 Hz have been estimated for jets with pseudo-rapidities limited to $|\eta| < 2.5$. These results are optimistic since they assume that the background from soft particles produced in the same interaction has been subtracted using e.g. the procedure described in Chapter 6. This operation, however, will most likely be done only at the level of offline analysis (or maybe in the Event Filter).

9.5 Issues for future studies

The ATLAS T/DAQ system offers, in its baseline design, a large degree of flexibility, and therefore should be relatively easy to adapt to the different running conditions expected in heavy-ion collisions.

The full-simulation studies of the detector environment and performance reported in the previous Chapters provide useful information for detailed future investigations of various aspects of the T/DAQ system. As an example, more complete cross-checks will be made that the front-end electronics of all sub-detectors have sufficiently long buffers, so that, in spite of the higher detector occupancy, no dramatic truncation of event fragments occurs before these fragments are stored in the ROBs for the asynchronous HLT processing.

Chapter 10

Summary

In this Letter of Intent, first and preliminary results have been presented of the expected potential of the baseline ATLAS experiment for the study of heavy-ion collisions. Emphasis has been given to high-p_T probes, which best match the design concepts of the detector.

The main conclusions of these studies, which are based on detailed GEANT-simulations of the detector layout and response in the worst-case scenario of Pb-Pb central collisions, can be summarized as follows:

- In general, the detector performance is not expected to be significantly deteriorated by the more difficult environment to which it will be exposed in Pb-Pb collisions (with the exception of the TRT). This demonstrates also the robustness and flexibility of the experiment in coping with conditions for which it has not been specifically designed.
- ATLAS has many handles to extract the global event characteristics, e.g. through the measurements of charged particle multiplicity and calorimetric transverse energy flow. It has been shown that these global observables can be measured with high accuracy on an event-by-event basis, and can also be used to determine the collision impact parameter and thus the event centrality.
- It has been demonstrated that, even without the contribution of the TRT, efficient tracking can be performed in the (dense) heavy-ion environment by using the precision layers of the Inner Detector. This performance is crucial for a large number of physics studies, like jet quenching and quarkonia suppression.
- The issue of whether jet quenching mechanisms are best measured via modified fragmentation functions, jet cross-sections for a fixed cone size, jet transverse profiles, back-to-back correlations, or otherwise, is under current theoretical discussion. Measuring as broad a range of these observables as possible will optimize the tools for understanding the underlying physics. The ATLAS calorimetry, with its hermetic coverage, fine segmentation, and excellent jet resolution, is very well suited for these studies. It has been shown that efficient reconstruction of jets with $E_T >$ 40 GeV is possible in Pb-Pb events, for an acceptable rate of fakes, in spite of the additional background noise coming from the soft part of the collision. The jet energy resolution has been found to be similar to that achieved in pp interactions at design luminosity for $E_T > 100$ GeV, and about 40% worse at $E_T \sim$ 40 GeV. Furthermore, the ability to analyze the jet fragmentation function over a broad z range by using charged hadrons has been studied, and first results are promising.

- QCD is flavour-invariant and thus all quarks should interact in the medium in a similar manner. However, heavy-flavour partons may have suppressed first-order gluon radiation, and thus measurements of b-jets provide an additional tool to understand quenching physics. The studies presented in this document show that ATLAS offers significant b-tagging capabilities even in the heavy-ion environment.

- Heavy quark-antiquark bound states allow for a probe of the screening of the long-range confining potential of QCD in the plasma. The wide range of binding energies of the Υ (1s,2s,3s) states makes the measurement of their relative yields an effective thermometer of the plasma. It has been shown that the $\Upsilon \rightarrow \mu^+\mu^-$ mass resolution achieved by combining tracks reconstructed in the Muon Spectrometer, which maintains relatively low occupancy even in central Pb-Pb events, with tracks in the precision layers of the Inner Detector is comparable to that obtained in pp interactions. The capability of separating Υ and Υ' states, at least in the central part of the detector, has been demonstrated. Initial studies of the expected signal-to-background ratios for the Υ states are quite encouraging.

Proton-nucleus reactions provide excellent calibration data for heavy-ion reactions, but also hold the key for many aspects of low-x physics, which are interesting in their own right. The forward coverage of ATLAS gives access to very low-x parton distributions in the nuclear wave-function. By reconstructing jets with $E_T \sim 15\ GeV$ in the forward directions, it should be possible to probe physics in the $x \sim 10^{-5} - 10^{-4}$ range. In proton-nucleus collisions the detector occupancy will be similar to or lower than that expected in high-luminosity pp runs. The full performance of the ATLAS detector will therefore be available for such studies.

This initial round of simulations has been performed with standard ATLAS software tools, with minimal modifications in most cases, yielding nevertheless very encouraging results. The next step will be to develop algorithms tailored to heavy-ion events. This should allow improvements to be achieved on issues such as tracking in a very high-multiplicity environment, efficiency for J/ψ and Υ reconstruction, and performance for reconstructing jets with moderate E_T (in the range 20-60 GeV).

Outstanding problems which need further study have also been identified, and will be addressed in the future.

Predictions for which physics scenarios will be realized in heavy-ion collisions at the LHC energies are difficult to formulate today. There are also large uncertainties on the global picture which will eventually emerge from RHIC data. As new physics items are provided from the experimental and/or theoretical side, further simulations will be required. Nevertheless, the ATLAS performance for the study of heavy-ion collisions presented in this Letter of Intent offers, today, a significant addition to the exciting physics programme of the experiment.

Appendix A

Forward Instrumentation

The physics goals of ultra-peripheral collisions outlined in Section 1.4 could be better achieved with the addition of a Zero Degree Calorimeter (ZDC). This detector would be located at zero degrees and incorporated into the TAN [49]. Such a device would also improve the performance of a minimum-bias trigger for Pb-Pb collisions.

There is overlap in the instrumentation described here and what is proposed in [50]. However, here the focus is on aspects specific to heavy-ion physics. The ZDC design for ATLAS could follow the ZDC calorimeters now used by all four RHIC experiments.

The LHC environment is harsher than at RHIC because of the elevated radiation doses and it needs to be properly addressed for the construction of this device. In addition, it is important to understand at the simulation level how the detector will perform. One of the main problems is the absence of reliable event generators. A modified version of HIJING has been used successfully at RHIC and will be used also here.

A.1 Forward calorimetry at RHIC

The four RHIC experiments have made extensive use of ZDC [51]. They are based on an identical design. They have a transverse dimension of 10.5 cm, and are located at a distance of 18 m from the interaction point. The total depth of the RHIC ZDC is 6 interaction lengths. They are subdivided into three identical modules consisting of tungsten absorbers and PMMA clear fiber layers. The energy resolution for 100 GeV neutrons is $< 21\%$.

The small aperture is sufficient to capture all fragmentation neutrons produced in peripheral collisions, which have small transverse momentum ($p_T \sim$ 90 MeV). It has also been shown at RHIC [23] that a forward-backward coincidence of ZDCs (placed in each beam direction) has higher efficiency than the minimum-bias beam-beam counters to define an interaction trigger. In ATLAS this would help to improve the efficiency of the interaction trigger described in Chapter 9 for events with large impact parameter. In addition, the timing resolution of this device ($\sim$ 120 ps) allows the vertex determination to a precision of 2 cm by time difference measurement between opposite calorimeters.

In the PHENIX experiment a Shower Maximum Detector (SMD), consisting of position sensitive arrays of scintillator strips, has been installed after the first 2 interaction lengths in the ZDC, in order to measure the shower profile in two orthogonal coordinates. A similar scheme could be implemented in ATLAS.

A.2 Role of a ZDC in ATLAS

The primary uses of a ZDC in ATLAS would be to:

- Determine the absolute luminosity in Pb-Pb runs from the calculable cross-section for ZDC coincidences [52].
- Provide an independent event characterization from spectator neutron multiplicity, complementing the measurements based on central particle production, at large values of the impact parameter.
- Extend the reach of interaction triggers to the most peripheral collisions, where a ZDC would help to reduce the error in the centrality determination due to trigger uncertainties.
- Tag UPC produced with a rapidity gap in either or both of the beam directions.
- Measure centre of gravity and shape of the showers (using e.g. the SMD), which are useful for determining transverse momentum distributions of neutrons as well as directed flow.

Peripheral data are a critical baseline for characterizing nuclear effects and in some cases are preferable to pp data as a reference sample for heavy-ion studies, because they are taken at the same $\sqrt{s} = 5.5$ TeV and in the same run as the heavy-ion events. Therefore they offer potentially smaller systematic uncertainties. The smaller the error in the trigger efficiency for peripheral collisions, the better this procedure works.

It is expected that also at the LHC, as was the case at RHIC, the ZDC will aid in the accelerator commissioning and monitoring during heavy-ion runs. The ZDC coincidence rates provide a real-time luminosity measurement, and thus can be used for tuning and monitoring purposes for ATLAS. The shower maximum detector in RHIC, and especially in PHENIX, has been used to measure beam location and angle in the interaction. An example showing the correlation between shower position and beam displacement during a van der Meer scan is presented in Fig. A.1. Time profiles of the ZDC hits have also been used to check the RF structure of the beams during the commissioning of the storage RF in RHIC.

A.3 Location and technology of a ZDC for ATLAS

In most respects, the rôle and performance of the ZDC/SMD in ATLAS, when the LHC stores Pb beams, will be identical to what it has been at RHIC.

On either side of the ATLAS interaction there is an absorber (TAN), designed to protect LHC magnets by limiting their absorbed dose. This absorber was built with a slot of 1 m length, 10 cm width and 0.5 m height, into which are inserted 90 cm copper absorber bars and a transversely segmented ionization chamber to be used for beam monitoring. The integration of an ATLAS ZDC design, which would replace the copper absorber bars with tungsten/fiber calorimeter components, is presently being discussed with the group responsible for the accelerator instrumentation in the TAN.

Because the beam energy is approximately 30 times higher than at RHIC, while the p_T of the fragments is independent of the energy, the acceptance is better at the LHC than at RHIC. This is true even taking into account the fact that the TAN is located 140 m away from the intersection region, as opposed to 18 m for the RHIC ZDC.

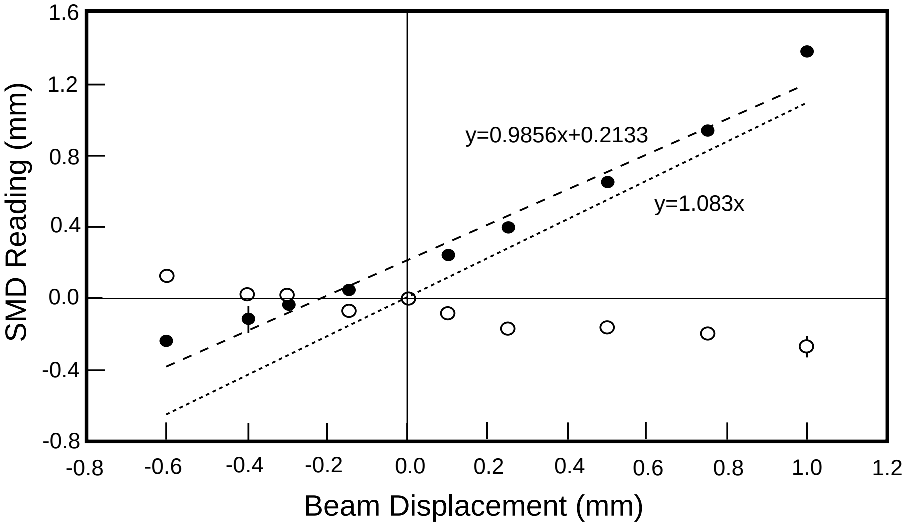

Figure A.1: Correlation between the shower position in the PHENIX Zero Degree Calorimeter and the beam displacement during a van der Meer scan (full dots). The measurement in the orthogonal coordinate (open circles) is also shown, and exhibits no dependence on beam displacement.

The ZDC detectors currently used at RHIC and two candidate technologies for this project have been implemented in a GEANT simulation. This simulation includes both, energy loss and light transport in the optical fiber readout. It also reproduces all features of a beam test of the RHIC modules, performed with a 100 GeV proton beam.

Some of the results are shown in Table A.1. For the LHC case, a readout based on 0.5 mm quartz-quartz fibers with numerical aperture NA=0.3 has been assumed.

It can be seen from Table A.1 that the energy resolution goal of 20% is achieved with lower sampling fraction than and similar overall length to the RHIC design.

The main design choice for the LHC implementation is between sampling with optical fibers parallel to the beam or with fibers transverse to it. Both give acceptable performance, but the transverse readout solution integrates more easily with the accelerator instrumentation.

Thickness (number of interaction lengths)	6	8
quartz, t=10 mm	3370, 16.0%	3440, 12.5%
quartz, t=15 mm	2220, 15.5%	2300, 13.3%
RHIC ZDC @100 GeV, t=5 mm	510, 21%	

Table A.1: Simulated light yields (in p.e.) and fractional energy resolutions for Zero Degree Calorimeters with 45% fibers and various absorber thicknesses (t). Except for the RHIC case, the incident beam is made of 2.7 TeV neutrons.

The main technological issue in the construction of calorimeters for the TAN is radiation hardness. The average dose at the TAN location is expected to reach 10 Grad/year if the LHC attains a pp luminosity of 10^{34} cm^{-2} s^{-1}. Although the radiation doses will be significantly lower during heavy-ion runs, the calorimeter should be designed to survive also during pp operation. This would ensure its usefulness as an accelerator instrument for commissioning. It would also ensure that the ZDC will be operational for the first beams with Pb ions, when it could be used to provide an early cross-check with the accelerator-derived luminosity using the cross-section computed in [52].

Since a dose of 10 Grad will reduce the transparency of quartz fibers below ~ 500 nm, the quartz-fiber calorimeter option has to be reconsidered. The two most promising solutions are to filter out short wavelengths (where radiation damage occurs), and to use a gas as the active sampling medium with Cerenkov-light readout. The choices of the readout system and of the position sensitive detector need to be coordinated with the LHC instrumentation effort.

A.4 Nuclear fragmentation modeling

A key aspect of beam fragmentation is missing from the heavy-ion event generators currently available. The number of fragment neutrons measured by the ZDC is overestimated in peripheral collisions. HIJING, for example, treats spectator neutrons as free particles, neglecting the presence of bound clusters of nucleons after the collision. On the other hand, nuclear fragmentation is known to be only weakly dependent on the centre-of-mass energy, therefore lower-energy data on fragmentation can be used to safely predict the free neutron survival probability.

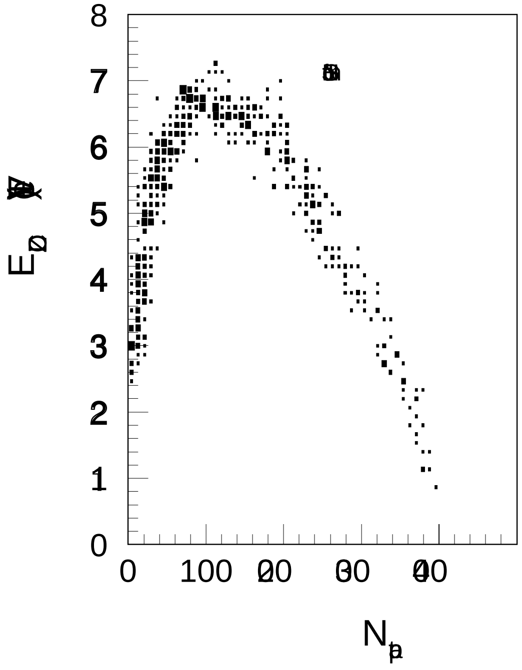

Figure A.2: Simulation results showing the correlation between the impact parameter (expressed in terms of number of interacting nucleons) and the energy deposited in the ZDC.

This procedure has been incorporated in HIJING. Starting from NA49 data on lead beam dissociation [53], an "afterburner" was introduced to the free neutron multiplicity, correcting for coalescence depending on the impact parameter. Where possible, this simulation was compared with RHIC data from PHENIX (NA49 measurements are not available for the most peripheral collisions). Finally, the “afterburner” was tuned to match the RHIC data over the full range of centralities. A correlation plot of ZDC signal versus impact parameter is shown in Fig. A.2. It should be noted that the ZDC response has the strongest impact-parameter dependence at large impact parameter values. Small impact parameters are measured better by the central calorimeters. This procedure will help greatly for future simulation studies of a ZDC in ATLAS.

Acknowledgments

We would like to thank John Byrd and Bill Turner for useful discussions about the TAN instrumentation.

Bibliography

[1] *ATLAS Collaboration, ATLAS Detector and Physics Performance*, Technical Design Report, CERN/LHCC 99-14.

[2] All ATLAS TDRs can be found at http://atlasinfo.cern.ch/ATLAS/internal/tdr.html.

[3] See for instance K. Schindl, in Proceedings of Chamonix XII, CERN-AB-2003-008, and references therein.

[4] A. Dumitru and L. D. McLerran, Nucl. Phys. **A700** (2002) 492.

[5] L. D. McLerran, *The Color Glass Condensate and Small-x Physics: Four Lectures*, hep-ph/0104285.

[6] M. Gyulassy and M. Plumer, Phys. Lett. **B243** (1990) 432.

[7] X.N. Wang and M. Gyulassy, Phys. Rev. Lett. **68** (1992) 1480.

[8] R. Baier et al., Nucl. Phys. **B484** (1997) 265.

[9] B.B. Back et al., Phys. Rev. Lett. **91** (2003) 072302;
S.S. Adler et al., Phys. Rev. Lett. **91** (2003) 072303;
I. Arsene et al., Phys. Rev. Lett. **91** (2003) 072305.

[10] J. Adams et al., Phys. Rev. Lett. **91** (2003) 072304.

[11] I. Vitev and M. Gyulassy, Phys. Rev. Lett. **89** (2002) 252301.

[12] Y.L. Dokshitzer and D.E. Kharzeev, Phys. Lett. **B519** (2001) 199.

[13] S. Digal, P. Petreczky and H. Satz, hep-ph/0110406.

[14] J.P. Blaizot and A.H. Mueller, Nucl. Phys. **B289** (1987) 847.

[15] K.J. Eskola, Prog. Theor. Phys. Suppl. **129** (1997) 1.

[16] Z. Huang, H.J. Lu, and I. Sarcevic, Nucl. Phys. **A637** (1998) 79.

[17] E. Levin and M. Lublinsky, Nucl. Phys. **A696** (2001) 833.

[18] L.D. McLerran and R. Venugopalan, Phys. Rev. **D59** (1999) 094002.

[19] F. Abe et al., Phys. Rev. Lett. **79** (1997) 584.

[20] A. Del Fabbro and D. Treleani, Phys. Rev. **D63** (2001) 057901.

[21] M. Strikman and D. Treleani, Phys. Rev. Lett. **88** (2002) 031801.

[22] C. Adler et al., Phys. Rev. Lett **89** (2002) 272302.

[23] M. Chiu et al., Phys. Rev. Lett. **89** (2002) 012302.

[24] D. Acosta et al., hep-ex/0311023.

[25] G.Baur et al., nucl-th/0307031.

[26] R. Engel et al., Z. Phys. **C74** (1997) 687.

[27] K. Piotrzkowski, in *Electromagnetic Probes of Fundamental Physics*, edited by W. Marciano and S. White, World Scientific (2003).

[28] M. Gyulassy and X. N. Wang, Comput. Phys. Commun. **83** (1994) 307.

[29] R.J. Glauber, in *Lectures in Theoretical Physics*, edited by W.E. Brittin and L.G. Dunham, Interscience, New York, (1959), Vol.1, 315.

[30] B.B. Back et al., Phys. Rev. Lett. **88** (2002) 022302, and references therein.

[31] D. Kharzeev, E. Levin, and M. Nardi, hep-ph/0111315.

[32] B. Wosiek et al., Nucl. Phys. **715** (2003) 510.

[33] C. Adler et al., Phys. Rev. Lett. **90** (2003) 032301.

[34] U. Wiedemann, Nucl. Phys. **A690** (2001) 731.

[35] C. Salgado and U. Wiedemann, hep-ph/0310079.

[36] C. Salgado and U. Wiedemann, Nucl. Phys. **A715** (2003) 783.

[37] See for instance K. Filimonov, *Jets at RHIC*, to appear in the Proceedings of the 7th International Conference on Ultra-relativistic Nucleus-Cucleus Collisions, Quark Matter 2004, Oakland, January 2004, http://www-rnc.lbl.gov/qm2004/talks/plenary/06Saturday/KFilimonov.pdf

[38] M. Gyulassy et al., Phys. Lett. **B526** (2002) 301.

[39] M. Gyulassy, P. Levai, and I. Vitev, Phys.Lett. **B538** (2002) 282.

[40] R. Baier et al., Nucl. Phys. **B484** (1997) 265.

[41] T. Matsui and H. Satz, Phys. Lett. **B178** (1986) 416.

[42] M.C. Abreu et al., Phys. Lett. **B410** (1997) 327;
M.C. Abreu et al., Phys. Lett. **B410** (1997) 337;
M.C. Abreu et al., Phys. Lett. **B450** (1999) 456.

[43] F. Abe et al., Phys. Rev. Lett. **75** (1995) 4358.

[44] D.M. Alde et al., Phys. Rev. Lett. **66** (1991) 133.

[45] G. Baur et al., CMS NOTE 2000/060.

[46] ATLAS Collaboration, *First Level Trigger*, Technical Design Report, CERN/LHCC 98-14.

[47] ATLAS Collaboration, *High-Level Trigger, Data Acquisition and Controls*, Technical Design Report, CERN/LHCC 2003-022.

[48] M. Boonekamp et al., *Cosmic Ray, Beam-Halo and Beam-Gas Rate Studies for ATLAS Commissioning*, ATLAS Note ATL-GEN-2004-001.

[49] W.C. Turner, E.H. Hoyer, and N.V. Mokhov, *Absorbers for the HighLuminosity Insertions of LHC*, in Proceedings of EPAC 98, Stockholm, page 368.

[50] ATLAS Collaboration, *ATLAS Forward Detectors for Luminosity Measurement and Monitoring*, Letter of Intent, in preparation.

[51] C. Adler et al., Nucl. Instr. and Meth. **A470** (2001) 488.

[52] A. J. Baltz, C. Chasman, and S. White, Nucl. Instr. and Meth. **A417** (1998) 1.

[53] H. Appelshauser et al., Eur. Phys. J. **A2** (1998) 383.